

Accelerated Evolution of Biomimetic Crossflow Filtration: A Parameterized, Wave Minimal
Surface Vortex Generator for Particulate Water Treatment

A Thesis

Presented in Partial Fulfillment of the Requirements for the

Degree of Master of Science

with a

Major in Chemical Engineering

in the

College of Graduate Studies

University of Idaho

by

Mason S. Anderson

Major Professor: Gregory Möller, Ph.D.

Committee Members: Eric Aston Ph.D.; Vibhav Durgesh, Ph.D.; James Moberly, Ph.D.

Department Administrator: Dev Shrestha, Ph.D.

December 2022

ABSTRACT

Biomimetic crossflow particulate filtration to date has focused on rudimentary replication of biological modalities without extensive considerations for filter surface optimization. The novelty of this current work lies with the utilization of bio-inspired minimal surfaces to facilitate facile topology optimization and empower accelerated evolution. In the present work we analyzed one such classic surface termed the wave minimal surface for its ability to generate vortices for antifouling shear as well as filter particles via vortex-induced shielding. To assess these characteristics, two sets of computational fluid dynamics simulations were conducted and analyzed for planar vorticity, fluid filtrate flux, and particle behavior. Furthermore, the surface was translated into a filter design and parameterized based on three distinctions: leading-edge morphology, angle of fluid incidence, and maximum width. After replicating the simulations for each structural configuration of the filter, the design which produced the highest filtrate flux was 3D printed and tested in a water tunnel for experimental validation. The mid-plane velocity field was analyzed against that of the simulation to determine where the simulation and experiment showed the greatest divergence. The results show that a reversed wave filter design with convex leading-edge, 90° angle of incidence, and maximum width of $n=1.0$ produced the best filtrate flux for the lowest energy input. The filtrate flux was found to be most sensitive to changes in outlet pressure and less so the velocity of the fluid or the particle diameter. The subsequent validation of this design for inlet fluid velocities ranging from 0.2 to 0.4 m/s produced root-mean-square errors on the order of 0.01 to 0.02 m/s.

ACKNOWLEDGEMENTS

I would like to acknowledge the entire BlueWave project team at the University of Idaho for their substantial contributions to this work as well as my committee for taking the time to advise and guide in the creation of this work.

DEDICATION

First and foremost, I would like to thank my loving and supporting wife, Zoie, for constantly bearing with me during the circus that was this thesis. I would also like to thank my co-researchers Martin Baker and Lusine Taslakyian for their constant support and dedication to the BlueWave project as a whole.

TABLE OF CONTENTS

Abstract	ii
Acknowledgements	iii
Dedication	iv
Table of Contents	v
List of Tables	vi
List of Figures	vii
Statement of Contribution	viii
CHAPTER 1: Introduction	1
Motivations	1
Biomimicry for Particle Filtration	2
Minimal Surfaces	3
Testing Methodology	4
CHAPTER 2: Initial Multiphase Testing.....	8
Simulation Setup.....	8
Results.....	10
CHAPTER 3: Wave Minimal Surface Testing.....	13
Geometry Generation.....	13
Simulation Setup.....	14
Vorticity Analysis	15
Results.....	17
Flow Orientation Testing	20
CHAPTER 4: Parameterized Filtration Testing	27
Geometry and Boundary Parameters	27
Simulation Setup.....	29
Experimental Flow Validation	30
Results.....	31
REFERENCES	42
APPENDIX A.....	46

LIST OF TABLES

Table 3.1: Parameter Suite for Size and Orientation Testing of Reverse WMS Array	20
Table 3.2: EFA Analysis Results	23
Table 4.1: Average RMSE Value for each CFD Validation.....	40

LIST OF FIGURES

Figure 1.1: Clean Water Machine Process Diagram.....	2
Figure 1.2: Wave Minimal Surface as viewed from (A) Perspective and (B) Side-View	4
Figure 1.3: Example Biomimetic Geometry for Crossflow Filtration.....	5
Figure 1.4: Current BlueWave Project RBF Configuration Diagram	5
Figure 1.5: Vortex Generation Geometries.....	6
Figure 2.1: Left-Oriented Geometries	8
Figure 2.2: Right-Oriented Geometries	8
Figure 2.3: Plot of Slat Angle vs. Particle Filtration for Left and Right-Oriented Geometries	11
Figure 2.4: Basic CFD-Informed Iterative Geometric Optimization Algorithm	12
Figure 3.1: Preliminary Vorticity Analysis Computational Domain	14
Figure 3.2: Average x -Vorticity Along Computational Domain	18
Figure 3.3: x -Vorticity Isosurface Plots	19
Figure 3.4: Examples of Different Parameter Configurations	21
Figure 3.5: Y and Z Velocity Components of each Particle for Geometry Distribution 1	22
Figure 3.6: Scree Plot for Particle Y Position	24
Figure 3.7: Factor Loading Heatmaps	25
Figure 3.8: Configuration Matrix Post-EFA	26
Figure 4.1: WMS 3D Filter Design Parameters	28
Figure 4.2: 65 Gallon Water Tunnel for Flow Validation Experiments	30
Figure 4.3: Configured Flow Tunnel Experimental Setup with PIV and WMS	31
Figure 4.4: Filtrate Flux as Percentage of Total Mass Flowrate	32
Figure 4.5: Particle Count for C19 Simulations	33
Figure 4.6: z -Vorticity of C19 Midplane at 0.2 m/s Inlet Velocity	34
Figure 4.7: Wall Shear Stress of C19 Midplane at 0.2 m/s Inlet Velocity	35
Figure 4.8: Flow Velocity Field in xy -plane with Inlet Velocity of 0.2 m/s	36
Figure 4.9: RMSE of Flow Velocity Field in xy -plane with Inlet Velocity of 0.2 m/s	37
Figure 4.10: Flow Velocity Field in xy -plane with Inlet Velocity of 0.3 m/s	38
Figure 4.11: RMSE of Flow Velocity Field in xy -plane with Inlet Velocity of 0.3 m/s	38
Figure 4.12: Flow Velocity Field in xy -plane with Inlet Velocity of 0.4 m/s	39
Figure 4.13: RMSE of Flow Velocity Field in xy -plane with Inlet Velocity of 0.4 m/s	40

STATEMENT OF CONTRIBUTION

For the paper in Chapter 3, Mason Anderson designed the model and conducted computational studies and analysis. Martin Baker co-designed the model and provided support for the computational and experimental work. Paulo Yu and Vibhav Durgesh led the experimental fluid dynamics analysis and interpretation. Gregory Möller conceived the original idea and supervised the project.

CHAPTER 1

Introduction

Motivations

Rapidly evolving global climate change coupled with detrimental impacts to water quality, food security, and waste management have propelled the advancement of not only novel technologies but sustainable and realizable ones as well [1, 2]. Both the National Academy of Engineers (NAE) and the Department of Energy (DOE) have identified access to and security of clean water as an Engineering Grand Challenge due to its' necessity in human health, economic growth, and agricultural productivity [3, 4]. In response to these threats the recovery of useable products from waste streams and the recycling of process materials is becoming more mainstream as opposed to a simple ancillary. The BlueWave Project is an interdisciplinary research group at the University of Idaho that is working towards addressing these challenges for water and waste alike through nutrient recovery in wastewater streams. The production of fertilizers for agricultural products consumes large amounts of phosphorus (P) and nitrogen (N). Phosphorus is an essential element for plant growth, but the only method to obtain it is mining [5]. On the other hand, nitrogen for fertilizers is generated from an energy-intensive process known as the Haber-Bosch process [6]. Along with the unsustainability of these sources comes the deleterious side-effect of ecosystem nutrient loading. Nutrient loading occurs when waste streams with high concentrations of P and N runoff into surface waters [7]. The increase in these nutrients leads to excessive algal growth within the water, that algal growth can lead to harmful algae blooms (HABs) and eutrophication of the body of water [8]. Removing these nutrients from waste streams is a necessity to facilitate the reduction of eutrophication and create a sustainable food and fiber system.

Currently, a process developed in the University of Idaho BlueWave Project known as the Clean Water Machine [9] incorporates reactive filtration coupled with ozonated ferric chloride to clean nutrient and particle-laden wastewater. Figure 1.1 displays the overall process diagram for the Clean Water Machine with the proposed work occurring in/impacting the red area.

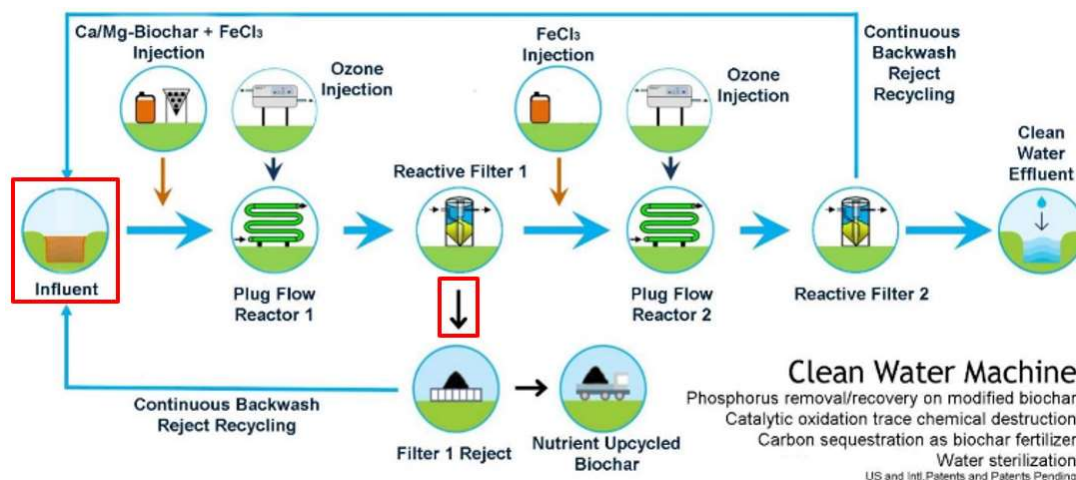


Figure 1.1. Clean Water Machine Process Diagram.

As shown above, two sources of optimization have been identified for the process. Both are in the solids-laden stream's mechanical filtration prior to or from the primary reactive filtration unit. Currently, a commercial rotary bed filter (RBF), coupled with biochar (BC) and nanobubbles, is being utilized for solids separation as an effective and lower energy alternative to energy-intensive nano- or membrane separations. This work looked to retrofit this RBF-BC system by leveraging biomimetic surface geometries to enhance the particle separation capabilities of the current process.

Biomimicry for Particulate Filtration

High-fidelity particle filtration has been a target of countless studies to date [9-15] with some having utilized a nature-inspired perspective [16-20], but few (if any) having looked at the use of minimal surfaces as bio-inspired architectures [21, 22].

Filtration through the advent of biomimetics has been studied numerous times with applications ranging from ion-mediated membranes [23, 24] to oil-water emulsions [25]. The aim of the current study is to utilize bio-inspired modalities to increase the efficiency of high-throughput crossflow filtration techniques. Particulate filtration comes in many forms, but most methods behave within two distinct categories: dead-end and crossflow [26]. Dead-end sieving is the most well-known method for filtration wherein particle-laden fluid flows perpendicular to a porous substrate with size exclusion causing particle separation. Crossflow

filtration utilizes parallel flow of the particulate stream to the substrate; this causes lift and shear to induce diffusion for particle migration. Many systems both natural and synthetic benefit from crossflow filtration over dead-end sieving due to the reduction in substrate fouling.

Nature is the penultimate example of high-throughput filtration with classic clarifiers like bivalves [27] all the way up to balaenid whales which can filter volumes in excess of 80 m³ per engulfment [28-31]. Previous work has been done which evaluated the continuous crossflow filtration mechanisms within the American paddlefish [16] and Manta rays [18, 19]. These works both utilized a combination of simulation and experimentation to evaluate the performance of their respective filter candidates.

One obvious problem incurred during the creating/testing of bio-inspired structures is the subjectivity of translation [32]. More specifically, where one group may aim to perfectly emulate the conditions of their inspiration [16], another may merely aim to replicate their inspiration to a reasonable degree [18]. This ambiguity can potentially lead to unforeseen loss of pertinent information within the system as a whole. To avoid this translation, this work aims to approach the problem of crossflow particle filtration without the use of a distinct natural analogue. By instead investigating a specific phenomenon which is pervasive among biological systems, minimal surfaces.

Minimal Surfaces

Minimal surfaces by their name alone indicate a surface which possess a minimal surface area based its local bounding geometry [33]. A more rigorous (but not all encompassing) definition would be to say that a minimal surface is that surface which has a mean zero curvature at all points [34]. Minimal surfaces are ubiquitous in nature from the structure of coral and our cerebellum [35, 36] to nucleic acid folding in viruses [37]. Minimal surfaces are described via hypergeometric functions with various schema for representation, but for the purposes of this work only classical surfaces in \mathbb{R}^3 will be considered. Advantages abound for minimal surfaces in filtration technology, some examples included: minimal material usage, fouling resistance from shear-modulated inertial migration [12], streamlined optimization for targeted flows, and user customizability.

As clear as the bio-inspired nature of these minimal surfaces is, their usage further allows for more rigor within the experimental methodology and optimization. Classic biomimetic studies aim to replicate the biological example to a tee, but this often lacks a strong formalism regarding where and when compromises are made during translation. The use of a minimal surface allows for the circumvention of that translation by providing objects which are both biomimetic as well as mathematically defined.

To begin an initial investigation into the use of these minimal surfaces, this work focuses on the creation, parameterization, and optimization of one such surface. More specifically, the surface of interest in this work is so termed the wave minimal surface (WMS). The WMS (Figure 1.2) was first noted by Patrice Jeener in 1994 [38, 39] and was one of many that they created during their career. The WMS was chosen as the crux of this work because it resembles common vortex generators such as the Wheeler and micro-ramp (MR) [40]. Beyond vortex generation, the exotic patterning of filtration substrates for use in crossflow applications has been shown to greatly increase antifouling properties while maintaining filtrate flux [41, 42].

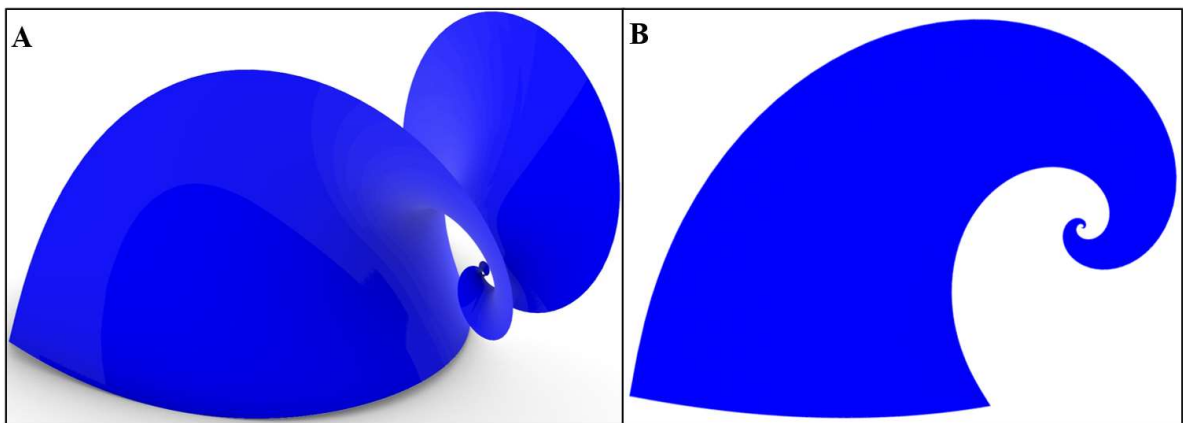


Figure 1.2. Wave Minimal Surface as viewed from (A) Perspective and (B) Side-View.

Testing Methodology

There are four main activities of the current work, three involve sets of in-silico simulations of the WMS while the remaining activity is done to experimentally evaluate those simulations of the WMS for particle filtration ability. The three sets of simulations are

conducted with computational fluid dynamics (CFD); the first set of simulations are conducted to investigate the results shown by Divi, Shrother, and Paig-Tran in [18] as it pertains to our system of interest. To do so, a simulation is conducted utilizing a slatted geometry similar to the one shown in Figure 1.3; that geometry is then tested with particles (suspended in fluid water) both with and without the addition of O₂ bubbles. The gaseous bubbles act to mimic conditions seen in the full-scale RBF system (Figure 1.4) with the purpose of the simulation being to see if the so called “ricochet” filtration mechanism (described in [18]) is being observed as well as providing a staging ground for more advanced multiphase simulations.

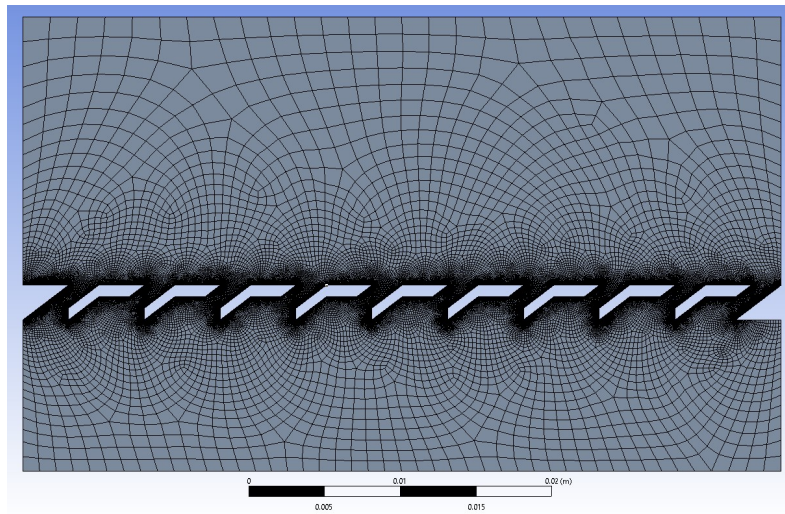


Figure 1.3. Example Biomimetic Geometry for Crossflow Filtration.

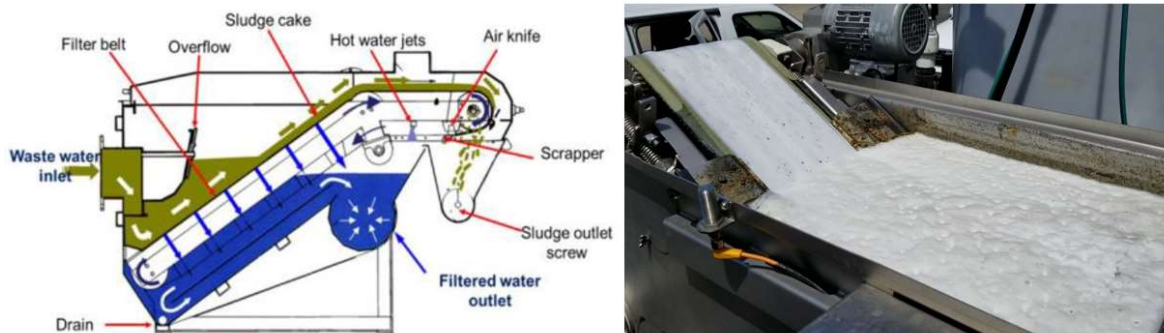


Figure 1.4. Current BlueWave Project RBF Configuration Diagram (left) and the RBF with nano-bubble process equipment in operation at an ID dairy processor in 2019 (right).

The second set of simulations are done to roughly assess the vortex generation ability of the WMS prior to a parameterized structure modification. To do this, the average vorticity (in the plane perpendicular to fluid flow) is evaluated over the surface of the WMS in two different flow configurations compared to a MR of the same characteristic length (Figure 1.5). Extensive study on vortex identification/elucidation is not conducted here as to corral the scope of this work to the realm of particle filtration; for advanced vortex treatments refer to other works [40, 43-50]. The final set of simulations are built to optimize the structure of the WMS for particle filtration (with various boundary conditions) based on three structure parameters: leading-edge morphology, maximum width, and angle of fluid incidence. Further details as to the evaluated variables, optimization criteria, and structure parameters can be found in Chapter 4. Hailing from these activities, the primary goals of the CFD simulations are to first compare the relative vorticity of the WMS against a common analogue and then optimize the WMS structure towards the highest particle filtration efficiency.

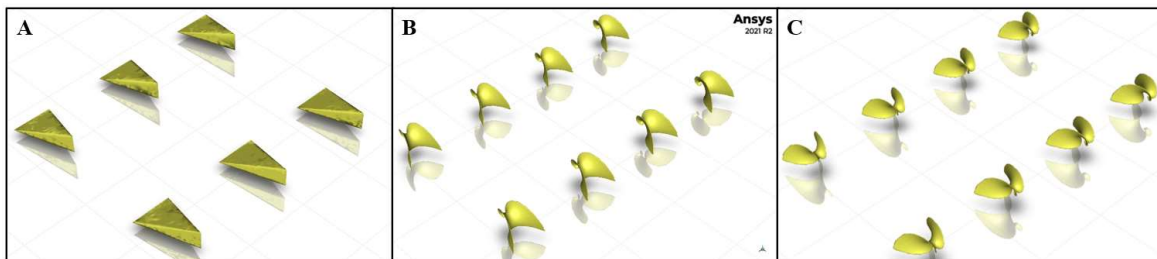


Figure 1.5. Vortex Generation Geometries for (A) Wheeler/MR, (B) WMS, and (C) Reverse-WMS

After the simulations, the final WMS filter design is 3D printed and validated experimentally. The validation experiment is done within a water tunnel where particle image velocimetry (PIV) is used to produce the velocity field surrounding the WMS filter. That velocity field is then compared to the same field from the CFD simulation (particle filtration set) where the PIV field is assumed to be the ground truth. The error between these fields is then evaluated to reveal areas where the simulation and experiment diverge to a significant degree. Contingent upon the accuracy between ground truth and the CFD, an

algorithmic approach can be developed for further testing of minimal surfaces for particulate flow simulations.

These activities and goals mirror those done in similar studies [16-19, 29, 30], where a computational simulation is built and tuned based on a number of criteria to produce a resultant simulation which provides a high-fidelity snapshot of the specific case being built. That resultant simulation is then systematically compared to experimental flow dynamics (EFD) to assess the accuracy of the simulation for that specific case. Beyond similar studies, this work aims to employ exploratory factor analysis to investigate the impact of array orientation and spacing in the surface substrate conducted during Chapter 3 to better guide future array-based testing methodologies.

CHAPTER 2

Initial Multiphase Testing

Simulation Setup

The use of these initial CFD simulations is to probe the capabilities of the simulation software for use in multiphase CFD. The software utilized for all simulation sets was ANSYS 2021 R2 using the Fluent case solver [51]. The simulations will begin with 2D representations of the biomimetic geometries seen in Figure 2.1 and 2.2; these slatted geometries are constructed for three different slat angles (30° , 45° , and 60°). Furthermore, the slats are separated into left-oriented (Figure 2.1) and right-oriented (Figure 2.2) to gauge the impact of the slat orientation as well as the impact that a gaseous phase will have on the system. These biomimetic filtration geometries are meant to separate a high-flow particle-laden stream; therefore, the simulations will be built to represent the system as closely as possible. Several multiphase solvers exist within ANSYS and differ depending upon the intended case. The final simulations are done utilizing a two and three-phase system within the geometries with two fluid phases and one solid phase; where one fluid phase is represented by gaseous bubbles during half of the simulation set.

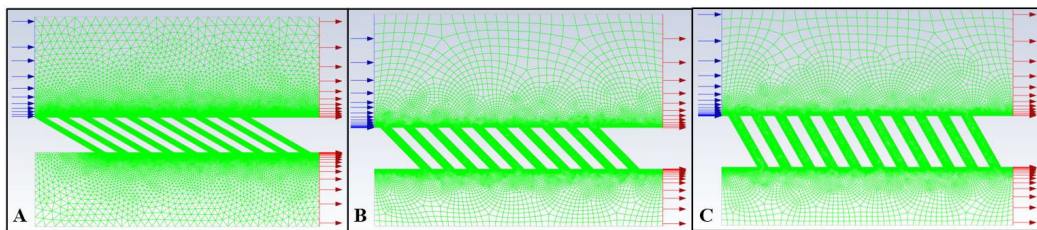


Figure 2.1. Left-Oriented Geometries for (A) 30° , (B) 45° , and (C) 60°

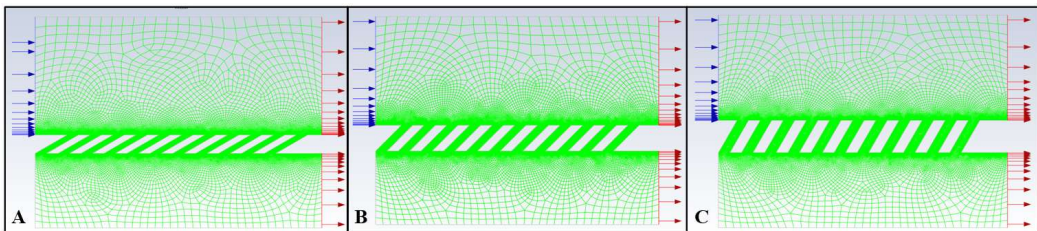


Figure 2.2. Right-Oriented Geometries for (A) 30° , (B) 45° , and (C) 60°

The two fluid phases are water and O₂, with water being the primary continuous phase and O₂ being injected at the inlet such that the volume fraction is 0.01 with a constant bubble diameter of 3e-6 m. The solid particulate phase is modeled as pure carbon particles injected from the inlet at 2.52e-4 kg/s. The maximum particle diameter is set to 1e-3 m, and the minimum particle diameter is 1e-5 m with the distribution following a Rosin-Rammler logarithmic function (spread parameter of 0.35). Along with these parameters, the inlet fluid and particle velocity is constant at 5e-2 m/s along with the slot width for all geometries which is set at 5e-4 m.

The multiphase model utilized for these simulations was the Eulerian inhomogeneous model coupled with the dense discrete phase modeling (DDPM) which simulates a secondary discrete phase in a Lagrangian frame of reference. DDPM accounts for the assumption of the typical Euler-Lagrangian multiphase model that the solid volume fraction is negligible (the mass can be greater, but the volume fraction must be low) [52]. Due to the highly particle-laden nature of the intended simulations, DPPM is required for accurate results. To account for the volume fraction of the dispersed particles, DPPM extends the mass and momentum conservation equations into a set of equations. For some discrete phase p within n total phases, the mass and momentum conservation equations are shown as (1) and (2), respectively.

$$\frac{\partial}{\partial t}(\alpha_p \rho_p) + \nabla \cdot (\alpha_p \rho_p \vec{v}_p) = \sum_{q=1}^n (\dot{m}_{qp} - \dot{m}_{pq}) \quad (1)$$

$$\begin{aligned} \frac{\partial}{\partial t}(\alpha_p \rho_p \vec{v}_p) + \nabla \cdot (\alpha_p \rho_p \vec{v}_p^2) = & -\alpha_p \nabla p + \nabla \cdot [\alpha_p \mu_p (\nabla \vec{v}_p + \nabla \vec{v}_p^T)] + \alpha_p \rho_p \vec{g} + \\ F_{vm,lift,UDF} + \sum_{q=1}^n (& \vec{K}_{qp} (\vec{v}_q - \vec{v}_p) + \dot{m}_{qp} \vec{v}_{qp} - \dot{m}_{pq} \vec{v}_{pq}) + \vec{K}_{DPM} (\vec{v}_{DPM} - \vec{v}_p) + \\ & S_{DPM,explicit} \end{aligned} \quad (2)$$

Where α , ρ , ∇p , \vec{v}_p , \dot{m} , and \vec{g} are volume fraction, density, pressure gradient, velocity vector, mass flow rate, and gravity vector, respectively. $F_{vm,lift,UDF}$ accounts for various forces imparted on the particles, such as lift and user-defined functions. \vec{K}_{qp} and \vec{K}_{DP} describe the interphase momentum exchange coefficients, dependent upon the drag function, volume fraction, density, and the particulate relaxation time. $S_{DPM,explicit}$ is known as the mass source term, which is specified as a constant or user-defined function. A major drawback to using this

multiphase model is that it limits the simulation to using the two-equation k- ε turbulence model.

For transport phenomena in the continuous phase (water) these simulations utilized the two-equation dispersed k- ε model for turbulence prediction. The dispersed k- ε model is a simple eddy viscosity model which modifies the continuous phase turbulence equations with additional terms for interphase turbulent momentum transfer. Similar to the equations above for the discrete phase, the mass and momentum conservation equations for the continuous phase q are

$$\begin{aligned} \frac{\partial}{\partial t} (\alpha_q \rho_q k_q) + \nabla \cdot (\alpha_q \rho_q \vec{U}_q k_q) &= \nabla \cdot (\alpha_q \mu_{t,q} \sigma_k^{-1} \nabla k_q) + \alpha_q G_{k,q} - \alpha_q \rho_q \varepsilon_q + \alpha_q \rho_q \Pi_{k,q} \quad (3) \\ \frac{\partial}{\partial t} (\alpha_q \rho_q \varepsilon_q) + \nabla \cdot (\alpha_q \rho_q \vec{U}_q \varepsilon_q) &= \nabla \cdot (\alpha_q \mu_{t,q} \sigma_\varepsilon^{-1} \nabla \varepsilon_q) + \alpha_q \varepsilon_q k_q^{-1} (C_{1\varepsilon} G_{k,q} - C_{2\varepsilon} \rho_q \varepsilon_q) + \\ &\quad \alpha_q \rho_q \Pi_{\varepsilon_q} \quad (4) \end{aligned}$$

where many of these values are known and described in detail from other works [53]. The important modifications denoted here over the basic k- ε model comes from the Π terms which represent the dispersed phase's contribution on the continuous phase as well as the G term which denotes the production of turbulent kinetic energy. An important point to consider: the model being utilized does not account for any interaction such as momentum transfer or adsorption/desorption mechanics between the discrete particulate phase and the gaseous phase. Each of the two has an impact on the continuous phase and thus the overall bulk interactions are accounted for, but the direct interaction between the two is not.

Results

Three different angles were tested for each geometry orientation of 30°, 45°, and 60° (with respect to the filter base). Along with particle mass flow rates and histograms, the turbulent kinetic energy of the continuous phase (water) and the volume fraction of the gaseous phase (O₂) were also collected (if included in the simulation). The residuals, particle tracks, and contour plots of each simulation can be seen in Appendix A.1 – A.54. To elucidate the impact of a gaseous phase on particle filtration ability, the difference in the particle mass flow rate through the upper and lower outlets was divided by the total inlet rate to retrieve the

filtration as a mass percentage of particles filtered. The results from the simulations can be seen in Figure 2.3 below.

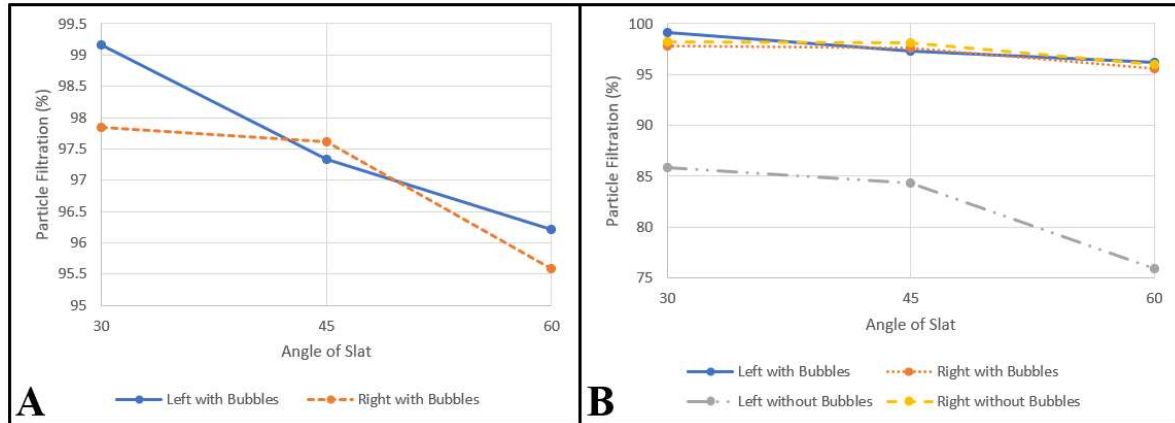


Figure 2.3. Plot of Slat Angle (degrees) vs. Particle Filtration (%) for Left and Right-Oriented Geometries with (A) and without (B) the inclusion of a gaseous phase.

The plot clearly shows that as the angle of the slat is increased for gaseous simulations, the particle separation decreases, more so for the left-oriented geometry than the right-oriented. When the gaseous phase is removed a major impact is seen for the left-oriented geometry wherein more than a ten percent drop in particle filtration ability occurs. One reason for this could be the presence of vortical crossflow [16] in the right-oriented geometry as opposed to the left-oriented. The presence (or lack thereof) of vortical crossflow could place further burden on the gaseous phase to assist in particle migration.

The results of this experiment are twofold; the low residuals and comparable results show that the simulation software is at least capable of handling multiphase flows with low flow velocities while also illustrating a facile example of geometric optimization. A simple algorithmic approach to testing and optimization of this geometry would resemble Figure 2.4.

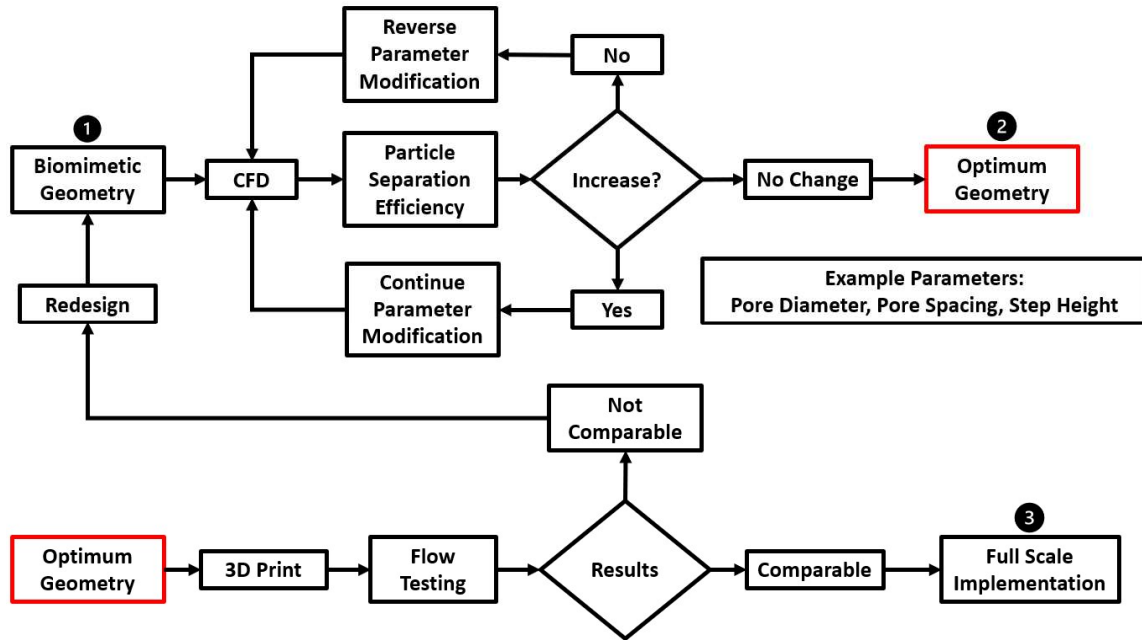


Figure 2.4. Basic CFD-Informed Iterative Geometric Optimization Algorithm.

Consulting with the algorithm diagram in Figure 2.4 would indicate that the slat angle for the gaseous phase simulations should be decreased further from 30° to 15° and the CFD re-run for results. Eventually, the particle separation should form a downward-facing parabolic curve based on the angle, and the apex of said parabola would be the optimum angle. Next, another parameter would be selected, and the same parabola established until each intended parameter has been maximized accordingly. Once a geometry is optimized via this method, it could move to flow tunnel testing for validation (or de-validation).

Moving beyond these elementary multiphase simulations will involve two major steps from the simulation perspective: increased flow rate stability and higher order turbulence modeling. The strength of the vortices during crossflow is clearly dependent upon the flow velocity of the retentate, but proper vortical elucidation while maintaining a fully-resolved boundary layer will require proper treatment.

CHAPTER 3

Wave Minimal Surface Testing

Accepted with Revisions: “Biomimetic crossflow filtration with wave minimal surface geometry for particulate biochar water treatment”, *PLOS Water*, Manuscript Number: PWAT-D-22-00076

Geometry Generation

Prior to any further CFD simulations or experimentation, the surface of interest must be visualized and parameterized. In order to generate the point cloud and mesh for these surfaces the Grasshopper plugin [54] from the CAD software Rhinoceros 3D [55] was used. Grasshopper is a visual programming language which is optimized for generative algorithms and parametric modeling. To produce the surface for the WMS, Grasshopper allows for the evaluation of functions with subsequent meshing of said points through built-in packages. The parameterized functions for the cartesian coordinates of the WMS are denoted below.

$$x(m, u, v) = e^{mu}(\cos u \cosh v + \sin u \sinh v) \quad u, v \in \mathbb{Z}_{>0} \quad (5)$$

$$y(m, u, v) = e^{mu}(\cos mv \cosh v \sin u - \sin mv \sinh v \cos u) \quad (6)$$

$$z(m, n, o, p, u, v) = -e^{mu} \sin nv \left(\frac{\sqrt{1+o^2}}{p} \right) \quad m, n, o, p \in \mathbb{R}_{>0} \quad (7)$$

Where m , n , o , and p are functional parameters and u/v are the grid points for mesh evaluation. As exemplified later, the most impactful of these parameters in the surface shape is n which heavily modifies the maximum width of the surface.

For the first set of WMS testing, the parameters of the surface were kept constant at 0.5 for m , n , o , and p producing the surface seen in Figure 1.2. As shown in the previous chapter, the inclusion of vortices into the crossflow filter are critical to its' success both with and without high flowrate retentate. To that end, this set of CFD simulations were conducted to qualitatively evaluate the vorticity generation of the WMS against an analogue in the MR [49, 50]. The MR is a well-studied vortex generating structure which allows for comparative analysis between the WMS and a known standard. This set of experiments was conducted to

evaluate the overall WMS's ability to generate external vortical flow without the inclusion of particles for filtration. To simplify the simulation set the WMS was left as a surface (thickened slightly to allow for 3D analysis) for the simulations. The simulation was conducted in the computational domain seen in Figure 3.1 with fluid flow in the positive x direction.

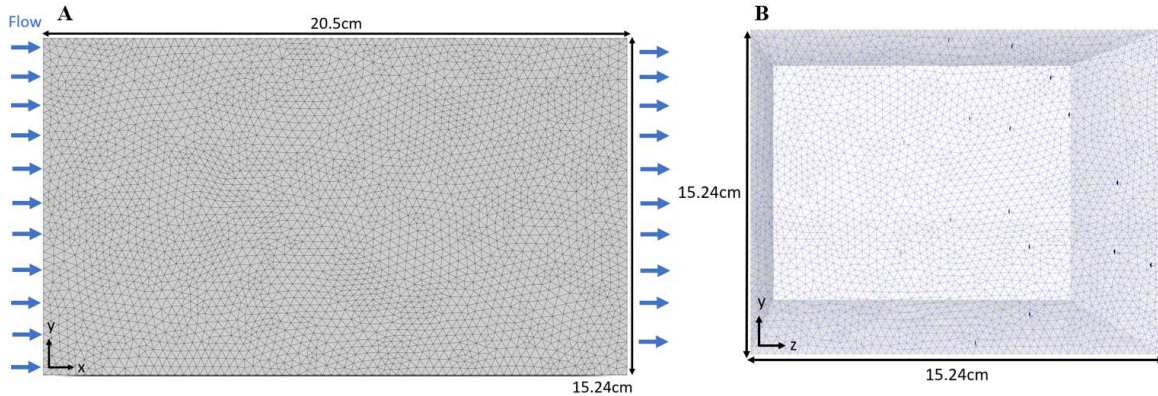


Figure 3.1. Preliminary Vorticity Analysis Computational Domain in the (A) xy -plane. (B) yz -plane.

Simulation Setup

Both sets of CFD simulations were built and tested with the ANSYS 2021 R2 software package using the Fluent case solver. The computational domain for each simulation was built to mirror the dimensions of the water tunnel used for validation. This assumed the geometry to be evaluated was placed on a flat plate at the center of the flow region and the geometry itself accounted for less than 10% of the total flow area. Each set of simulations also utilized the Reynolds stress model (RSM) for turbulence prediction, the RSM modifies the two-equation k - ϵ turbulence model used previously by neglecting the assumption of isotropic eddy-viscosity leading to seven additional transport functions for 3D cases. The exact form of these equations for the Reynolds stress ($\overline{\rho u'_i u'_j}$) transport can be seen below.

$$\frac{\partial}{\partial t} (\overline{\rho u'_i u'_j}) + C_{ij} + D_{T,ij} + P_{ij} + G_{ij} + \epsilon_{ij} + F_{ij} = D_{L,ij} + \varphi_{ij} + S \quad (8)$$

Where C_{ij} , $D_{L,ij}$, P_{ij} , and F_{ij} require no further continuum assumptions and describe the convection, molecular diffusion, stress, and system rotation respectively. To produce a tractable solution set $D_{T,ij}$, G_{ij} , ϕ_{ij} , and ε_{ij} , which denote the turbulent diffusion, buoyancy, strain, and dissipation, must be modeled from further assumptive models. Deeper investigation as to the modeled assumptions of the RSM are not discussed here, see other works for details [56]. The RSM was chosen because it is best optimized for flow cases where the geometry or the strain rate tensor is believed to be complex in nature with significant sections of swirling flow [52, 57]. As the WMS structures show both complex hyperbolic geometry as well as vortex generation ability, the RSM was chosen to properly model the anticipated system.

The simulations were done for a single fluid phase with the flow properties equal to that of water at 25°C. The WMS was tested for two configurations as shown in Figure 1.5; the first was done with the crest of the wave oriented into the flow (termed WMS) and the other had the crest oriented downstream of the flow (termed reverse WMS). Each of the geometries were kept at the same characteristic length of 2 mm, taken as the longest chord line of the structure. To see how subsequent downstream geometries would behave in vortex generation, two rows of four structures (placed 5 mm apart) were tested for each case (MR, WMS, and reverse WMS). Finally, each simulation was rerun for inlet fluid velocities ranging from 0.03 to 0.3 meters per second.

After the simulations were complete the average x -vorticity was calculated at several points along the domain to elicit the vortex generation ability of each. More specifically, the cartesian vorticity in the yz -plane which is defined as the x component of the curl of the velocity field shown below.

$$\nabla \times \vec{v} = \left\langle \left(\frac{\partial v_z}{\partial y} - \frac{\partial v_y}{\partial z} \right), \left(\frac{\partial v_x}{\partial z} - \frac{\partial v_z}{\partial x} \right), \left(\frac{\partial v_y}{\partial x} - \frac{\partial v_x}{\partial y} \right) \right\rangle \quad (9)$$

Averaging the x -vorticity was done in order to minimize any errors in evaluating the vorticity over a single surface/geometry. The spacing values were chosen after initial vorticity testing to ensure that the vortices generated from each geometry did not interfere with the vortices of subsequent geometries. As the purpose of the final 3D design is meant to act as a standalone filtration device (and not solely a filter surface modification), the vorticity was only

evaluated shortly before/after the structure as well as over the length of the structure itself and plotted accordingly.

Vorticity Analysis

Vortex analysis and identification is an extremely detailed subject within the field of fluid simulation theory [47]. Vortices are most often described as physically stable eddies which do not decay via a turbulent cascade and rotate about a fixed axis in the flow domain. Vortices are not inherent products of turbulence like eddies, but their strength (rate of rotation) is directly dependent on flow velocity which can produce turbulent effects as it increases [58]. The simplest mathematical definition for use in vortex identification comes from the stream function. Given two points a and b , the stream function in cartesian coordinates is defined below.

$$\psi = \int_a^b (udy - vdx) \quad (10)$$

Which applies to 3D axisymmetric and divergence-free flow fields. Applying this to the definition of vorticity described previously produces the stream function definition of vorticity.

$$\nabla \times \vec{u} = -\nabla^2 \psi \quad (11)$$

Unfortunately, while this is a simple definition to use and analyze, the two dimensional restriction makes it impractical for use with the targeted large swirling three dimensional flows of this work.

Beyond that, two prominent and stable criterion exist for identification of three dimensional vortices: Q and λ_2 . The Q criterion originates from a proposed vortex definition using an invariant of the velocity gradient tensor ($\nabla \times \vec{u}$). More specifically, the Q criterion proposed that a vortex core (a region near or on the vortex rotational axis) is any region which produces complex eigenvalues of the velocity gradient tensor [59]. Writing this condition assuming incompressible flow produces the following characteristic equation.

$$\left[-\frac{1}{6}(u_{i,j}u_{j,i}) \right]^3 + \left[\frac{1}{2}det(u_{i,j}) \right]^2 > 0 \quad (12)$$

Where the cubic component is termed Q and is interpreted as the pressure source in the Navier-Stokes equations where a vortex core is said to occur in regions of minimum Q values. The work from Melander and Hussain (1993) detailed that for the core of

axisymmetric vortices the condition in the previous equation is met because $Q > 0$ [60]. However, work from Jeong and Hussain (1995) concluded that a $Q > 0$ does not necessarily imply a pressure minimum within the bounded region of interest as the minimum could occur at the boundary itself [47]. That conclusion undermines the usage of the Q criterion and thus a new definition, λ_2 , was created as an attempt to circumvent that pressure minimum issue.

The λ_2 criterion sprouted from a new definition which alleviated the inconsistency found between the coexistence of a pressure minimum and a vortex core. Jeong and Hussain (1995) attributed this inconsistency to two effects: unsteady strain and viscous effects which is what they discarded in order to define the criterion. Taking the gradient of the Navier-Stokes equations and retrieving the symmetric components leads to the following:

$$-\frac{1}{\rho} P_{ij} = \frac{DS_{ij}}{Dt} - \nu S_{ij,kk} + \Omega_{ik}\Omega_{kj} + S_{ik}S_{kj} \quad (13)$$

Where the unsteady strain and viscous effects are denoted in the first two terms on the righthand side respectively. Neglecting these terms produces the new vortex definition as a “connected region with two negative eigenvalues of $\Omega_{ik}\Omega_{kj} + S_{ik}S_{kj}$ ” [47]. For \mathbb{R}^3 this product will have three eigenvalues where the median eigenvalue (λ_2) is said to be within a vortex core for $\lambda_2 < 0$. Much more work has been done evaluating the robustness [61] and accuracy [62] of this definition, but exploration of that is deferred to other works [63].

For this set of simulations, the λ_2 criterion was utilized for vortex isosurface plots because it has shown to be the most robust for a large variety of vortical topologies as well as low Reynolds number flows.

Results

After running the simulations for each geometry, the average x -vorticity over both the first and second rows was plotted. Both the WMS and reverse WMS showed higher average vorticities than the MR, but all geometries displayed a clear drop in vorticity moving from the first to second row.

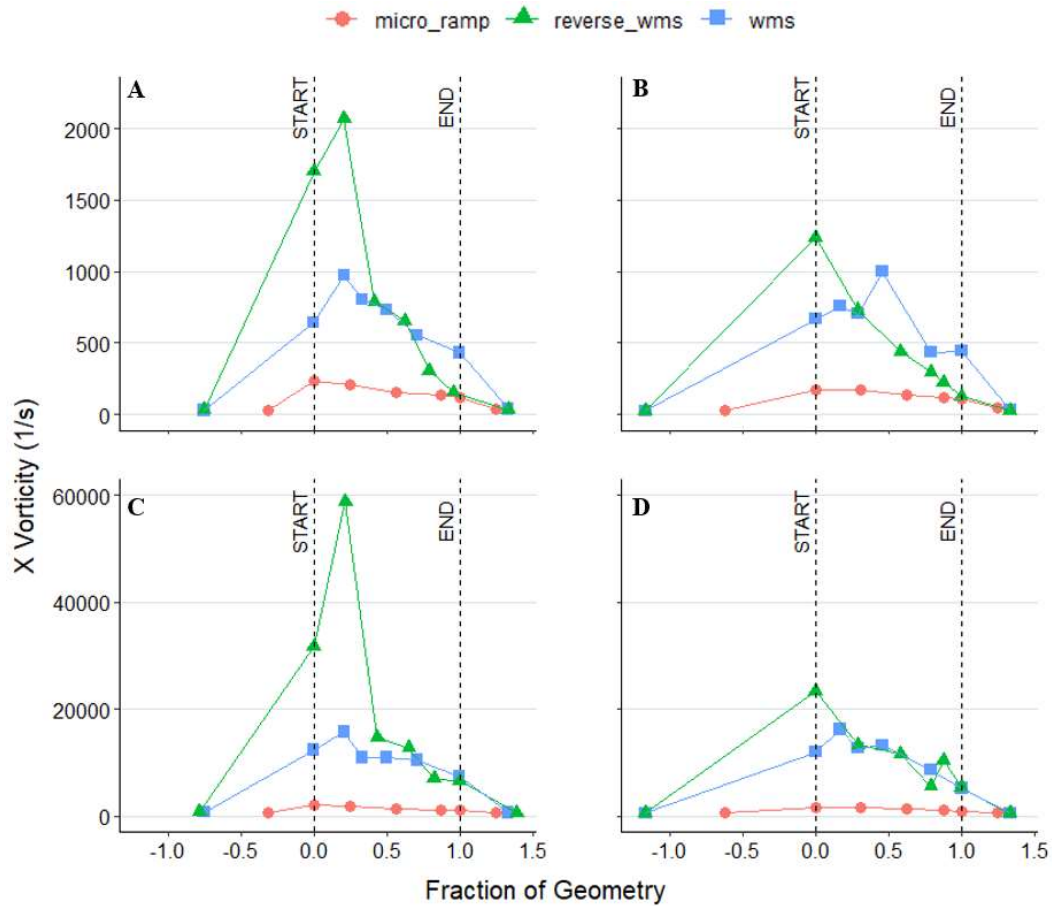


Figure 3.2. Average x -Vorticity Along Computational Domain. (A) x -vorticity of the first row of each geometry with inlet fluid velocity of 0.03 meters per second. (B) x -vorticity of the second row of each geometry with inlet fluid velocity of 0.03 meters per second. (C) x -vorticity of the first row of each geometry with inlet fluid velocity of 0.3 meters per second. (D) x -vorticity of the second row of each geometry with inlet fluid velocity of 0.3 meters per second.

Beyond that, the data clearly indicates that the reverse WMS produces significantly more x -vorticity than the WMS, but the WMS overtakes the reverse WMS near the end of the structure. This is most likely due to the translation of fluid momentum into a rotating flow regime (vortex) wherein the WMS does not convert the inflowing fluid into a vortical flow pattern as efficiently or as strongly as the reverse WMS does. Doing so would cause some vorticity increase as shown but would also conserve more of the linear momentum (in the x direction) of the fluid which then can contribute to stronger downfield vorticity. Along with the increased average vorticity, the disparity in the peak vorticity as fluid velocity increases

also benefits the reverse WMS. This again implicates the reverse WMS in efficiently converting fluid linear momentum into a vortical structure.

To visualize the vortex disparity between the WMS and reverse WMS, contours of the x -vorticity were plotted at the same plane in the second row of geometries (Figure 3.3 A/C) for an inlet flow velocity of 0.3 meters per second. Along with these contours, isosurfaces were created (Figure 3.3 B/D) using a λ_2 value of 154 and colored by x -vorticity to visualize the vortices at the same velocity.

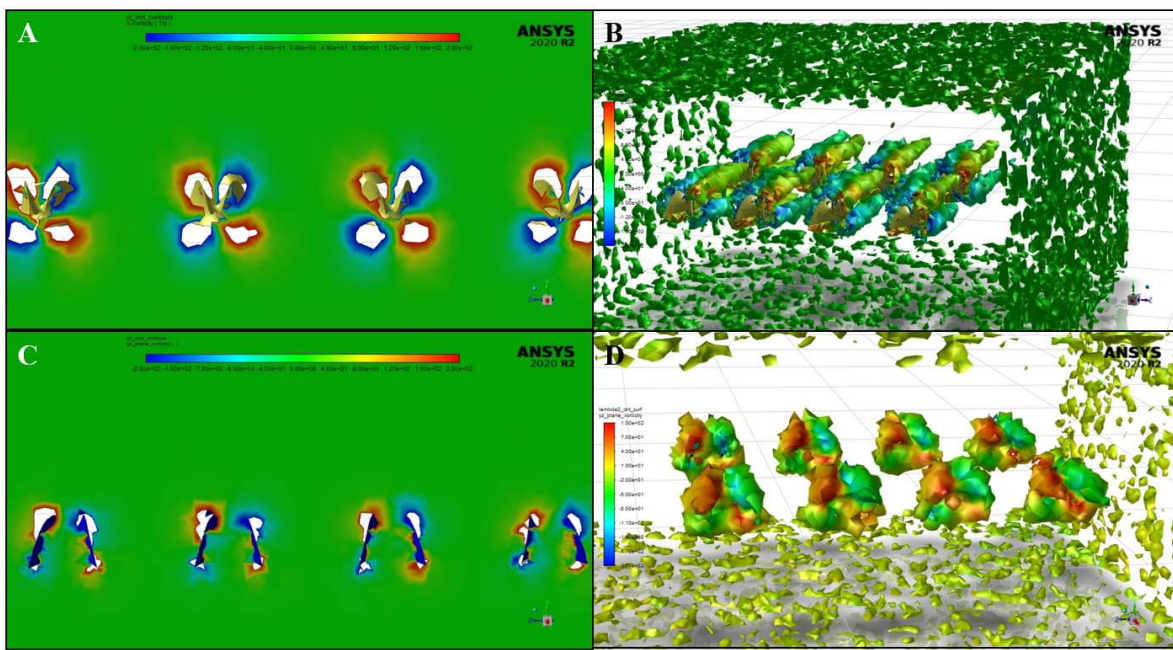


Figure 3.3. x -Vorticity Isosurface Plots. (A) Contour plot for reverse WMS colored by x -vorticity. (B) Isosurface of λ_2 criterion for reverse WMS colored by x -vorticity. (C) Contour plot for WMS colored by x -vorticity. (D) Isosurface of λ_2 criterion for WMS colored by x -vorticity.


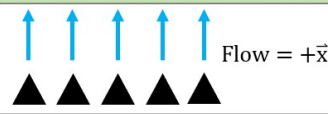

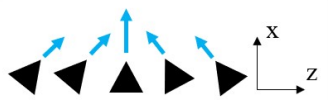

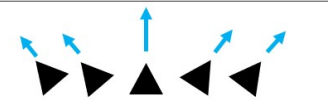

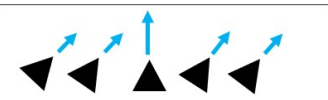



Both the contour plots as well as the isosurfaces detail the clear delineation in vortex form and strength shown by the reverse WMS. The reverse WMS displays clear and elongated vortices downfield of the flow whereas the vortices from the WMS are clearly malformed and weaker. In order to incorporate these findings, the parameterized set of simulations were conducted using the reverse WMS configuration along with higher inflow velocities starting at 0.2 meters per second.

Beyond the reverse WMS, another potential optimization was attempted. As seen in the previous testing, the two rows of geometries were oriented with the flow either into or against it, but no modification was done to the size of the geometries or non-parallel flow orientations. Thus, a small exploration was conducted into the impact of these two parameters. However, for this testing, particles were included in the same manner as the initial multiphase testing.

Flow Orientation Testing

The same computational domain and coordinate system as shown in Figure 3.1 was used for this testing, but two rows of five geometries were used instead of four to allow for greater variability in the size distribution of the geometries. Along with that, ~500 carbon particles with a diameter of 50 microns were injected at the inlet to best illustrate the full suite of parameters being tested, Table 3.1 details the different size distributions of the geometries as well as the orientation of the geometries (termed angle of fluid incidence).

Table 3.1. Parameter Suite for Size and Orientation Testing of Reverse WMS Array.

Label	MVG Size Distributions	Label	MVG Angle of Fluid Incidence
1		A	
2		B	
3		C	
4		D	
5			
6			
7			

For further illustration of the parameters, Figure 3.4 details an example of both 1C and 1A from different perspectives along with the fluid flow direction.

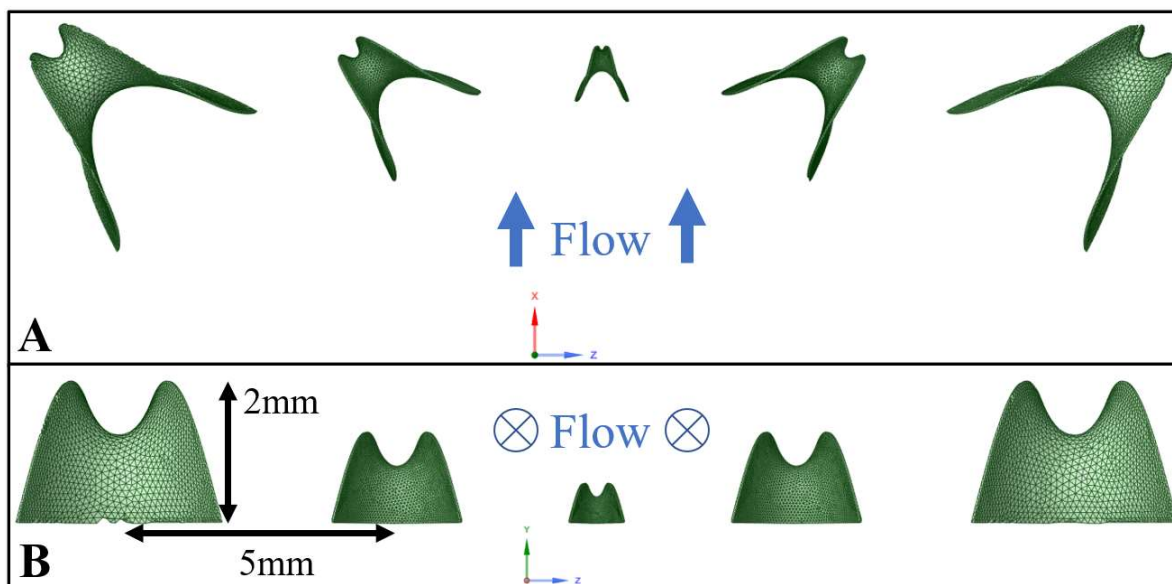


Figure 3.4. Examples of Different Parameter Configurations. (A) Configuration 1C as seen from the xz -plane. (B) Configuration 1A as seen from the yz -plane.

The full exhaustive set of these configurations produced a total of 28 different configurations which were analyzed for their contribution to particle disturbance. In order to avoid errors in the particle dispersion between simulations, each configuration was repeated 200 times and the particle data in the yz -plane was collected at 5 mm beyond the second row of geometries.

The overall purpose of the configuration testing was to see how the geometries would impact the injected particles; with an “optimum” configuration being that which caused the greatest disturbance to the particles in the y and z direction as the goal was to use the generated vortices to act as a shuttle or migratory agent for the particles to better facilitate filtration. To begin analyzing the results of the simulations, the particle velocity components in the yz -plane were plotted to see if there was a major contribution from any configuration (Figure 3.5). The remaining plots for each geometry distribution (2-7) can be seen in Appendix A.55 – A.60.

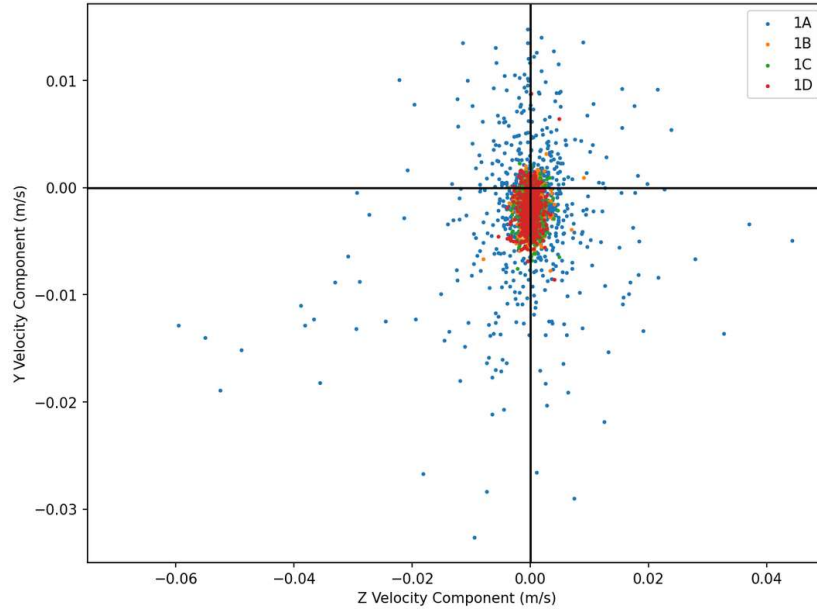


Figure 3.5. *Y* and *Z* Velocity Components of each Particle at an *x* position of 5 mm beyond the second row of geometries for Geometry Distribution 1.

Figure 3.5 shows configuration 1A is causing a much greater dispersion amongst the particles than others but quantifying the difference between each configuration is not inherently simple thus we turn to statistical analysis.

To quantify the impact of each configuration, exploratory factor analysis was conducted in an attempt to elucidate latent features from the data in order to find those configurations which produced the greatest particle dispersion. Exploratory factor analysis (EFA) is a basic statistical methodology which allows for potentially extracting latent variables from a dataset, these latent variables can then be attributed to specific contributing factors which caused the data to be generated [64]. For this work, regardless of the inferential capabilities of these latent factors, the impact on these factors by each configuration could be useful in attributing the particle dispersion between one configuration and another. Prior to conducting EFA, a couple tests are performed in order to evaluate the data's usefulness when it comes to extracting latent variables. Those tests are known as Bartlett's test of sphericity [65] and the Kaiser-Meyer-Olkin (KMO) test [66].

Bartlett's test is done to evaluate the correlation matrix of the data to ensure it is dissimilar to the identity matrix, otherwise that would imply no significant relationship exists between the data and variables. Comparing the correlation matrix to the identity matrix

requires simply calculating the χ^2 test statistic along with the P value for the matrix. The data will be considered minimally sufficient if the resulting P value is significant. Bartlett's test is seen as a minimally sufficient condition for the use of EFA as many datasets can pass Bartlett's test while still being poor contenders for EFA.

The KMO test is done to assess the sampling adequacy of a dataset and indicate if there may be some common variance amongst the tested variables. The KMO test produces a criterion from the equation

$$KMO = \frac{\sum_{j \neq k} \sum r_{jk}^2}{\sum_{j \neq k} \sum r_{jk}^2 + \sum_{j \neq k} \sum p_{jk}^2} \quad (14)$$

where r_{jk} and p_{jk} are the correlations and partial correlations of the j^{th} and k^{th} variables respectively. The KMO test is a more stringent test than Bartlett's test and instead of classifying the dataset/variables into a binary class it produces a value which lies within a range from poor to excellent for use in EFA.

Each set of particle data had four features, y and z positions as well as y and z velocity components. Conducting the Bartlett and KMO tests on each feature produced Table 3.2.

Table 3.2. EFA Analysis Results. *Value Below 1e-10

EFA Analysis		χ^2	P Value*	KMO Value
Velocity	Y	3265.28	0	0.5006
	Z	3468.75	0	0.4996
Position	Y	74252.08	0	0.5121
	Z	79986.72	0	0.5000

As shown in Table 3.2, the results of the Bartlett test very strongly indicate that the dataset and variables are not significantly similar to the identity matrix and thus EFA is at least feasible for this data. However, the KMO results all show a value near 0.5 which is considered to be the bare minimum value for an EFA dataset with 1 being considered the best and 0 being the worst [67].

Now that EFA was at least shown to be feasible for this data, the number of factors must be derived in order to evaluate them or make any type of theoretical inference regarding them. To do this, the scree test is used; the scree test plots the eigenvalue for each number of factors. As the number of factors increases the eigenvalue will decrease and the best number

of factors is said to be either past the point of maximum curvature or at least below the maximum KMO criterion value of 1. A scree test was conducted for each of the four variables (y/z position and velocity components) and then the optimum number of factors was evaluated. Figure 3.6 details the scree plot for y position; the remaining plots can be viewed in Appendix A.61-63.

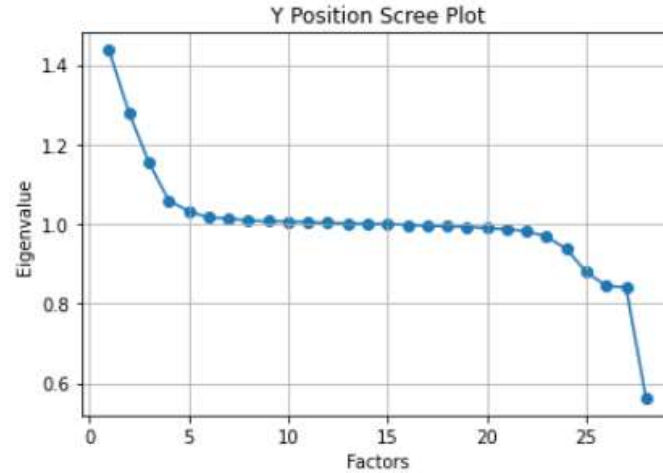


Figure 3.6. Scree Plot for Particle Y Position.

As shown in Figure 3.6, the eigenvalue drops as the number of factors increases with an eigenvalue of 1 corresponding to the theoretical minimum number of factors based on the KMO criterion. Repeating this test for each variable produces an average of 13 factors for use in EFA. In order to evaluate the contribution of each factor on the dataset, the factor loading value is determined.

Factor loading expresses the correlation of each factor to a corresponding variable. Statistically speaking, that correspondence value is attributed to the variance induced by that variable on that particular factor. The factor loading values are those values which minimize the mean square error of the residuals in the correlation matrix such that the below exists at a minimum [68].

$$\varepsilon^2 = \sum_{a \neq b} (\sum_i z_{ai} z_{bi} - \sum_j l_{aj} l_{bj})^2 \quad (15)$$

Where a and b are dimensions of the correlation matrix; i and j are the observation and factor respectively; and z and l are the normalized data value and factor loading respectively. Due to the nature of this specific modeling case, the exact theoretical latent variable that the factors

represent is not inferable, but the trend amongst the factors themselves does provide some information as to the system and its' behaviors. Computing the factor loading for each variable produces a heatmap (Figure 3.7) which denotes the strength of loading of individual factors from -1 to 1 for each configuration. The purpose of this portion is to evaluate the factors that have high loading between all (or most) of the variables. Those configurations which show high factor loading for multiple variables are seen to be those which produce high particle dispersion because they are modeled well from the collected data.

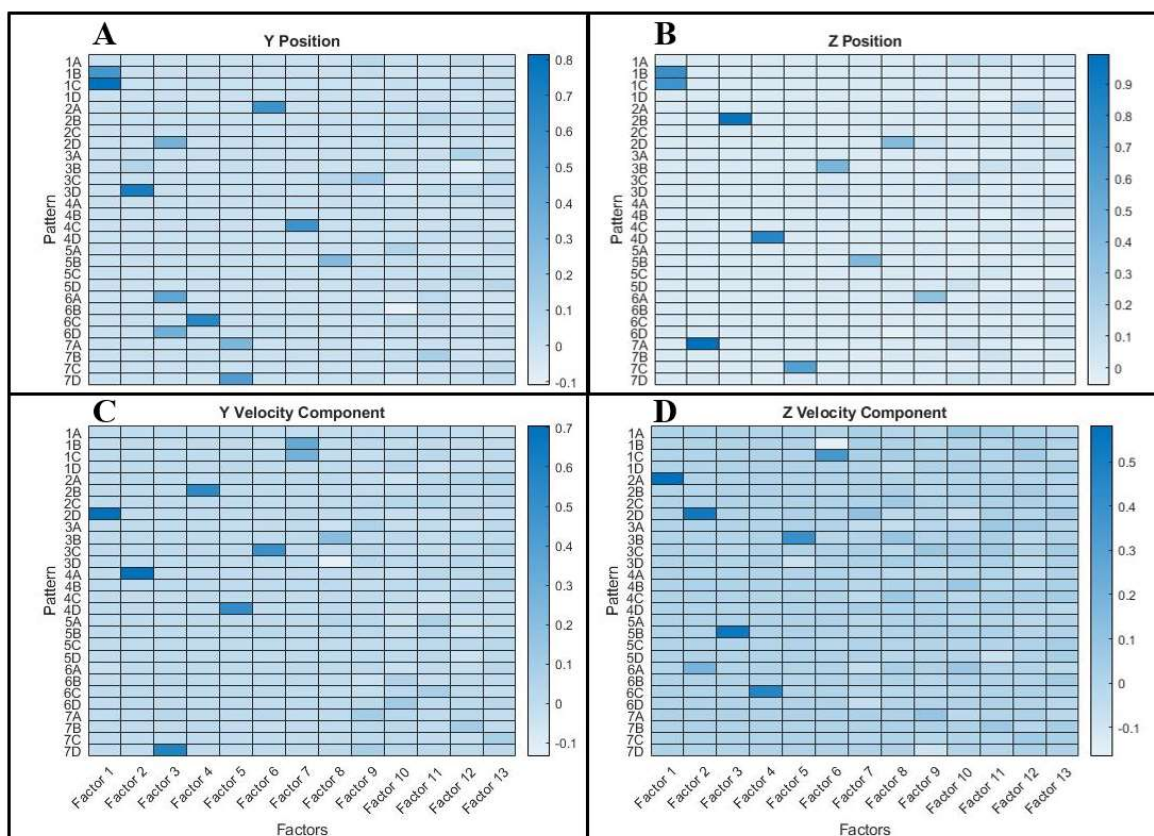


Figure 3.7. Factor Loading Heatmaps for (A) y Position, (B) z Position, (C) y Velocity, and (D) z Velocity.

Figure 3.7 shows a number of strong loading factors such as from factor 1 in Figure 3.7A-B for configurations 1B and 1C. An important consideration from these results is that each of the variable EFAs were done independently of one another. Meaning that factors from one test could potentially be capturing the same latent phenomenon that another factor for a different variable is. For example, a strong factor loading can be seen in Figure 3.7C for

configuration 2D from factor 1, but a similar loading is also seen for 2D in Figure 3.7D but from factor 2.

After analysis of the factor loading, the final configuration matrix (Figure 3.8) can be constructed to denote those configurations which are more strongly associated with particle dispersion from the EFA results.

1A	1B	1C	1D
2A	2B	2C	2D
3A	3B	3C	3D
4A	4B	4C	4D
5A	5B	5C	5D
6A	6B	6C	6D
7A	7B	7C	7D

Figure 3.8. Configuration Matrix Post-EFA. Configurations promoted by EFA are stripped.

As seen in Figure 3.8, the results were able to narrow the field of potential configurations to some extent, but further work is need in order to reduce the set into a more feasible number for testing. Another potential way to predict the behavior of particles from these configurations would be to apply hierarchical agglomerative clustering in order to evaluate the particle data in an attempt to cluster the particles into regions of high dispersion and low dispersion. One such example of this can be seen in Appendix A.64, but much more work would need to be done in order to tune the clustering for use in optimum configuration prediction.

CHAPTER 4

Parameterized Filtration Testing

Geometry and Boundary Parameters

Another hurdle prior to utilizing the WMS lies in the fact that it is (at this point) a parameterized two-dimensional surface and thus has no inherent ability to filter particulate flows. Therefore, to create a 3D filter design from these 2D surfaces, a thickening of the surface must be done along with inclusion of at least one filter pore for filtrate flow. To address this, a second surface was produced on top of the original with the outer boundaries of the WMS being used as guiderails for fitting. The second surface was fit offset to the original using an iterative soap film function as to also be a minimal surface itself. From there the volume between the two was filled with a filter pore at the mid-plane of the design which extended from the outer surface to the base of the structure (Figure 4.1A-B). Placement of the pore at the mid-plane was done to provide the pore with maximum fluid velocity over the backward step of the mouth to favor vortex-induced shielding.

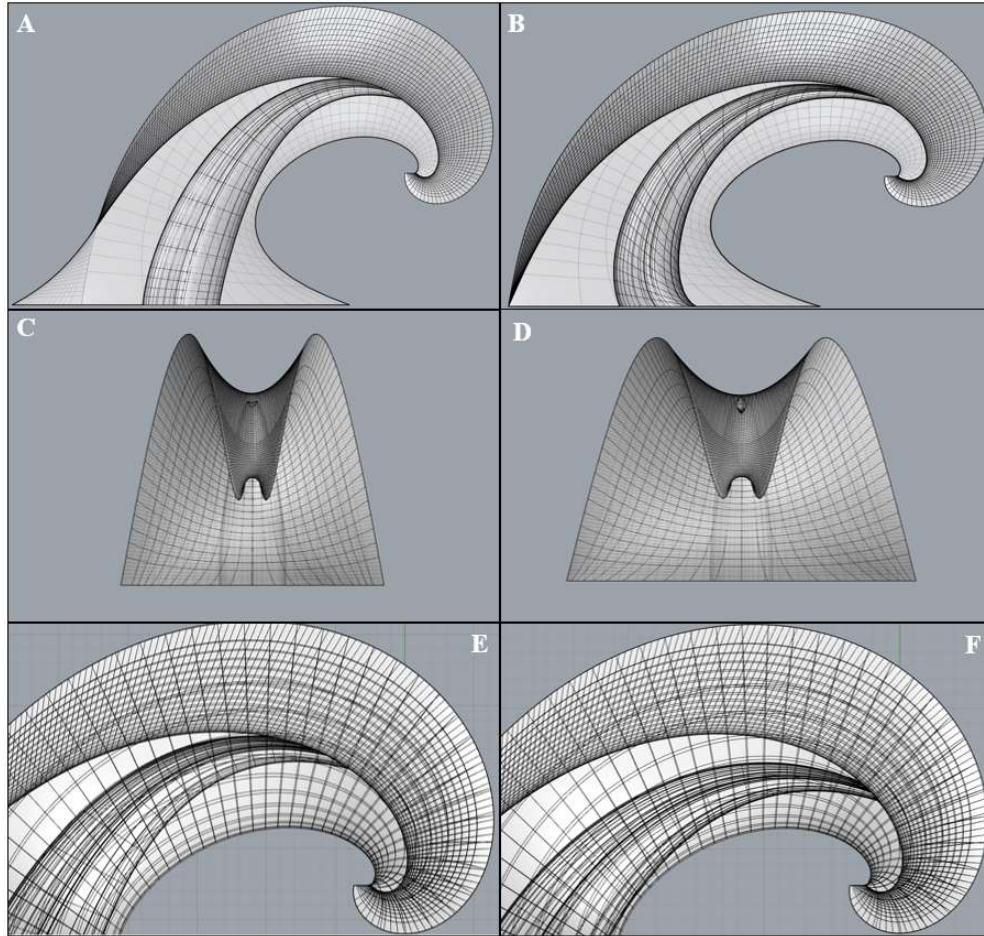


Figure 4.1. WMS 3D Filter Design Parameters. (A) Convex leading edge which provides softer initial incidence with fluid. (B) Flat leading edge. (C) Maximum width for $n=0.5$. (D) Maximum width for $n=1$. (E) Angle of fluid incidence of 90° . (F) Angle of fluid incidence of 40° .

Now that the WMS had a 3D design, further consideration had to be paid as to the structural parameters which will be modified here as well. Considering all the available functional parameters and 3D structural parameters this work focused on three specific attributes: leading-edge morphology, maximum width, and angle of fluid incidence. The leading-edge morphology (Fig 4.1A-B) is concerned with the form factor of the edge which first contacts the fluid stream. Two different forms of the leading-edge were considered in this study: flat and convex. Flat simply means that the leading edge of the 3D filter design is sharp and cuts off succinctly at the boundary of the WMS. Convex in this context refers to the flat leading edge being replaced with a parabolic function which is modified such that the

apex of that parabola is 25% offset from the original bounding edge of the WMS. The purpose of this modification was to produce a smoother fluid contact area to reduce momentum loss in the fluid due to that initial contact/shear. The maximum width parameter (Figure 4.1C-D) is controlled by the variable n from the WMS cartesian equations. The present study evaluated values of 1 and 0.5 for n , where an n of 0.5 produces the smaller width form shown in Figure 4.1C and an n of 1 widens the WMS (Figure 4.1D). These values were chosen because values below 0.5 begin to produce geometries which are not self-supporting and thus are troublesome for additive manufacturing. Values of n beyond 1 quickly cause the WMS to become a bluff body which does not generate meaningful vorticity. The parameter termed angle of fluid incidence (Figure 4.1E-F) denotes the angle of the backstep with respect to the fluid for the filter pore. In this work two angles were tested, 90° seen in Figure 4.1E and 40° seen in Figure 4.1F. The 90° angle was chosen as that is standard for backstep flow while 40° was chosen as it provided a filter pore set further forward in the WMS while maintaining the effective pore diameter. The size of the filter pore, while important, was not modified between trials and was kept at a constant diameter of 1.35 mm as that size provided a smooth filter pore from the outer surface to the base of the geometry.

After completion of the CFD simulations, the optimum WMS design was 3D printed with black ABS filament using a Stratasys F370 3D printer for water tunnel testing. Prior to experimental testing, special care was also taken to smooth the surface of the print.

Simulation Setup

Succeeding the preliminary vorticity analysis, a new set of simulations were constructed to evaluate the filtration potential of the WMS. To do so the WMS was converted into a three-dimensional substrate and parameterized as described previously. To test the parameters in a reasonable timeframe the parameter space was not evaluated exhaustively, but instead done via independent component testing. In other words, the parameters were evaluated in order of perceived impact to the system flow dynamics. That resulted in an order of parameter testing such that maximum width was first, angle of fluid incidence was second, and leading-edge morphology last.

The new set of simulations were built such that the bottom face of the filter pore on the 3D WMS structures was a separate outlet along with the end of the computational domain as seen previously. The fluid phase of the simulation mirrored that of the previous set with an additional neutrally buoyant solid particulate phase being injected along with the inlet. Along with the different structures denoted in Figure 4.1, each simulation was also evaluated over varying inlet fluid velocity, filtrate outlet pressure, and particle size. The inlet fluid velocity was tested from 0.2 to 0.4 meters per second while the particle size was shifted from 50 microns up to 1 mm and the filtrate outlet pressure was analyzed from 0 to 35 kPa to indicate a small amount of vacuum/negative pressure. The results of these simulations were evaluated for filtration efficiency via two metrics: filtrate flux ratio and filtrate particle count.

Experimental Flow Validation

Experimental flow validation was performed utilizing a 65 gallon water tunnel pictured in Figure 4.2. The tunnel visualization section is 45.72 cm in length with a 15.24 cm² square cross section with fluid flow calibrated for velocities in the range of 0.014 to 0.409 m/s.



Figure 4.2. 65 Gallon Water Tunnel for Flow Validation Experiments.

To measure the velocity field within the tunnel, 2D particle image velocimetry (PIV) was utilized. PIV involves measuring the change in position over time of silver-coated neutrally buoyant spheres that are seeded in the tunnel [69]. To measure the position of the particles

over time requires the use of a 200 mJ Nd:YAG double pulsed laser which emits a field of pulses at a rate up to 15 Hz. The illumination of particles by this field and the change of position for the particles between pulses produces the velocity field of the particle-entraining fluid [70]. The current work focused on comparing a 2D velocity field of the flow about the midplane of the optimized geometry based on results from the CFD as denoted in Figure 2.4. To simulate the outflow of fluid through the filter pore, the EFD was constructed with the WMS geometry inverted and an outlet tube connected such that water was flowing out of the outlet during each test. After calibration of the PIV capture system, the final field of view was a 200 mm by 100 mm region surrounding the printed geometry. The calibrated analysis region setup including the printed WMS geometry can be seen in Figure 4.3.

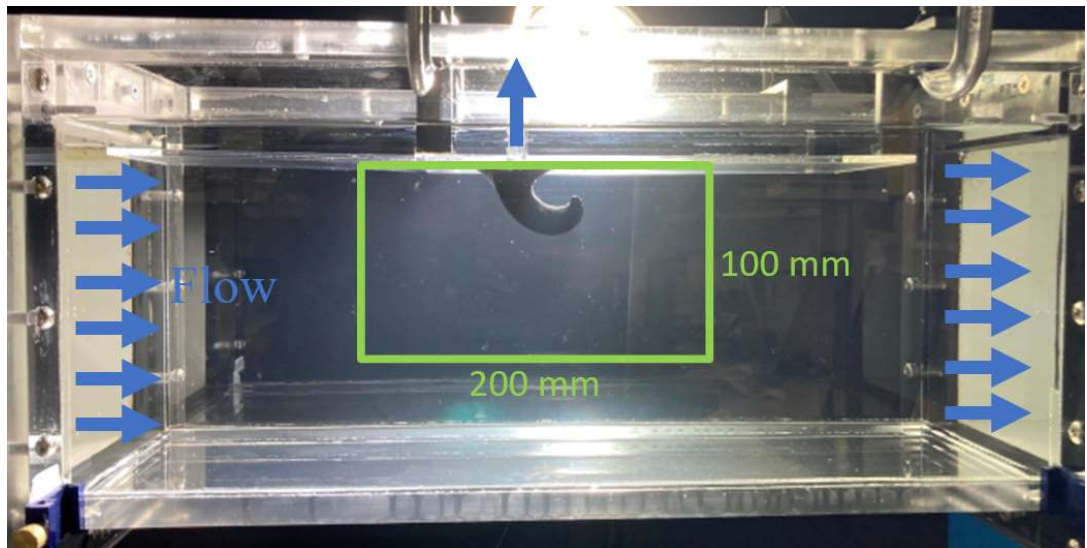


Figure 4.3. Configured Flow Tunnel Experimental Setup with PIV and WMS.

Results

After completing the set of simulations varying all the previously denoted geometric parameters and simulation conditions, the filtration efficiency of each was evaluated. For each simulation, the inlet particle stream consisted of ~5000 particles of a uniform diameter, with the diameter being modified between runs. All the simulations showed high particle filtration efficiency with the lowest efficiency coming out to be 99.4%. Due to this result, the simulations were first analyzed for filtrate flux to determine which structure provided the

highest filtrate flow considering the similar rate of particle exclusion. The filtrate flux was evaluated as the fraction (as a percentage) of mass flow out through the structure to the total inlet mass flow (see Figure 4.4).

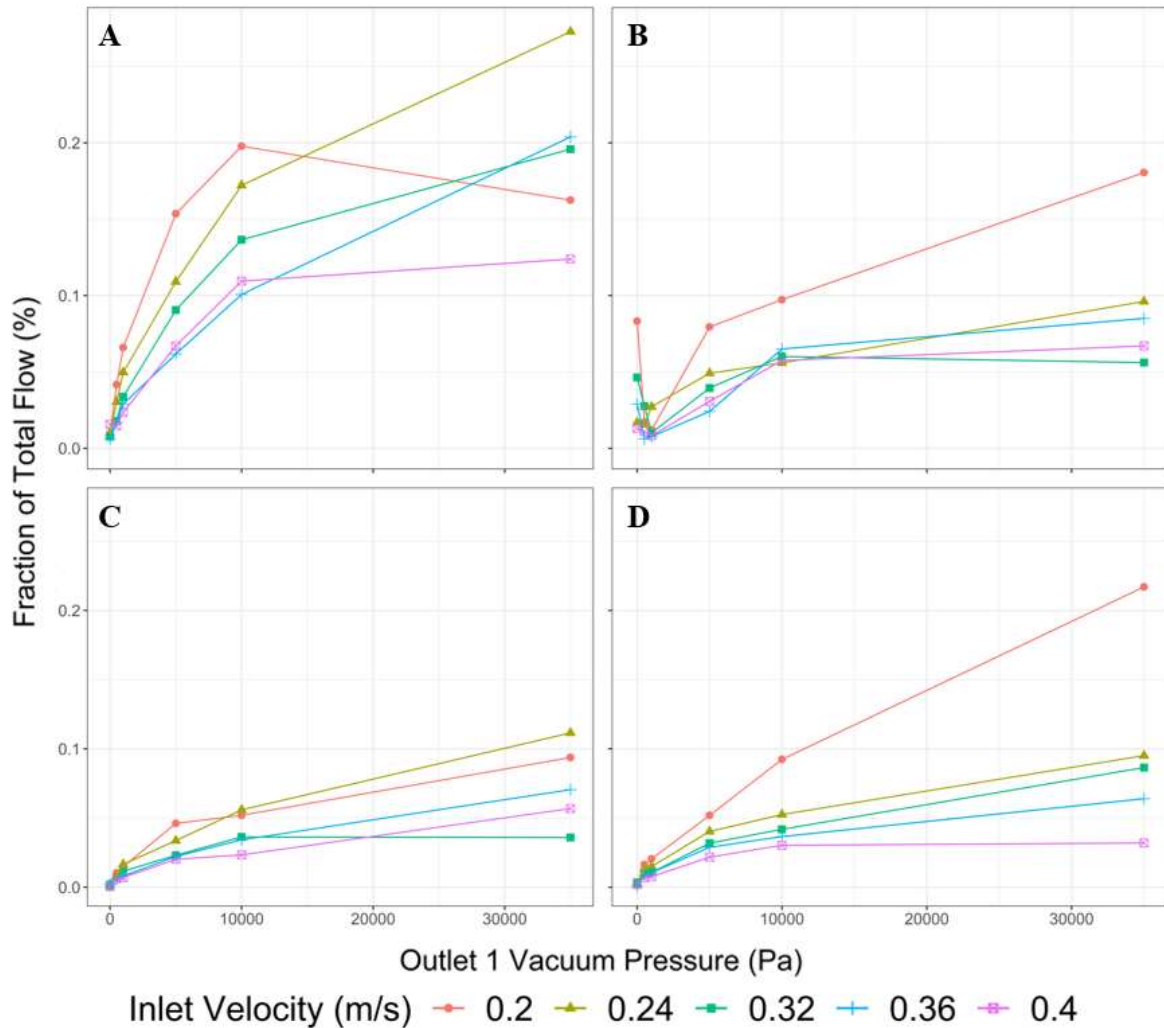


Figure 4.4. Filtrate Flux as Percentage of Total Mass Flowrate. (A) Fraction of total flow as a function of filtrate outlet pressure for a structure with a convex leading edge, maximum width of $n=1$, and angle of fluid incidence of 90° . (B) Fraction of total flow as a function of filtrate outlet pressure for a structure with a flat leading edge, maximum width of $n=1$, and angle of fluid incidence of 90° . (C) Fraction of total flow as a function of filtrate outlet pressure for a structure with a convex leading edge, maximum width of $n=0.5$, and angle of fluid incidence of 90° . (D) Fraction of total flow as a function of filtrate outlet pressure for a structure with a convex leading edge, maximum width of $n=1$, and angle of fluid incidence of 40° .

All geometric cases show an increase in filtrate flux as more negative pressure is applied to the filtrate outlet. The sole exception being the flat leading edge which quickly drops off in filtrate flux up to 1 kPa, but then returns to the similar logarithmic trend by 5 kPa. Another phenomenon observed in the data is the lower inlet fluid velocity producing higher filtrate flux. This is attributed to the Venturi effect over the filter pore; as fluid velocity increases, so too does the shear stress applied to the fluid near the mouth. If the force induced from the Venturi effect overcomes the pressure applied at the filtrate outlet, the fluid flux would invert, and no filtration would occur. However, the results show what is to be expected, as more negative pressure is applied to the filtrate outlet, the filtrate flux increases even with increasing fluid velocity.

To properly refine further analysis, the geometry with a convex leading edge, maximum width of $n=1$, and angle of fluid incidence of 90° (hereafter referred to as C19) was chosen as the optimum structure design from the previous results. This was because the C19 filtrate flux exhibited the strongest response to both filtrate pressure and inlet velocity, outperforming the other structures with only 10 kPa of pressure. Now the particle diameter behavior can be elicited for this optimized case by looking at the particle count through the filtrate outlet at various inlet velocities, outlet pressures, and particle diameters.

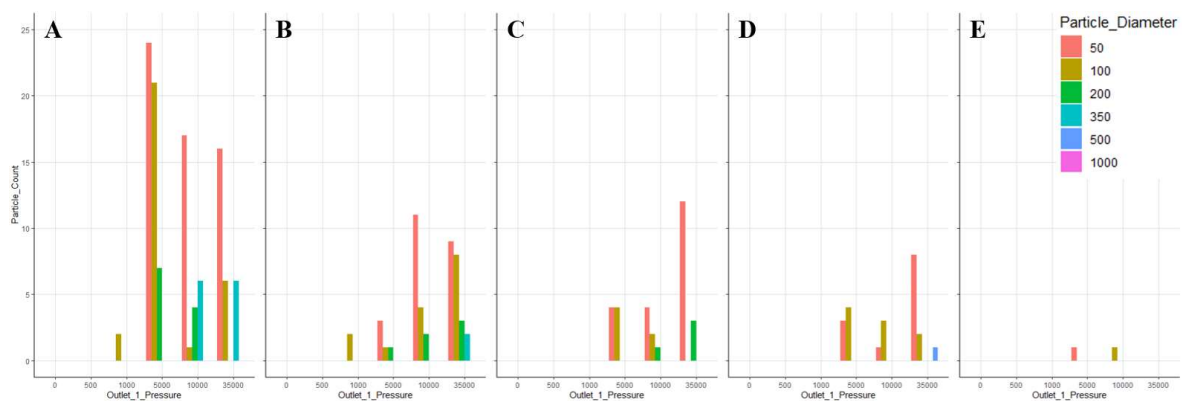


Figure 4.5. Particle Count for C19 Simulations. (A) Particle count partitioned by diameter as a function of outlet pressure for an inlet velocity of 0.2 meters per second. (B) Particle count partitioned by diameter as a function of outlet pressure for an inlet velocity of 0.24 meters per second. (C) Particle count partitioned by diameter as a function of outlet pressure for an inlet velocity of 0.32 meters per second. (D) Particle count partitioned by diameter as a function of outlet pressure for an

inlet velocity of 0.36 meters per second. (E) Particle count partitioned by diameter as a function of outlet pressure for an inlet velocity of 0.4 meters per second.

From Figure 4.5 a clear trend can be observed in the reduction of particle count due to the increase in fluid velocity. Another result shows that neither 0 nor 500 Pa exhibited any particles through the filtrate regardless of inlet fluid velocity. This is attributed to the drastically lower filtrate flux observed previously at low outlet pressures due to the Venturi effect over the pore. Higher inlet fluid velocities are also shown to be more impactful in reducing the particle count for larger diameter particles. That indicates that the inertia of the particles plays a critical role in their filtration efficiency with this design. Particle plots for each geometry and flow velocity can be found in Appendix A.65-69.

The hydrodynamics over the pore of the structure are most critical to the filtration efficiency as shown by the sensitivity to filtrate outlet pressure and fluid velocity. To that end, visualization of the filter pore for C19 was done to elucidate the vortical and shear dynamics occurring. To visualize the vortex forming over the pore, the z -vorticity was analyzed at the midplane of C19 for multiple different filtrate outlet pressures (Figure 4.6).

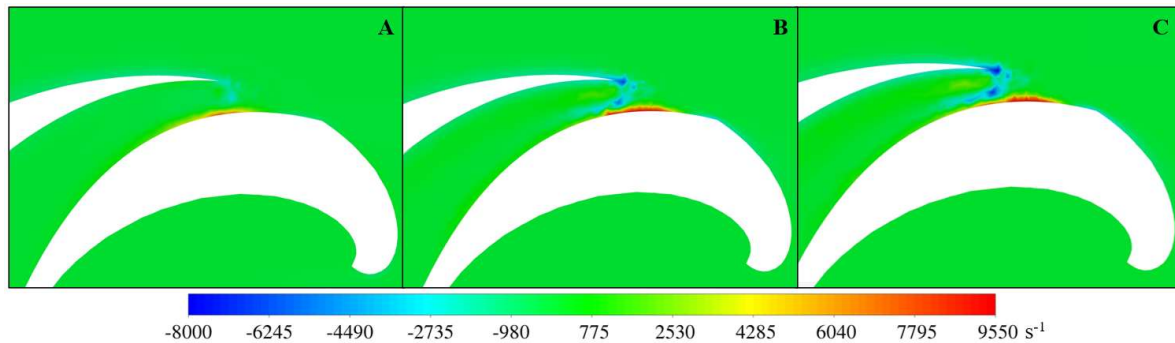


Figure 4.6. z -Vorticity of C19 Midplane at 0.2 m/s Inlet Velocity. (A) 500 Pa filtrate outlet pressure. (B) 5 kPa filtrate outlet pressure. (C) 10 kPa filtrate outlet pressure.

As expected, and shown in Figure 4.6, the vortex over the mouth increases in size and strength as the filtrate outlet pressure is increased. When this information is coupled with the particle diameter trend shown in Figure 4.5, it supports a theory for a combination of vortical

crossflow [16] and ricochet filtration [18] as methods for particle exclusion with this structure. More information about the system and its' particle filtration modality becomes evident when visualizing the wall shear stress for C19 at the same conditions from Figure 4.6B (Figure 4.7).

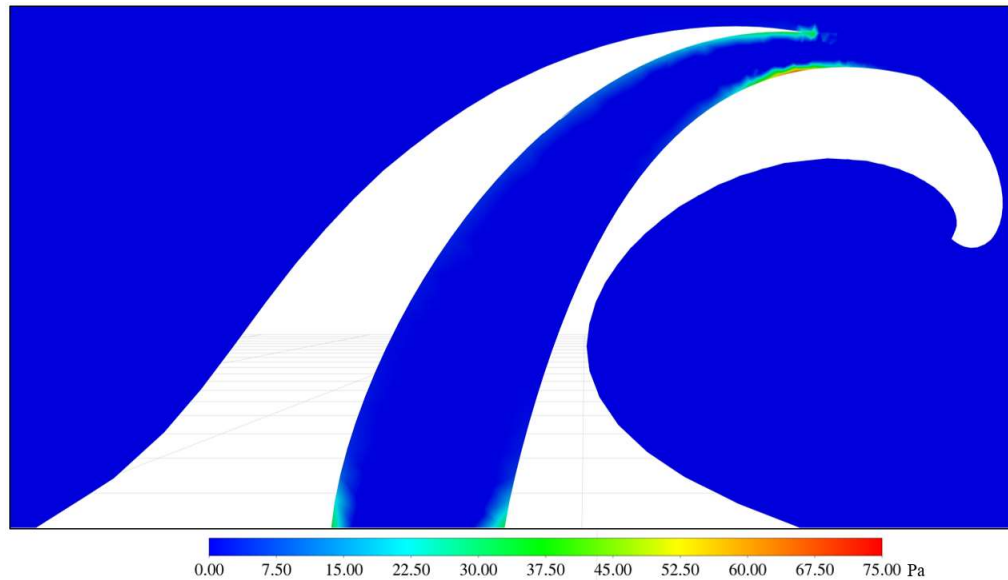


Figure 4.7. Wall Shear Stress of C19 Midplane at 0.2 m/s Inlet Velocity and 5 kPa Outlet Pressure.

As opposed to the results from Figure 4.6, Figure 4.7 does not appear to support a modality of shear-modulated particle migration [12] as the high shear region of the flow is far too low within the pore to have particles potentially escape and reenter the bulk flow. These results appear to indicate that the vortical crossflow and ricochet mechanisms for filtration are more prevalent here than any type of shear-induced particle migration effect.

Now that the simulations have been run and the results collated, the optimum case can undergo EFD to evaluate the accuracy of said simulation. To begin, the model was 3D printed and mounted into the tunnel as shown in Figure 4.3. The resultant velocity field was then collected at inlet velocities of 0.2, 0.3, and 0.4 m/s using PIV and then said velocity field was compared to the same plane in the CFD simulations to evaluate the error of the CFD. As the outlet pressure being applied to the pore during the EFD experiment was not known, the velocity fields were compared against results from the CFD with different outlet pressures

from 1 to 10 kPa. Starting with 0.2 m/s the resulting velocity fields for the EFD and CFD can be seen in Figure 4.8.

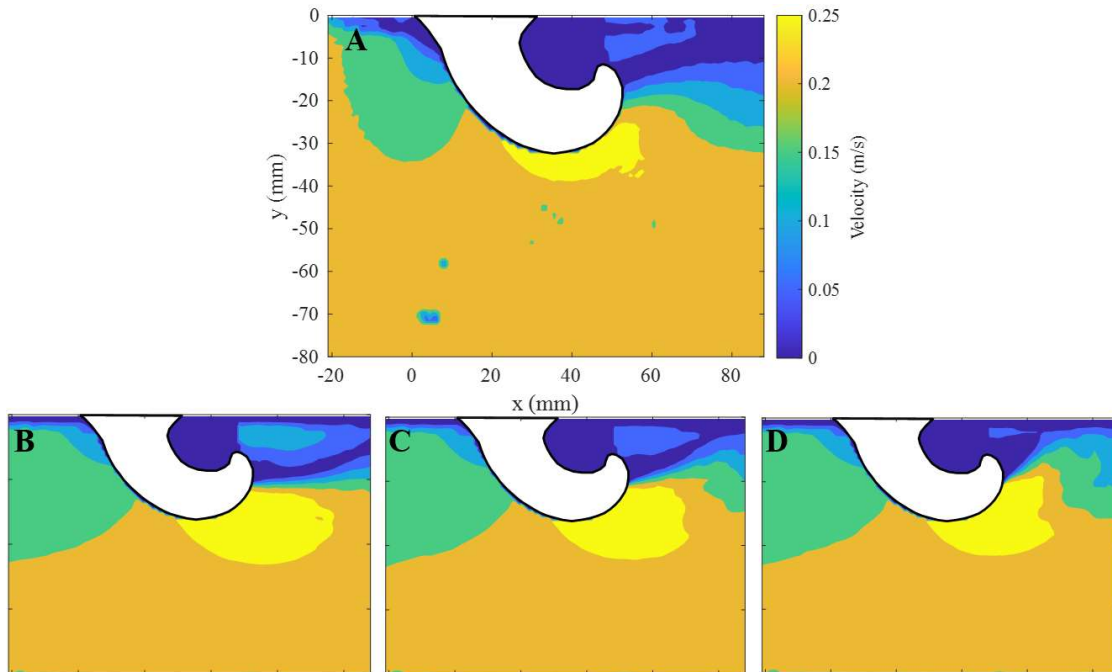


Figure 4.8. Flow Velocity Field in xy -plane with Inlet Velocity of 0.2 m/s for (A) EFD, (B) CFD with 1 kPa of pressure, (C) CFD with 5 kPa of pressure, and (D) CFD with 10 kPa of pressure.

Several results become abundantly clear when analyzing these velocity fields. The CFD in all cases (Figure 4.8B-D) tends to overestimate the extent of the leading edge on the model while higher values for the outlet pressure (Figure 4.8C-D) tend to have a smaller recirculating region downstream of the geometry. Some portions in the lower left hand of the EFD also show no fluid movement, but that is attributed to error in the PIV collection causing dead pixels for image analysis. Also, the portion of the field in the upper middle was obscured to PIV from the crest of the wave and thus no signal was computed for the EFD in that area. This error was subsequently matched for and corrected in the CFD to ensure proper error analysis.

In order to compare the fields to one another, the root mean square error (RMSE) was computed at each node in the velocity field. The total RMSE for all N points in the velocity field is denoted by

$$RMSE = \left(\frac{1}{N} \sum_{i=1}^N (x_i - \hat{x}_i)^2 \right)^{\frac{1}{2}} \quad (15)$$

where x_i and \hat{x}_i are the EFD and CFD values respectively. Plotting the RMSE at each node value (Figure 4.9) allows for the analysis of the local CFD error to find specific regions of low- or high-quality estimation.

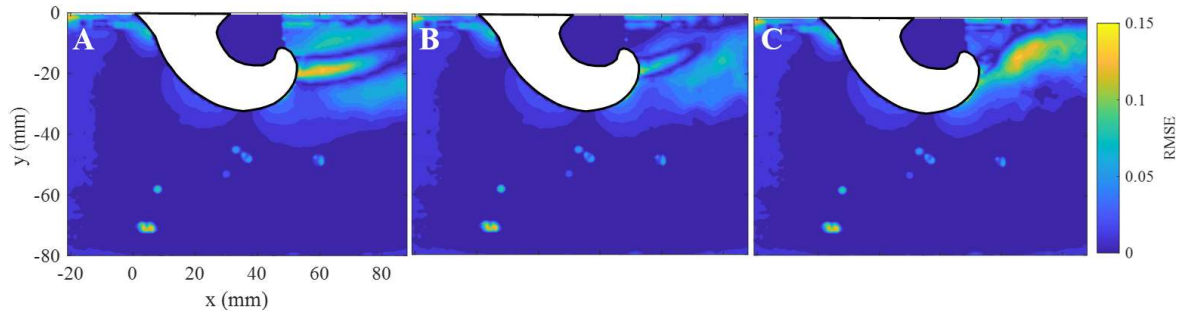


Figure 4.9. RMSE of Flow Velocity Field in xy -plane with Inlet Velocity of 0.2 m/s for (A) CFD with 1 kPa of pressure, (B) CFD with 5 kPa of pressure, and (C) CFD with 10 kPa of pressure.

The plots from Figure 4.9 more clearly illustrate the regions of error which were identified during the visual comparison in Figure 4.8. The bulk flow region has very little to no error except for areas where the PIV erroneously generated dead pixels. The leading edge and downstream region proceeding the geometry have higher error which is to be expected as these regions have both higher order turbulence interactions as well as a large disparity between the velocity of fluid due to recirculation regions. Another observation to be made is that the pressure which produced the lowest overall error is that with 5 kPa at the outlet, most likely this is because the true value is closer to this value than 1 or 10 kPa. However, that is expected to change as the inlet velocity is increased due to the Venturi effect of fluid flowing over the pore which will cause a pressure to be exerted against the one applied at the outlet which does not change between trials.

The next EFD was done with a fluid inlet velocity of 0.3 m/s with the resulting velocity fields for the EFD and CFD in Figure 4.10.

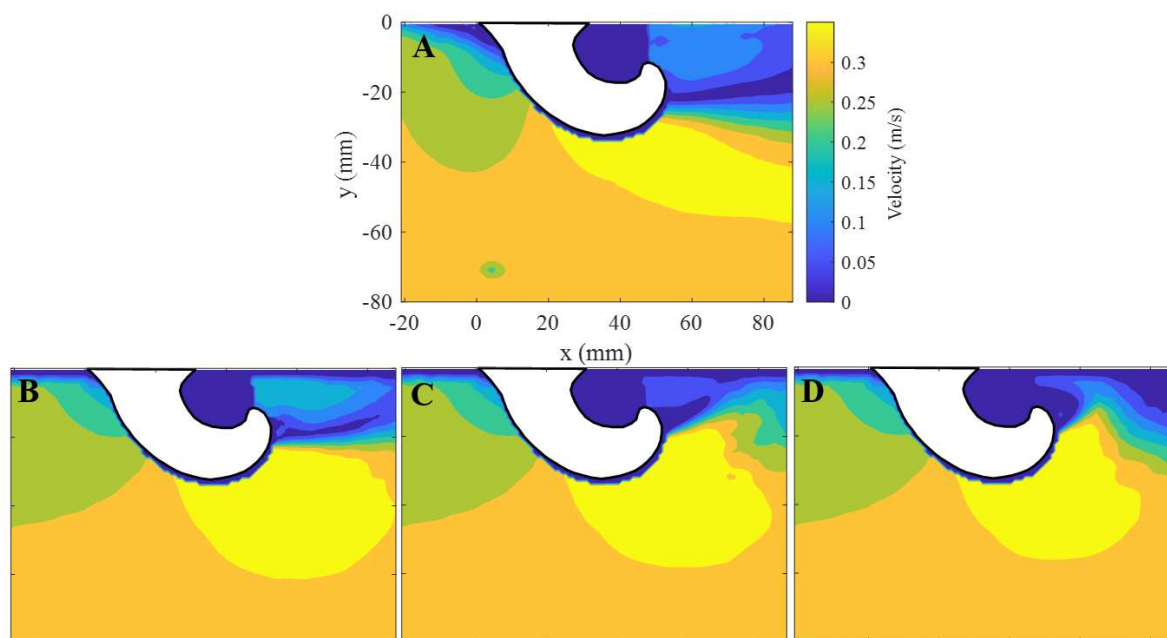


Figure 4.10. Flow Velocity Field in xy -plane with Inlet Velocity of 0.3 m/s for (A) EFD, (B) CFD with 1 kPa of pressure, (C) CFD with 5 kPa of pressure, and (D) CFD with 10 kPa of pressure.

As seen previously, the CFD for each pressure value (Figure 4.10B-D) overestimates the extent of the leading edge on the model. Here the CFD conducted at the lowest pressure (Figure 4.10B) appears to best model the recirculating region as well as displays the largest high velocity region near and around the pore. The dead pixel region from the PIV can still be seen from the EFD field and will need to be considered in the error as before. To evaluate these observations more succinctly the RMSE is plotted (Figure 4.11) as done previously.

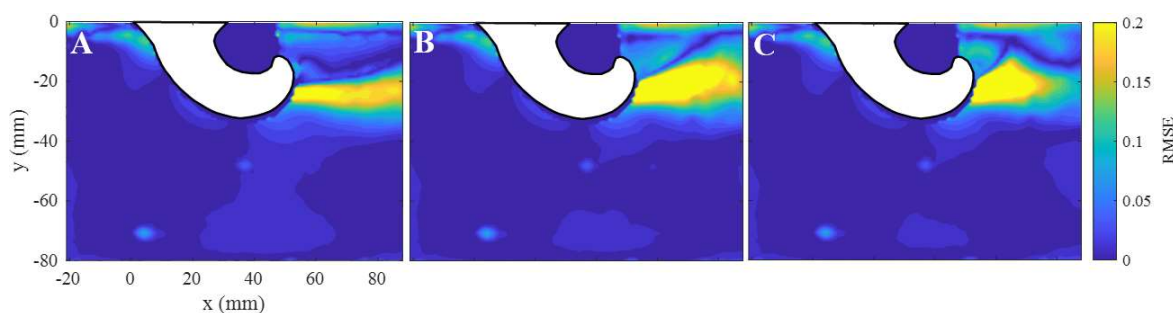


Figure 4.11. RMSE of Flow Velocity Field in xy -plane with Inlet Velocity of 0.3 m/s for (A) CFD with 1 kPa of pressure, (B) CFD with 5 kPa of pressure, and (C) CFD with 10 kPa of pressure.

As expected, the bulk flow region again has very little to no error except for the dead pixel regions while the leading and downstream flows have the highest errors. Along with these observations is the confirmation of the previous idea which anticipated the lowest error CFD estimation to be the case of lower outlet pressure as the inlet velocity increased due to the rivaling Venturi effect. The final trial for the EFD was done for an inlet velocity of 0.4 m/s and the field shown in Figure 4.12.

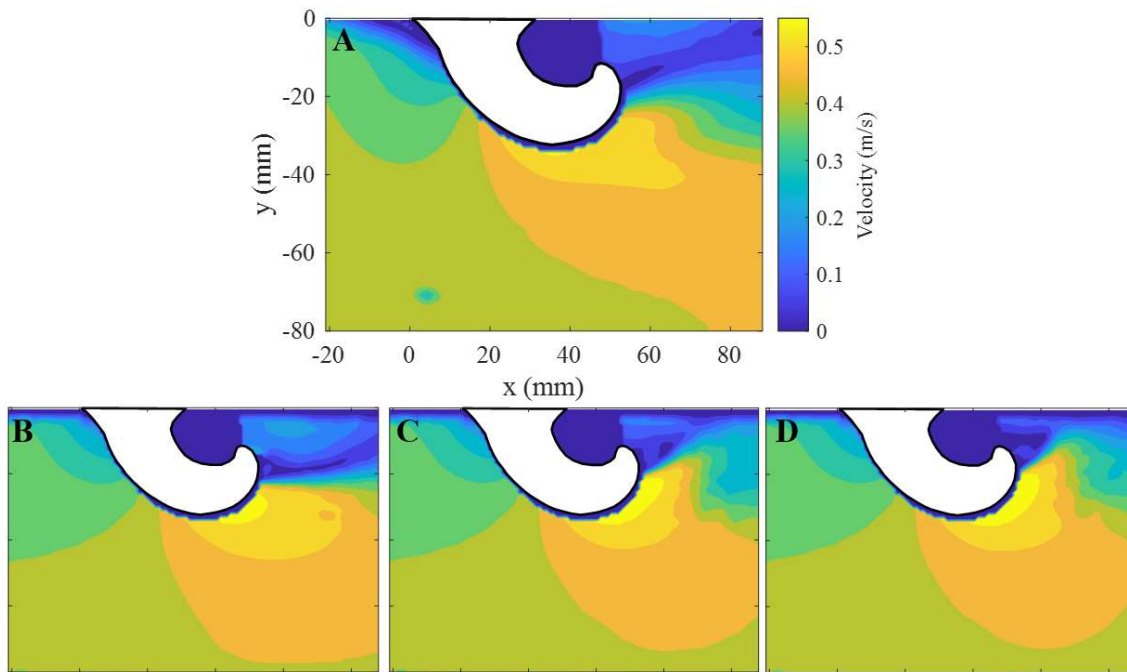


Figure 4.12. Flow Velocity Field in xy -plane with Inlet Velocity of 0.4 m/s for (A) EFD, (B) CFD with 1 kPa of pressure, (C) CFD with 5 kPa of pressure, and (D) CFD with 10 kPa of pressure.

Following the trend up until this point, each CFD case (Figure 4.12B-D) overestimates the extent of the leading edge on the model, but the downstream region for the higher outlet pressures appears to be increasingly erroneous. Plotting the RMSE as done previously (Figure 4.13) results in the following.

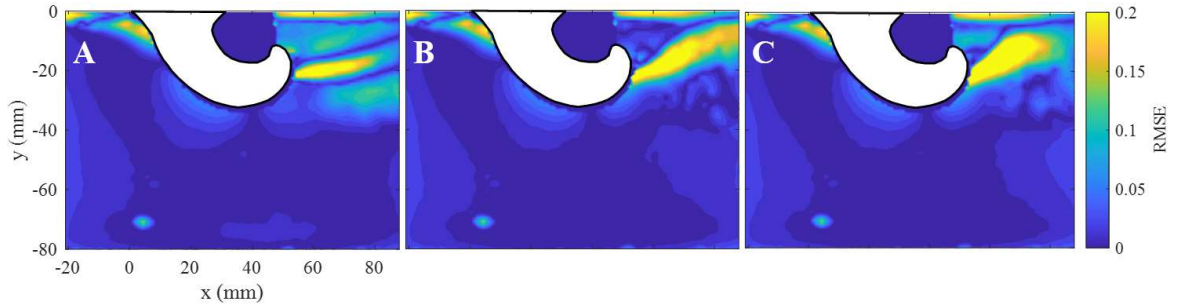


Figure 4.13. RMSE of Flow Velocity Field in xy -plane with Inlet Velocity of 0.4 m/s for (A) CFD with 1 kPa of pressure, (B) CFD with 5 kPa of pressure, and (C) CFD with 10 kPa of pressure.

Which merely has the trend continuing as each EFD has done before as well as repeating the pattern shown by the lower outlet pressure CFD cases. To better quantify the RMSE, the average over all nodes of each RMSE field is calculated resulting in Table 4.1 below.

Table 4.1. Average RMSE Value for each CFD Validation.

RMSE (m/s)		Inlet Velocity (m/s)		
		0.2	0.3	0.4
Outlet Pressure (kPa)	1	0.0124	0.0188	0.021
	5	0.0106	0.0241	0.0204
	10	0.0117	0.0211	0.0231

The average RMSE values do well to implicate the observed trends from the velocity fields as well as reinforce intuition. As the inlet fluid velocity is increased the RMSE of the lower outlet pressure cases tends to become more accurate in comparison to the higher outlet pressure cases.

The work presented herein has outlined and tested a framework for future investigations into other parametrized biomimetic minimal surfaces. To that end, the parameterization and subsequent optimization of the WMS was shown to be both effective as well as produced an accurate estimation of the true flow field. Further testing of this framework would best be extended to array-based optimization of the full 3D filter structure similar to the work in Chapter 3 but utilizing the optimized WMS from Chapter 4. Further

work could be also done in refinement of the CFD simulation itself to reduce the overall RMSE for more complex flow geometries. As shown from previous results, the best way to begin further tuning the simulation would be to investigate higher order modeling near the walls and edges of the computational domain as those regions displayed large inaccuracies in comparison to many of the transitional and bulk flow regions.

REFERENCES

1. Princiotta, F.T. and D.H. Loughlin, *Global climate change: the quantifiable sustainability challenge*. J Air Waste Manag Assoc, 2014. **64**(9): p. 979-94.
2. von Stechow, C., et al., *Integrating Global Climate Change Mitigation Goals with Other Sustainability Objectives: A Synthesis*. Annual Review of Environment and Resources, 2015. **40**(1): p. 363-394.
3. Board, O.S., E. National Academies of Sciences, and Medicine, *Environmental engineering for the 21st century: Addressing grand challenges*. 2019: National Academies Press.
4. Arkin, A., et al., *Grand challenges for biological and environmental research: A long-term vision*. 2010.
5. Ulrich, A. and E. Schnug, *The Modern Phosphorus Sustainability Movement: A Profiling Experiment*. Sustainability, 2013. **5**(11): p. 4523-4545.
6. Smith, C., A.K. Hill, and L. Torrente-Murciano, *Current and future role of Haber–Bosch ammonia in a carbon-free energy landscape*. Energy & Environmental Science, 2020. **13**(2): p. 331-344.
7. Portielje, R. and D.T. Van der Molen, *Relationships between eutrophication variables: from nutrient loading to transparency*, in *Shallow Lakes '98: Trophic Interactions in Shallow Freshwater and Brackish Waterbodies*, N. Walz and B. Nixdorf, Editors. 1999, Springer Netherlands: Dordrecht. p. 375-387.
8. Pinckney, J.L., et al., *The role of nutrient loading and eutrophication in estuarine ecology*. Environmental health perspectives, 2001. **109**(suppl 5): p. 699-706.
9. Moller, G., et al., *Reactive filtration*. 2008, Google Patents.
10. Adin, A. and M. Elimelech, *Particle filtration for wastewater irrigation*. Journal of irrigation and drainage engineering, 1989. **115**(3): p. 474-487.
11. Bhagat, A.A.S., S.S. Kuntaegowdanahalli, and I. Papautsky, *Inertial microfluidics for continuous particle filtration and extraction*. Microfluidics and nanofluidics, 2009. **7**(2): p. 217-226.
12. Bhagat, A.A.S., S.S. Kuntaegowdanahalli, and I. Papautsky, *Enhanced particle filtration in straight microchannels using shear-modulated inertial migration*. Physics of Fluids, 2008. **20**(10): p. 101702.
13. Fisk, W.J. and W.R. Chan, *Effectiveness and cost of reducing particle-related mortality with particle filtration*. Indoor air, 2017. **27**(5): p. 909-920.
14. Rushton, A., A.S. Ward, and R.G. Holdich, *Solid-liquid filtration and separation technology*. 2008: John Wiley & Sons.
15. Wakeman, R., *The influence of particle properties on filtration*. Separation and Purification Technology, 2007. **58**(2): p. 234-241.
16. Brooks, H., et al., *Physical modeling of vortical cross-step flow in the American paddlefish, *Polyodon spathula**. Plos one, 2018. **13**(3): p. e0193874.
17. Cheer, A., et al., *Computational fluid dynamics of fish gill rakers during crossflow filtration*. Bulletin of mathematical biology, 2012. **74**(4): p. 981-1000.
18. Divi, R.V., J.A. Strother, and E.M. Paig-Tran, *Manta rays feed using ricochet separation, a novel nonclogging filtration mechanism*. Science advances, 2018. **4**(9): p. eaat9533.

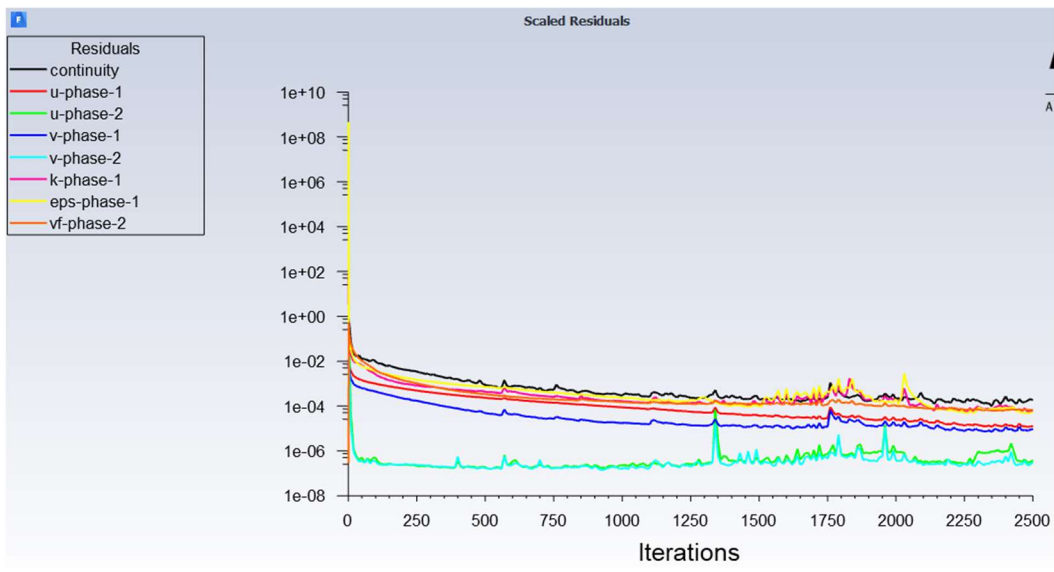
19. Paig-Tran, E.W., T. Kleinteich, and A.P. Summers, *The filter pads and filtration mechanisms of the devil rays: Variation at macro and microscopic scales*. J Morphol, 2013. **274**(9): p. 1026-43.
20. Sanderson, S.L., et al., *Fish mouths as engineering structures for vortical cross-step filtration*. Nature communications, 2016. **7**(1): p. 1-9.
21. Clarke, D.A., et al., *Investigation of flow through triply periodic minimal surface-structured porous media using MRI and CFD*. Chemical Engineering Science, 2021. **231**: p. 116264.
22. Fu, Y., et al., *CFD Study of Countercurrent Flow in Triply Periodic Minimal Surfaces with CO₂BOL Solvent*. 2019, Pacific Northwest National Lab.(PNNL), Richland, WA (United States).
23. Zhu, Z., et al., *Biomimetic dynamic membrane (BDM): Fabrication method and roles of carriers and laccase*. Chemosphere, 2020. **240**: p. 124882.
24. Beratto-Ramos, A., et al., *Fabrication and Filtration Performance of Aquaporin Biomimetic Membranes for Water Treatment*. Separation & Purification Reviews, 2021: p. 1-18.
25. Liao, R., et al., *Biomimetic Mineralization to Fabricate Superhydrophilic and Underwater Superoleophobic Filter Mesh for Oil–Water Separations*. Industrial & Engineering Chemistry Research, 2020. **59**(13): p. 6226-6235.
26. Aires-Barros, M.R. and A.M. Azevedo, *Fundamentals of Biological Separation Processes*, in *Current Developments in Biotechnology and Bioengineering*. 2017. p. 187-237.
27. Wright, R.T., et al., *Field and laboratory measurements of bivalve filtration of natural marine bacterioplankton I*. Limnology and oceanography, 1982. **27**(1): p. 91-98.
28. Goldbogen, J.A., et al., *How Baleen Whales Feed: The Biomechanics of Engulfment and Filtration*. Ann Rev Mar Sci, 2017. **9**: p. 367-386.
29. Werth, A.J., *Flow-dependent porosity and other biomechanical properties of mysticete baleen*. J Exp Biol, 2013. **216**(Pt 7): p. 1152-9.
30. Werth, A.J. and J. Potvin, *Baleen hydrodynamics and morphology of cross-flow filtration in balaenid whale suspension feeding*. PLoS One, 2016. **11**(2): p. e0150106.
31. Zhu, Y., et al., *Oral cavity flow distribution and pressure drop in balaenid whales feeding: a theoretical analysis*. Bioinspir Biomim, 2020. **15**(3): p. 036004.
32. Marshall, A. and S. Lozeva, *Questioning the theory and practice of biomimicry*. International Journal of Design & Nature and Ecodynamics, 2009. **4**(1): p. 1-10.
33. Finn, R., *On equations of minimal surface type*. Annals of Mathematics, 1954: p. 397-416.
34. Barbosa, J.L. and M.d. Carmo, *On the size of a stable minimal surface in R³*. American Journal of Mathematics, 1976: p. 515-528.
35. Vrolijk, N., et al., *Surface characterisation of two gorgonian coral species: implications for a natural antifouling defence*. Biofouling, 1990. **2**(1): p. 39-54.
36. Stievenart, J.-L., et al., *Minimal surface: A useful paradigm to describe the deeper part of the corpus callosum?* Brain research bulletin, 1997. **44**(2): p. 117-124.
37. Mondaini, R. *The minimal surface structure of biomolecules*. in *Proceedings of the First Brazilian Symposium on Mathematical and Computational Biology, ed E-papers Ltda*. 2001.
38. Colonna, J.-F., *Un coquillage (surface de Jeener 1) en mouvement*. 1994.

39. Jeener, P., *My Mathematical Engravings*, in *Mathematics and Modern Art*. 2012, Springer. p. 85-104.
40. Panaras, A.G. and F.K. Lu, *Micro-vortex generators for shock wave/boundary layer interactions*. *Progress in Aerospace Sciences*, 2015. **74**: p. 16-47.
41. Choi, D.-C., et al., *Effect of Pattern shape on the initial deposition of particles in the aqueous phase on patterned membranes during crossflow filtration*. *Environmental Science & Technology Letters*, 2017. **4**(2): p. 66-70.
42. Lyu, Z., et al., *3D-printed surface-patterned ceramic membrane with enhanced performance in crossflow filtration*. *Journal of Membrane Science*, 2020. **606**: p. 118138.
43. Bandyopadhyay, P.R. and A.M. Hellum, *Modeling how shark and dolphin skin patterns control transitional wall-turbulence vorticity patterns using spatiotemporal phase reset mechanisms*. *Scientific reports*, 2014. **4**(1): p. 1-10.
44. Bubolz, M., et al., *The use of dean vortices for crossflow microfiltration: basic principles and further investigation*. *Separation and Purification Technology*, 2002. **26**(1): p. 81-89.
45. Chen, J., et al., *The influence of micro vortex generator on inception cavitation*. *Physics of Fluids*, 2021. **33**(10): p. 103312.
46. Heffron, A.P., J.J. Williams, and E.J. Avital, *Large Eddy Simulation of Microvortex Generators in a Turbulent Boundary Layer*. *Journal of Fluids Engineering*, 2021. **143**(5).
47. Jeong, J. and F. Hussain, *On the identification of a vortex*. *Journal of fluid mechanics*, 1995. **285**: p. 69-94.
48. Kamalakshakurup, G., et al., *Shear-dependent microvortices in liquid-liquid flow-focusing geometry: A theoretical, numerical, and experimental study*. *Physics of Fluids*, 2021. **33**(3): p. 032016.
49. Lin, J., F. Howard, and G. Selby, *Small submerged vortex generators for turbulent flow separation control*. *Journal of Spacecraft and Rockets*, 1990. **27**(5): p. 503-507.
50. Lin, J.C., *Review of research on low-profile vortex generators to control boundary-layer separation*. *Progress in aerospace sciences*, 2002. **38**(4-5): p. 389-420.
51. Fluent, A., *Ansys fluent*. Academic Research. Release, 2015. **14**.
52. Greifzu, F., et al., *Assessment of particle-tracking models for dispersed particle-laden flows implemented in OpenFOAM and ANSYS FLUENT*. *Engineering Applications of Computational Fluid Mechanics*, 2015. **10**(1): p. 30-43.
53. Hinze, J., *Turbulence*. McGraw-Hill Publishing Co. New York, 1975.
54. Rutten, D. and R. McNeel, *Grasshopper3D*. Robert McNeel & Associates: Seattle, WA, USA, 2007.
55. McNeel, R., *Rhinoceros*. NURBS modeling for Windows: <http://www.rhino3d.com/jewelry.htm>, 2015.
56. Cokljat, D., et al., *Reynolds-stress model for Eulerian multiphase*. *Progress in Computational Fluid Dynamics, An International Journal*, 2006. **6**(1-3): p. 168-178.
57. Kieckhefen, P., et al., *Possibilities and Limits of Computational Fluid Dynamics-Discrete Element Method Simulations in Process Engineering: A Review of Recent Advancements and Future Trends*. *Annu Rev Chem Biomol Eng*, 2020. **11**: p. 397-422.

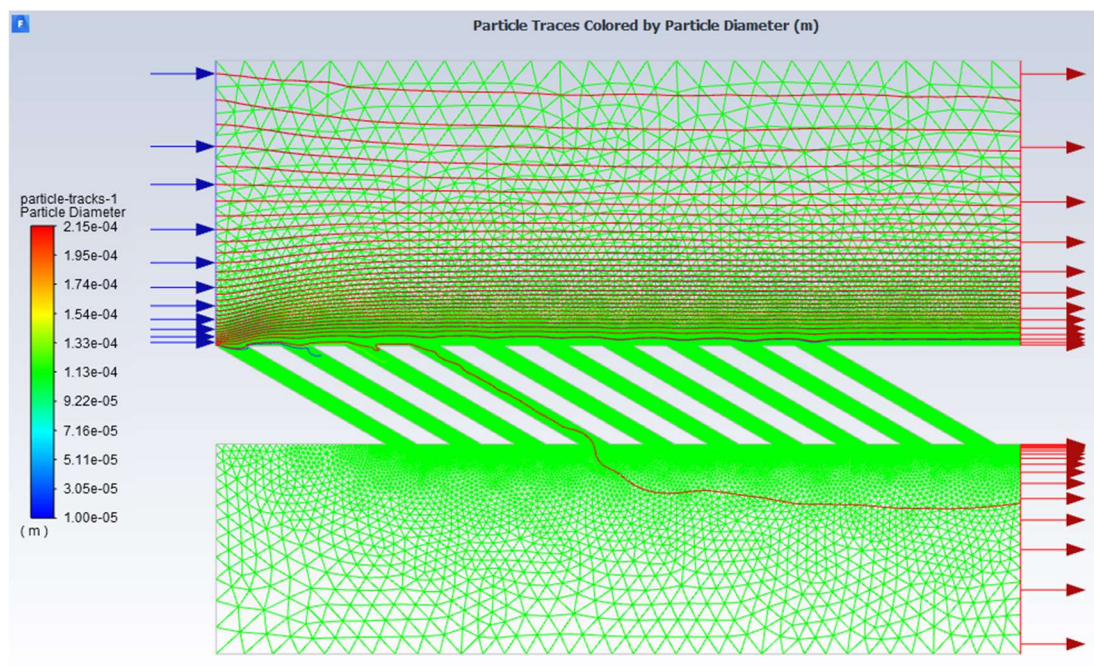
58. Magnussen, B.F. *The eddy dissipation concept: A bridge between science and technology.* in *ECCOMAS thematic conference on computational combustion*. 2005. Libson, Portugal.
59. Chong, M.S., A.E. Perry, and B.J. Cantwell, *A general classification of three-dimensional flow fields.* *Physics of Fluids A: Fluid Dynamics*, 1990. **2**(5): p. 765-777.
60. Melander, M.V. and F. Hussain, *Coupling between a coherent structure and fine-scale turbulence.* *Physical Review E*, 1993. **48**(4): p. 2669.
61. Epps, B. *Review of vortex identification methods.* in *55th AIAA aerospace sciences meeting*. 2017.
62. Gao, Y. and C. Liu, *Rortex and comparison with eigenvalue-based vortex identification criteria.* *Physics of Fluids*, 2018. **30**(8): p. 085107.
63. Zhang, Y.-n., et al., *A selected review of vortex identification methods with applications.* *Journal of Hydrodynamics*, 2018. **30**(5): p. 767-779.
64. Fabrigar, L.R. and D.T. Wegener, *Exploratory factor analysis*. 2011: Oxford University Press.
65. Bartlett, M.S., *Tests of significance in factor analysis.* *British journal of psychology*, 1950.
66. Dziuban, C.D. and E.C. Shirkey, *When is a correlation matrix appropriate for factor analysis? Some decision rules.* *Psychological bulletin*, 1974. **81**(6): p. 358.
67. Kaiser, H.F., *A second generation little jiffy.* 1970.
68. Howard, M.C., *A review of exploratory factor analysis decisions and overview of current practices: What we are doing and how can we improve?* *International Journal of Human-Computer Interaction*, 2016. **32**(1): p. 51-62.
69. Adrian, R.J. and J. Westerweel, *Particle image velocimetry*. 2011: Cambridge university press.
70. Willert, C.E. and M. Gharib, *Digital particle image velocimetry.* *Experiments in fluids*, 1991. **10**(4): p. 181-193.

APPENDIX A

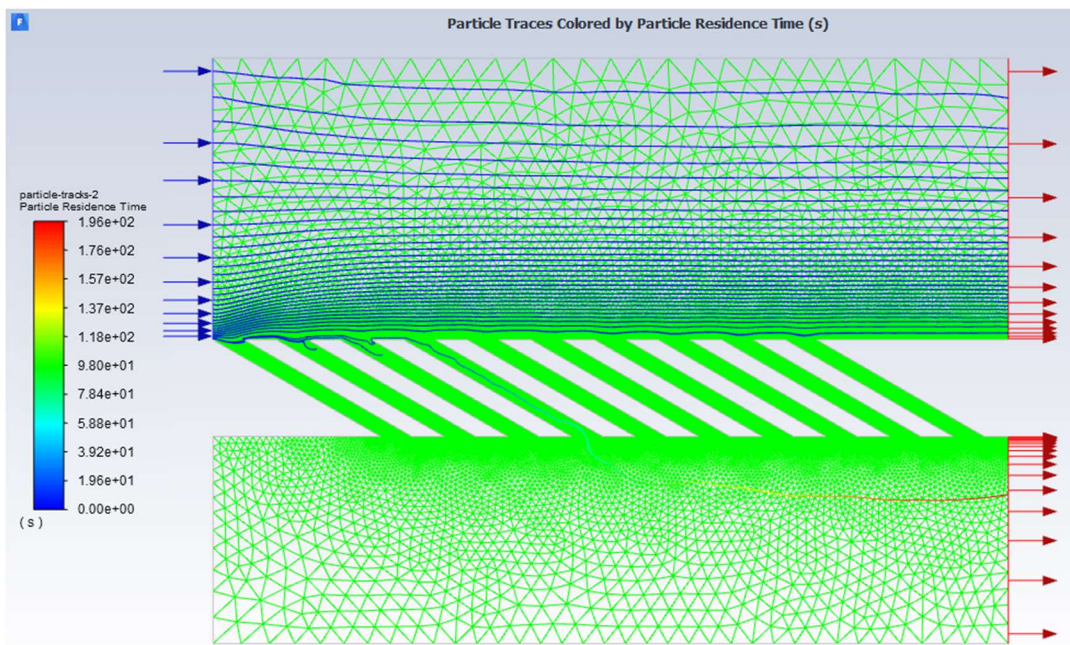
A.1. Left-Oriented 30° Angle with O₂ Phase Residuals



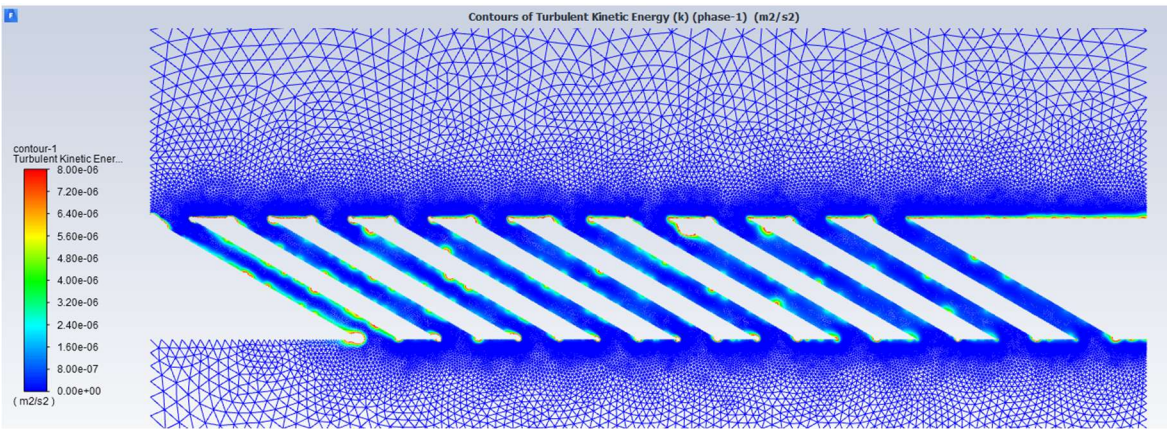
A.2. Left-Oriented 30° Angle with O₂ Phase Particle Tracks by Diameter



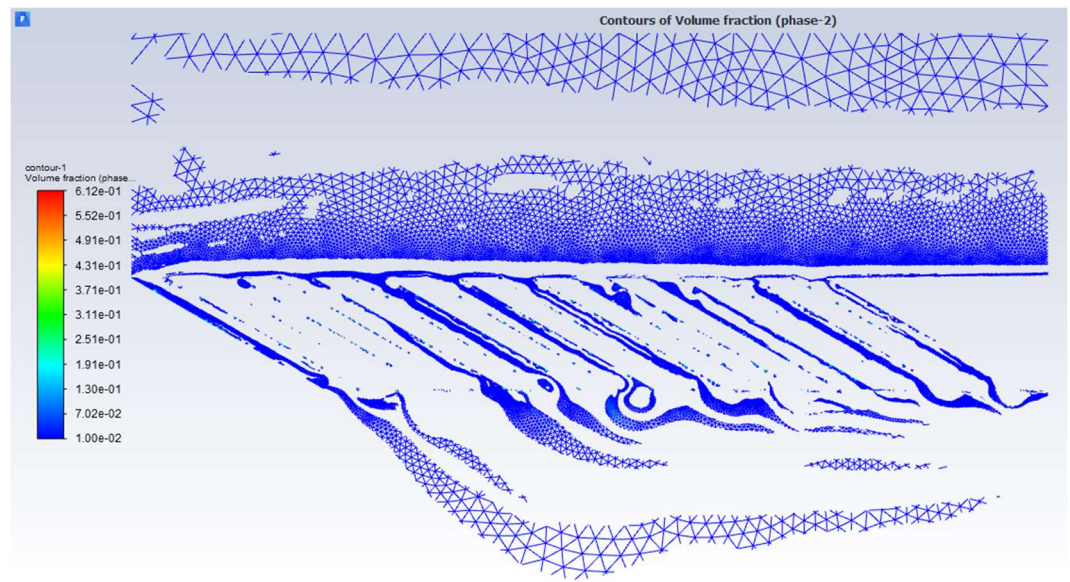
A.3. Left-Oriented 30° Angle with O₂ Phase Particle Tracks by Residence Time



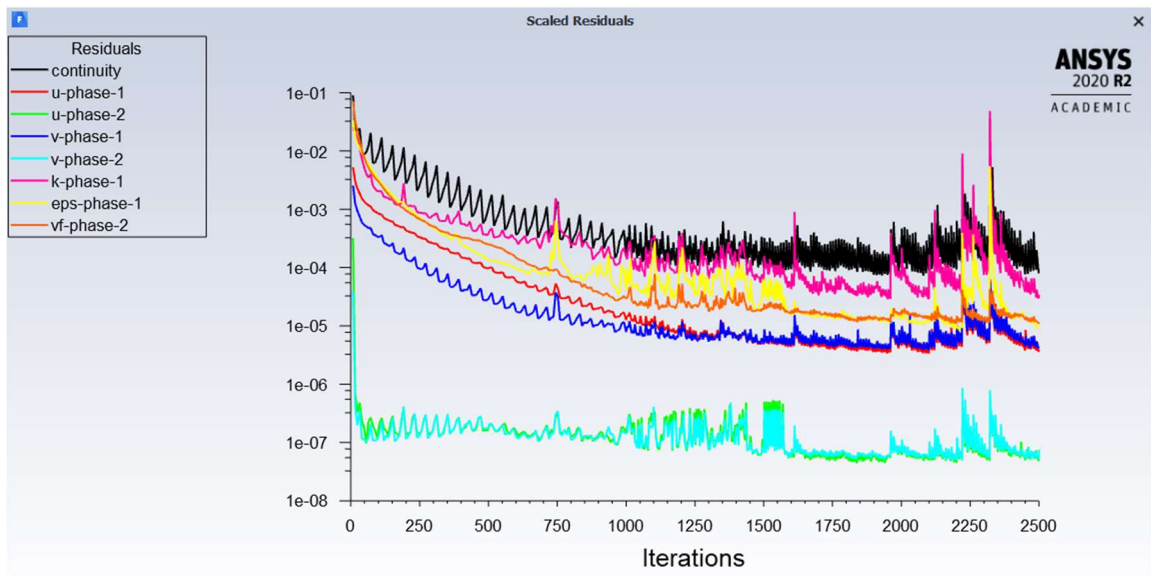
A.4. Left-Oriented 30° Angle with O₂ Phase Turbulent Kinetic Energy (Phase 1)

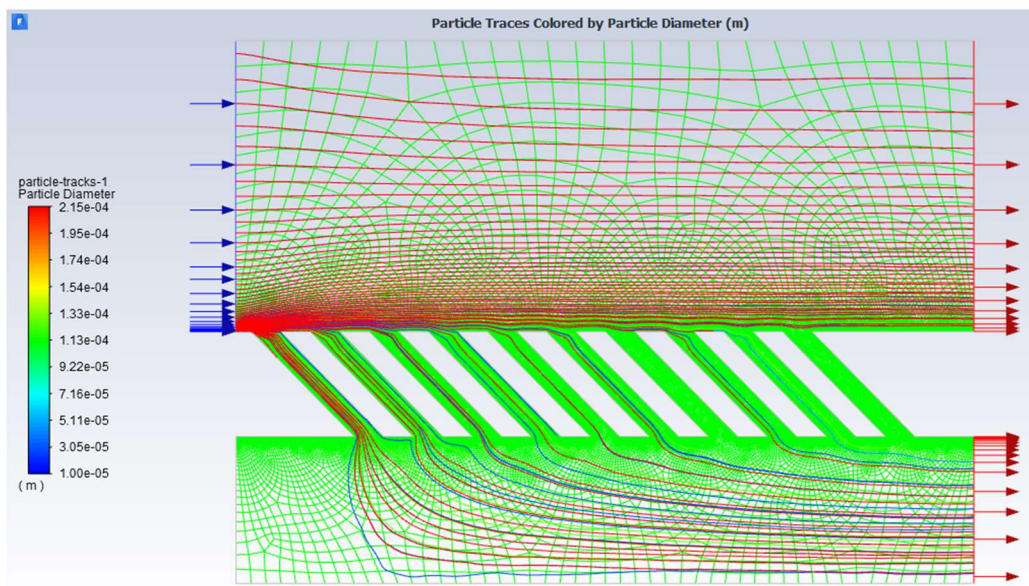
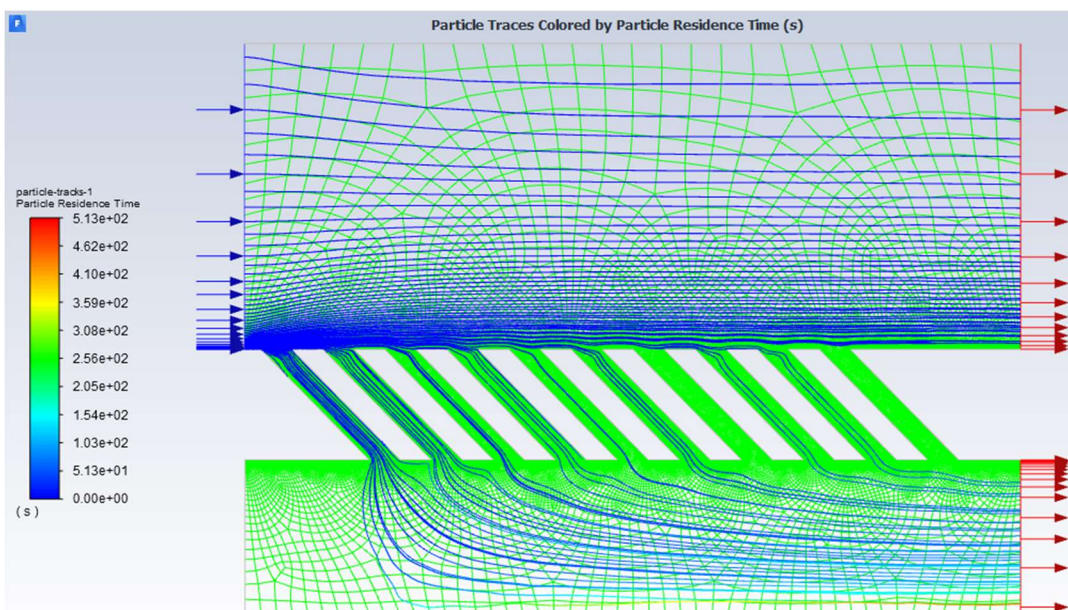


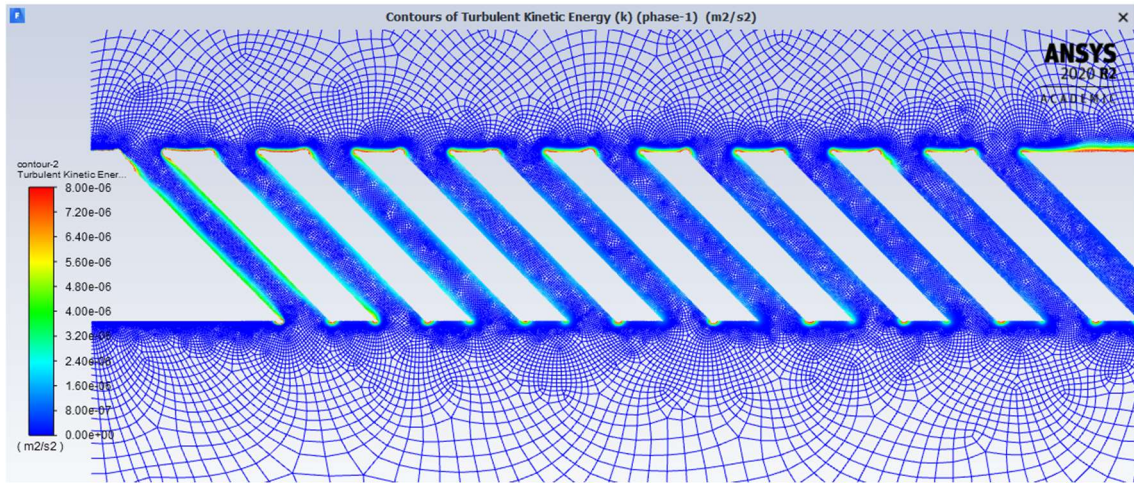
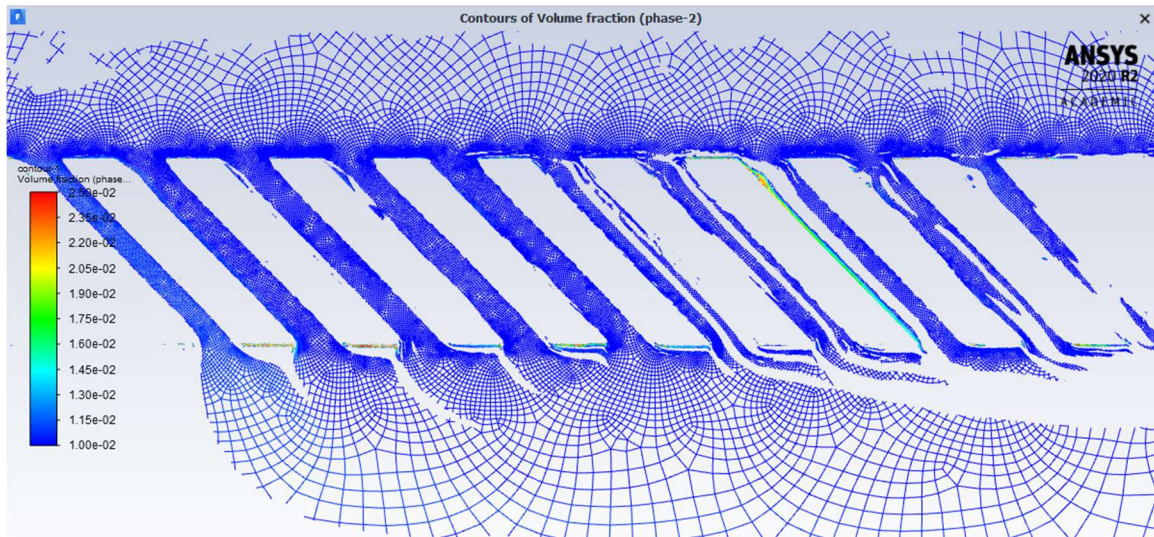
A.5 Left-Oriented 30° Angle with O₂ Phase Volume Fraction (Phase 2)

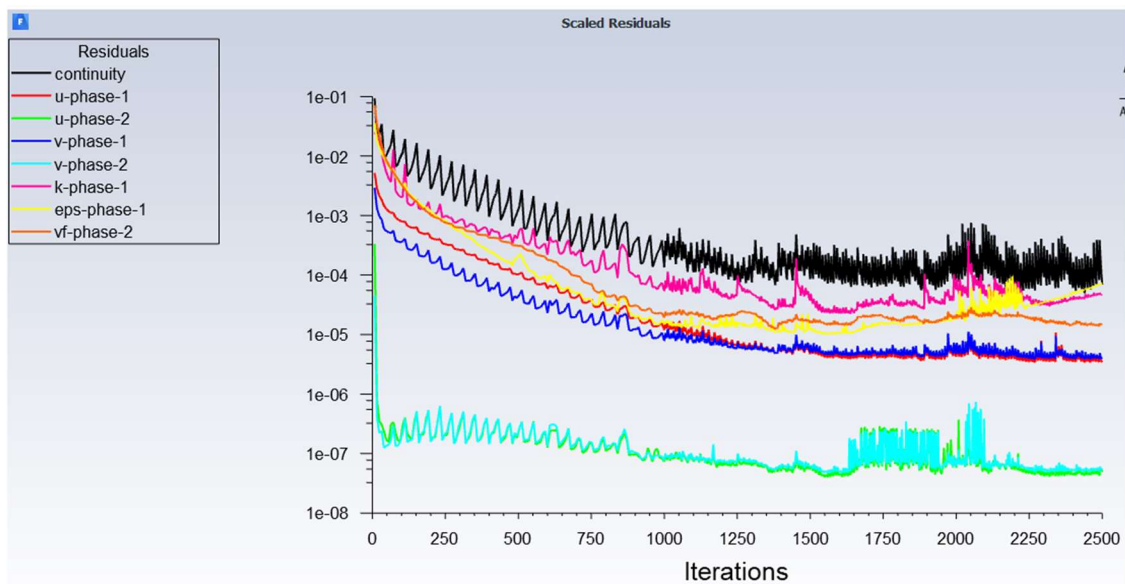
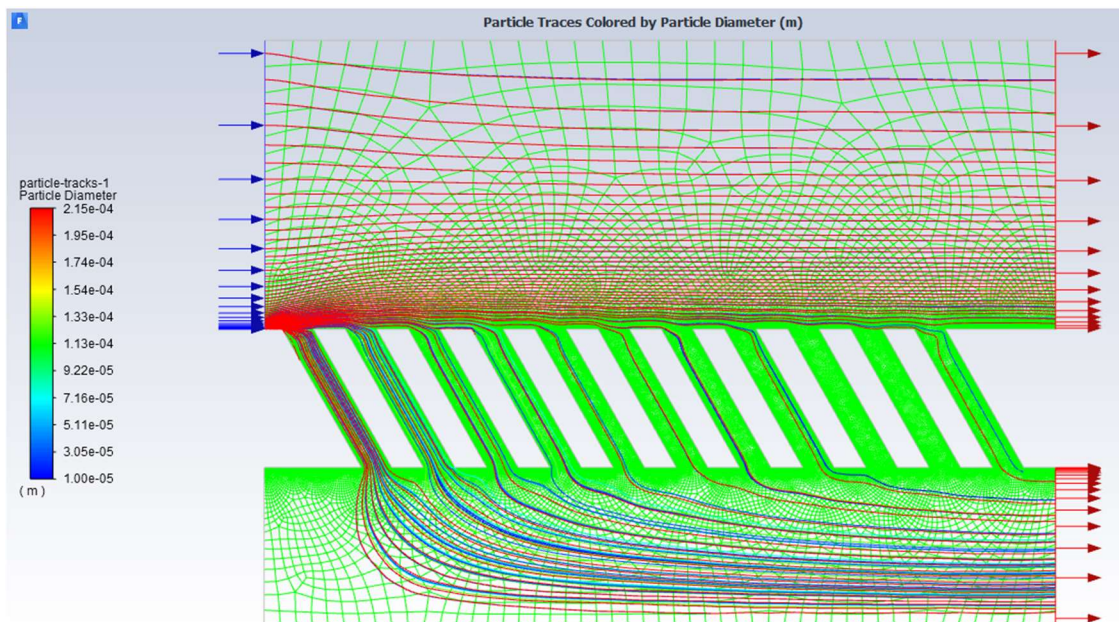


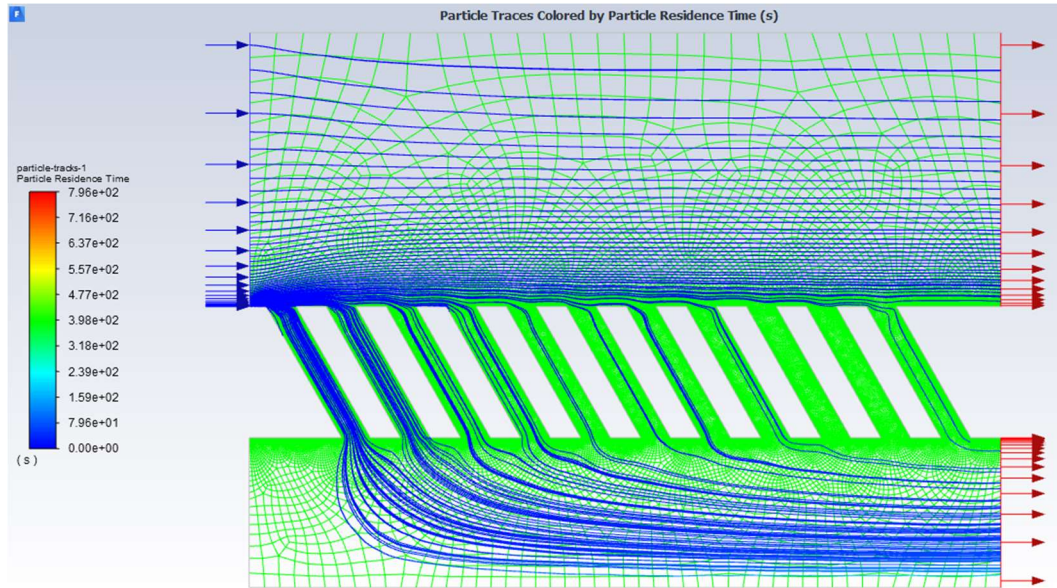
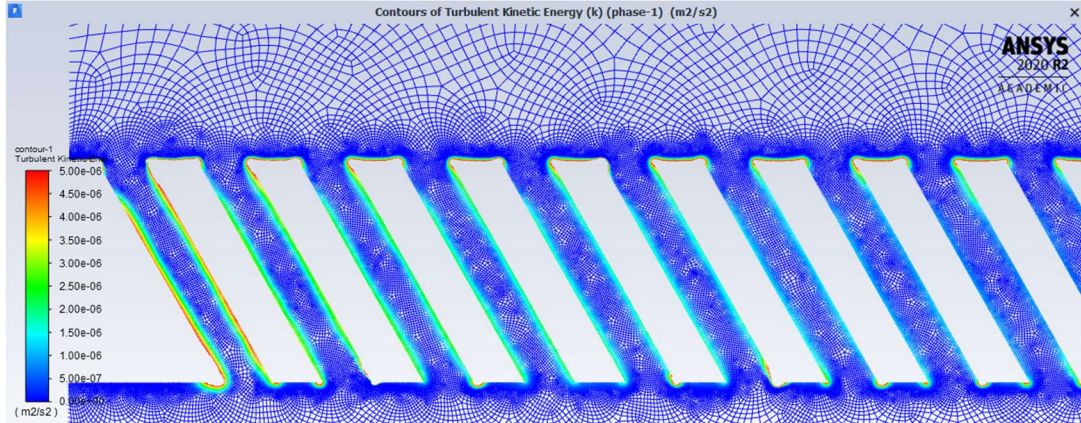
A.6 Left-Oriented 45° Angle with O₂ Phase Residuals

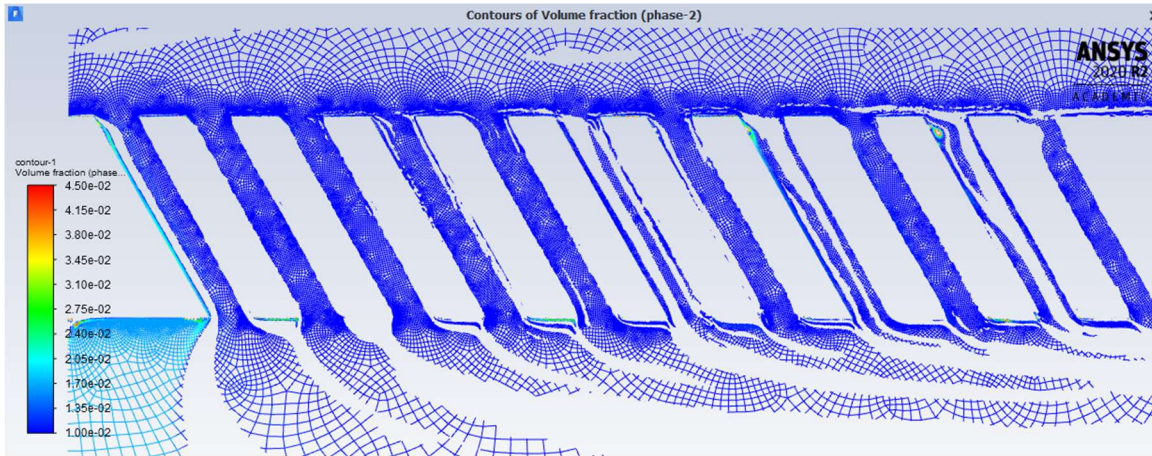
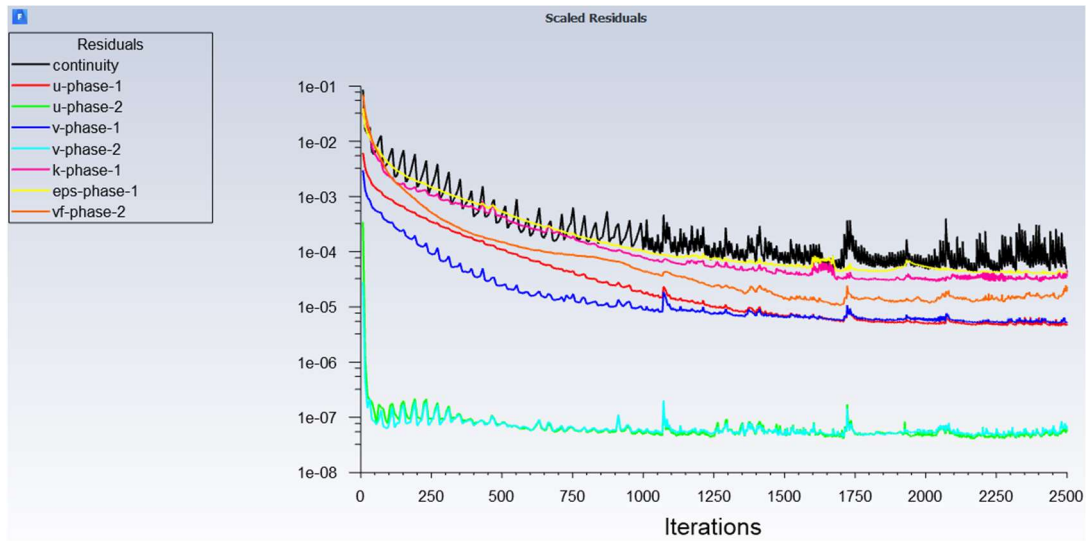


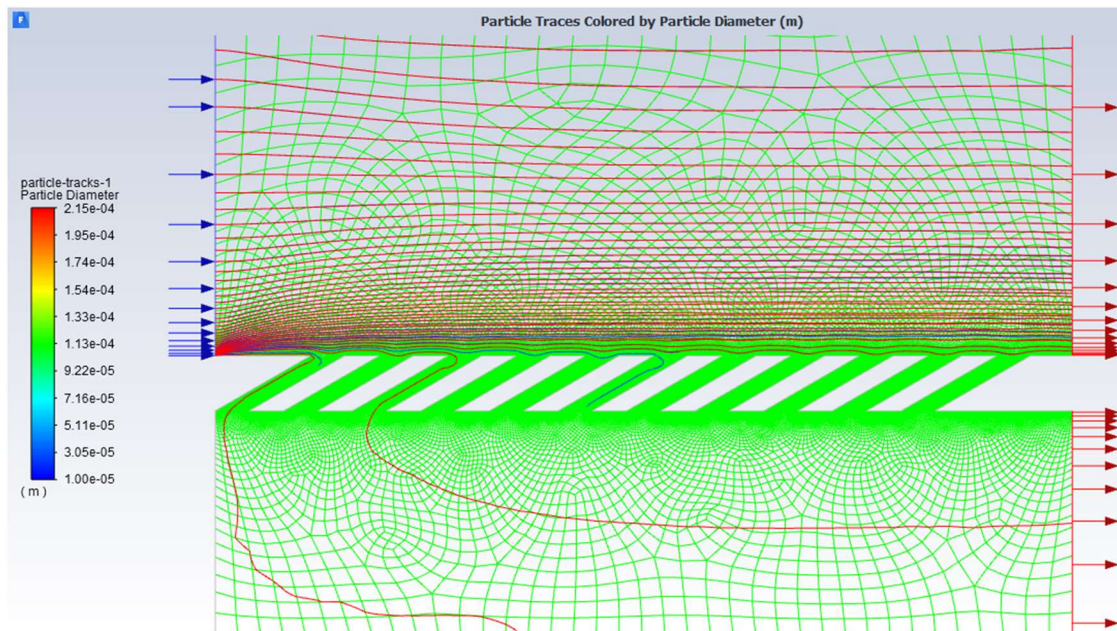
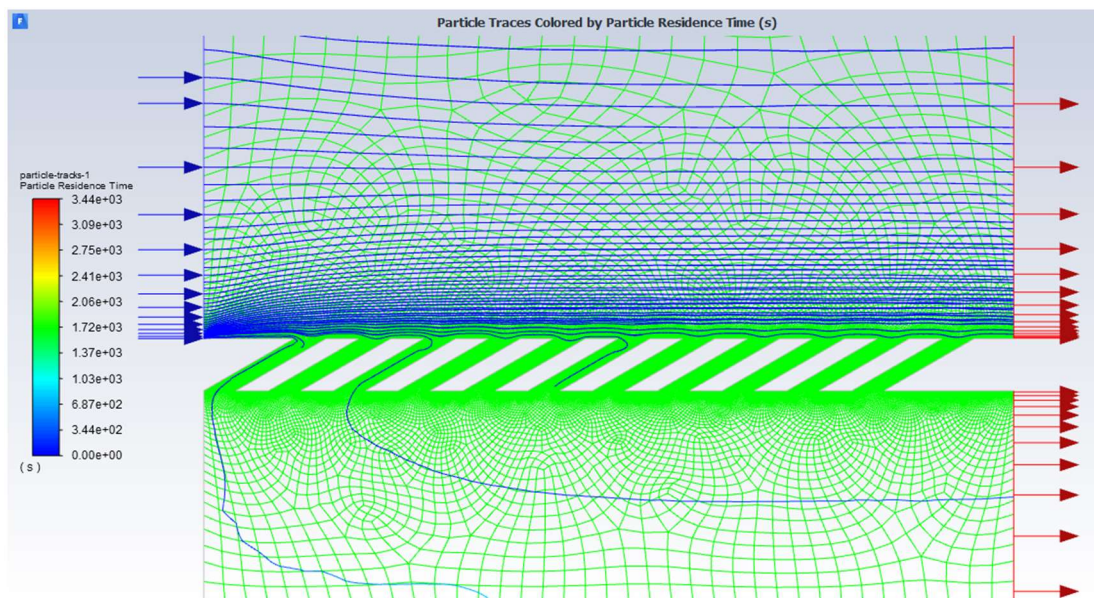
A.7. Left-Oriented 45° Angle with O₂ Phase Particle Tracks by DiameterA.8. Left-Oriented 45° Angle with O₂ Phase Particle Tracks by Residence Time

A.9 Left-Oriented 45° Angle with O₂ Phase Turbulent Kinetic Energy (Phase 1)A.10. Left-Oriented 45° Angle with O₂ Phase Volume Fraction (Phase 2)

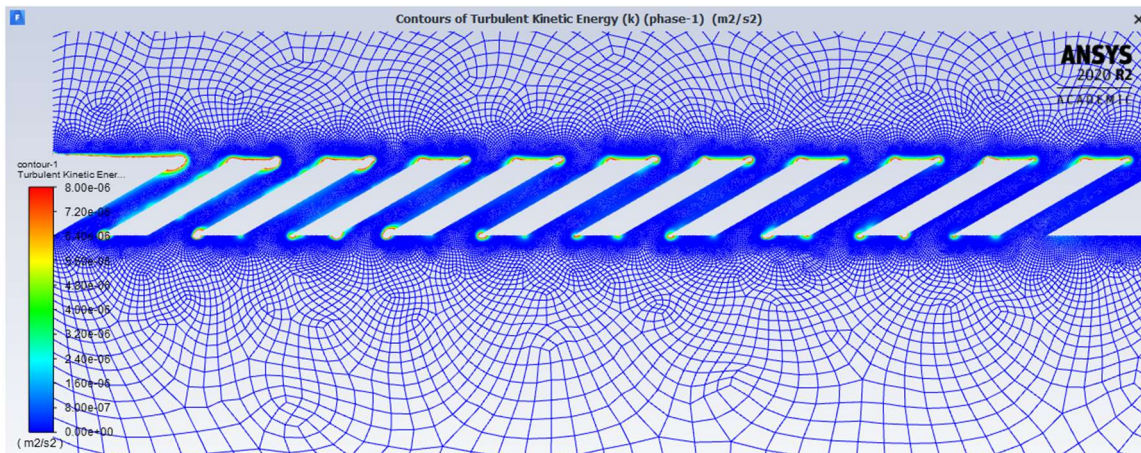
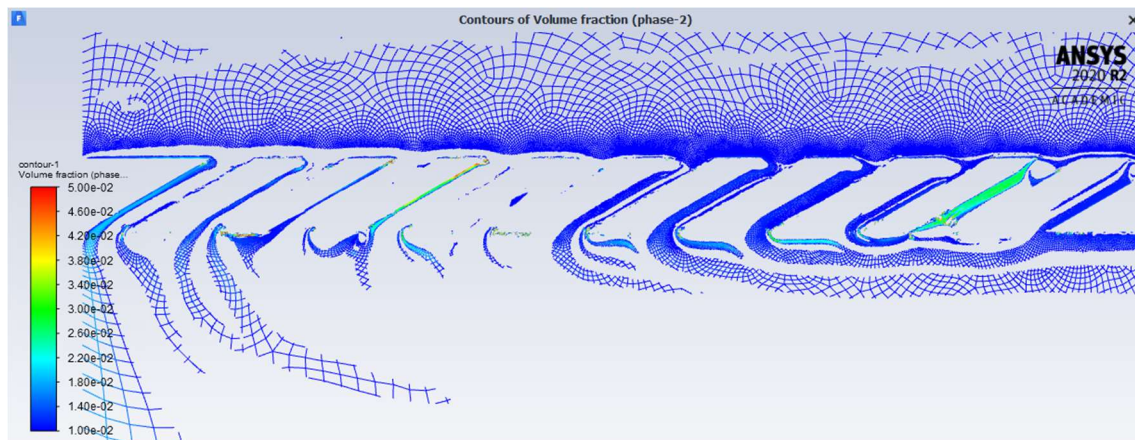
A.11. Left-Oriented 60° Angle with O_2 Phase ResidualsA.12. Left-Oriented 60° Angle with O_2 Phase Particle Tracks by Diameter

A.13. Left-Oriented 60° Angle with O₂ Phase Particle Tracks by Residence TimeA.14. Left-Oriented 60° Angle with O₂ Phase Turbulent Kinetic Energy (Phase 1)

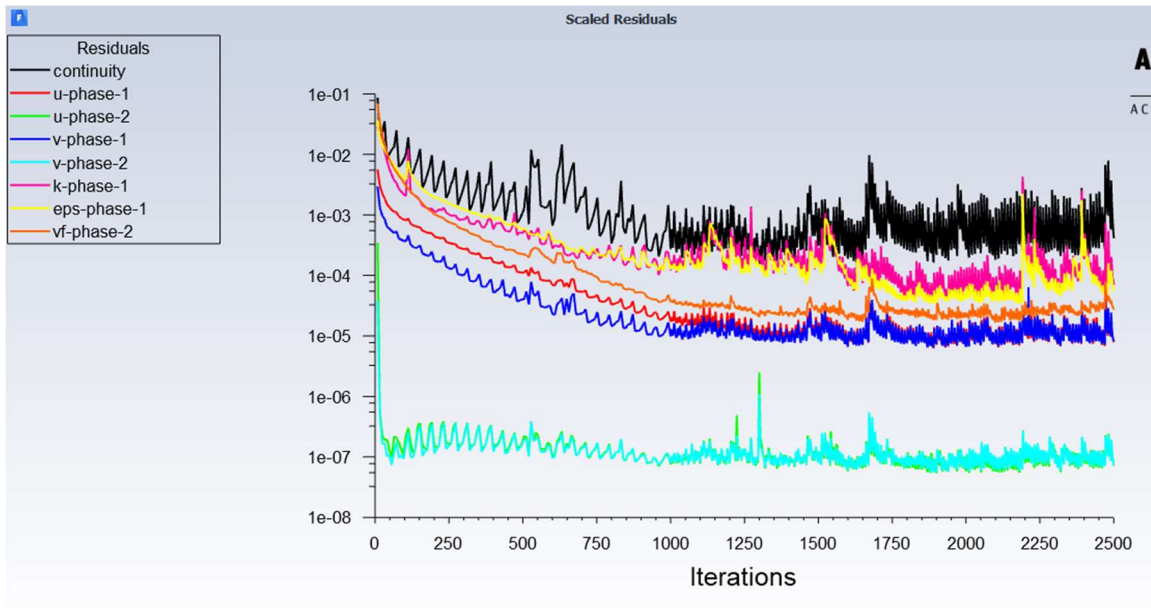
A.15. Left-Oriented 60° Angle with O_2 Phase Volume Fraction (Phase 2)A.16. Right-Oriented 30° Angle with O_2 Phase Residuals

A.17. Right-Oriented 30° Angle with O₂ Phase Particle Tracks by DiameterA.18. Right-Oriented 30° Angle with O₂ Phase Particle Tracks by Residence Time

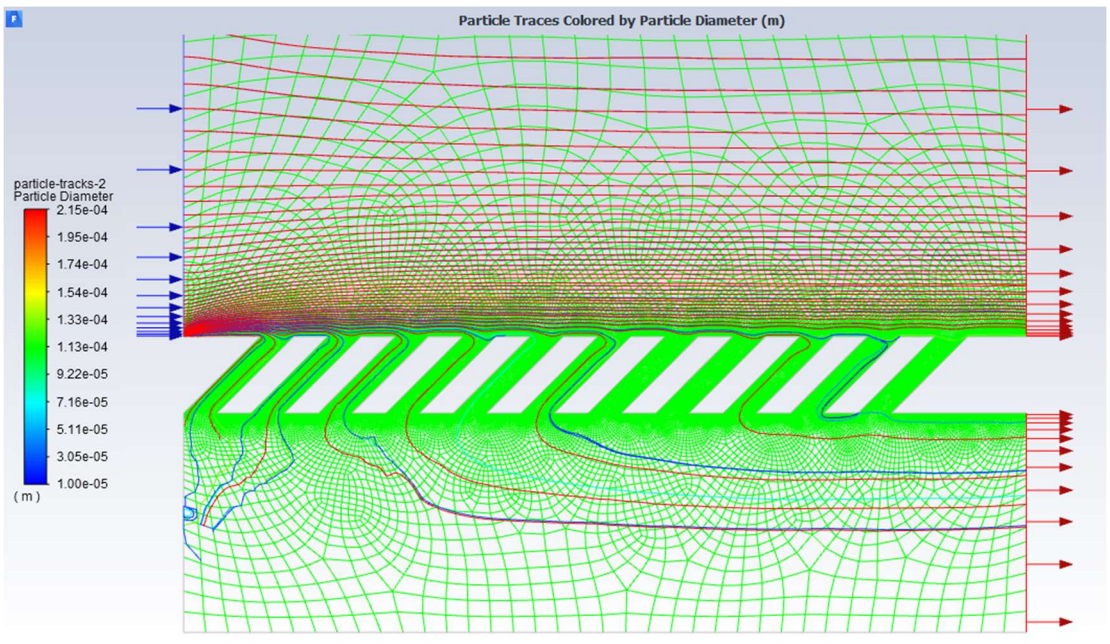
A.19. Right-Oriented 30° Angle Turbulent Kinetic Energy (Phase 1)

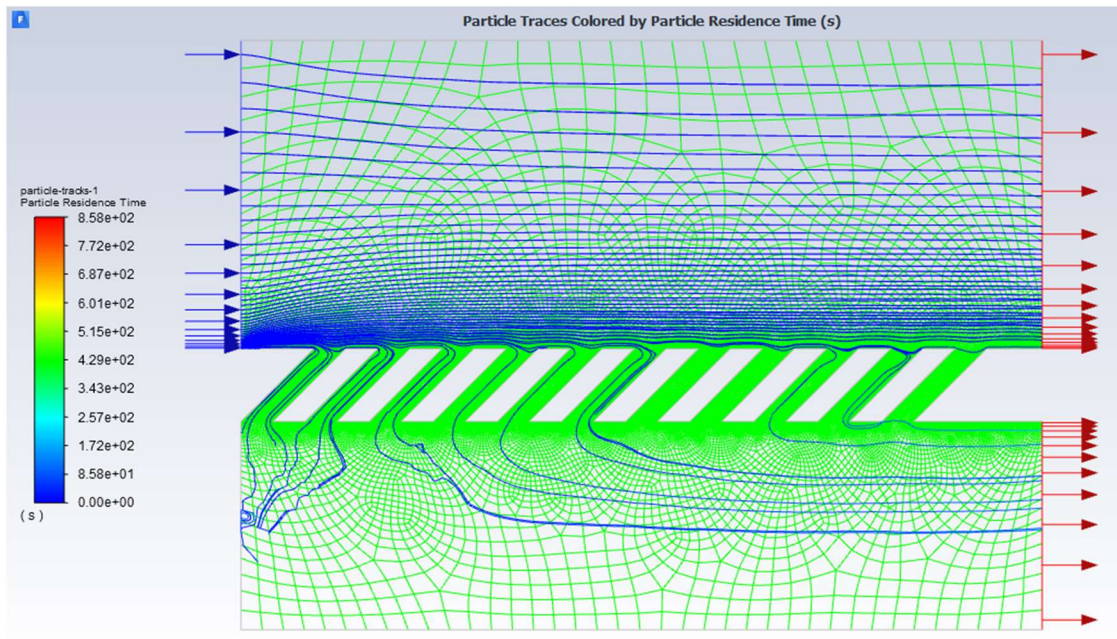
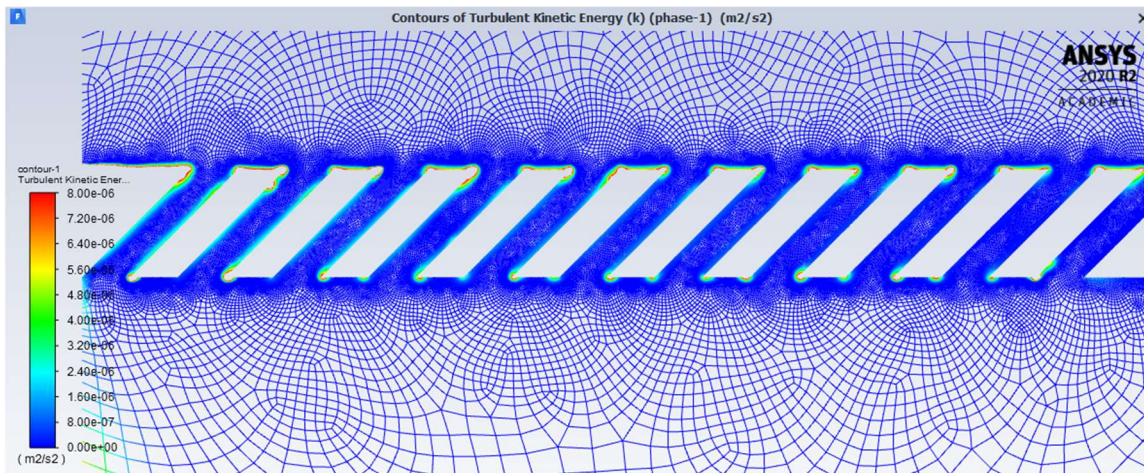
A.20. Right-Oriented 30° Angle with O₂ Phase Volume Fraction (Phase 2)

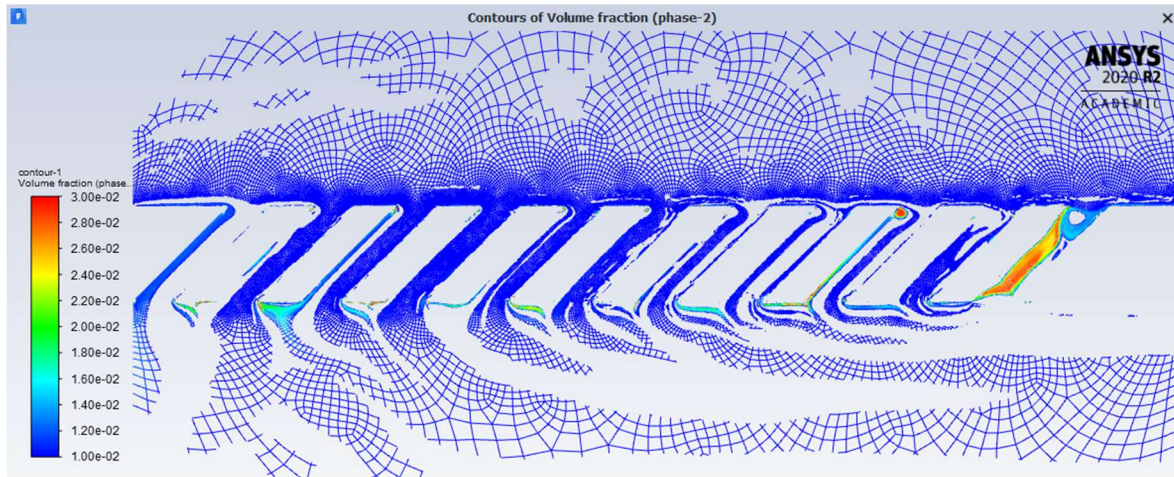
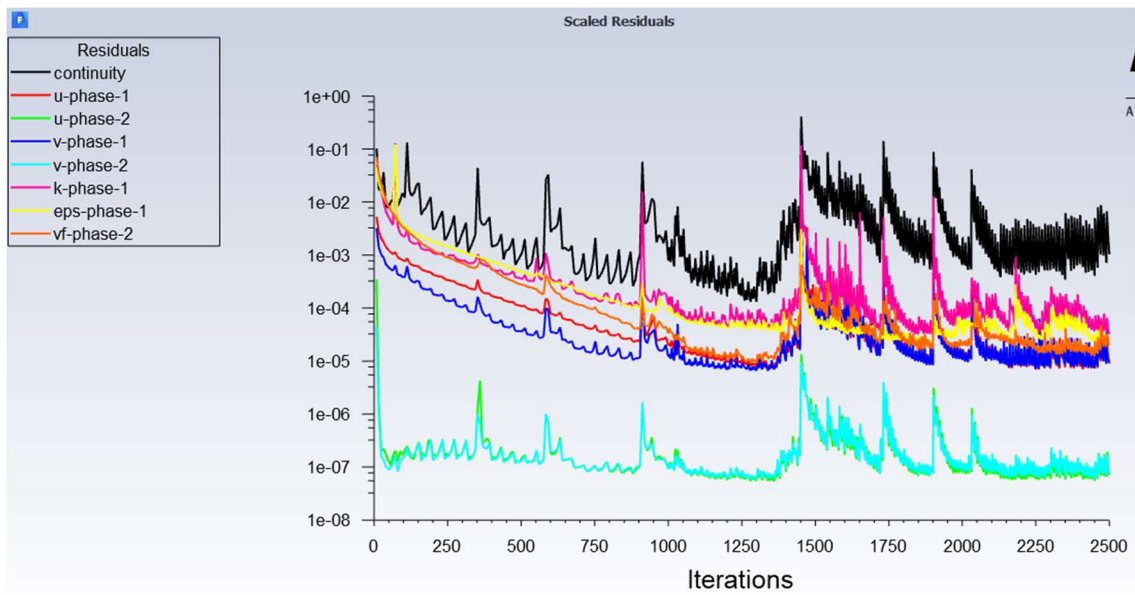
A.21. Right-Oriented 45° Angle with O₂ Phase Residuals

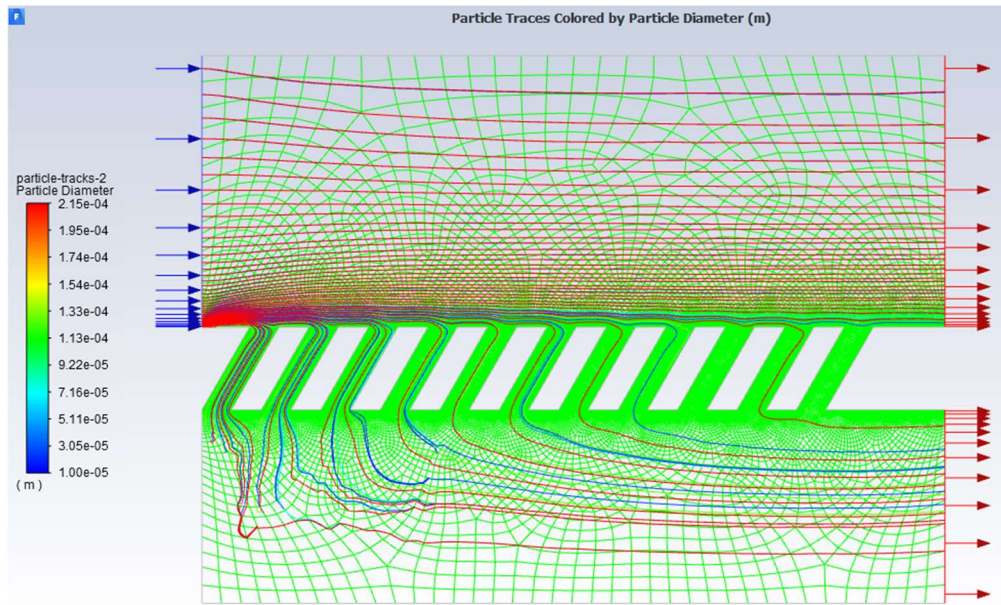
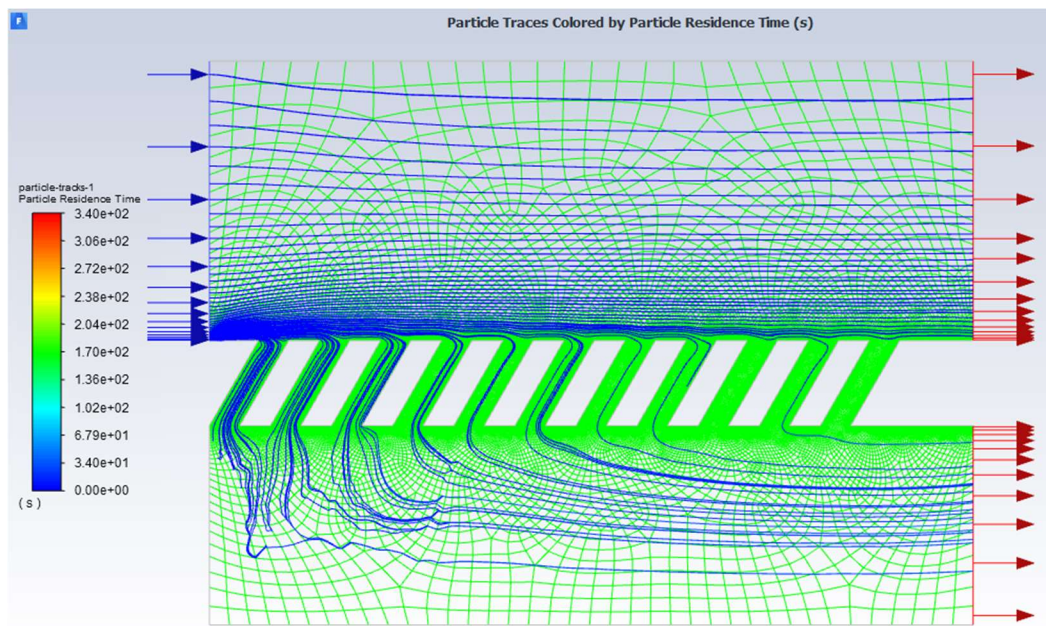


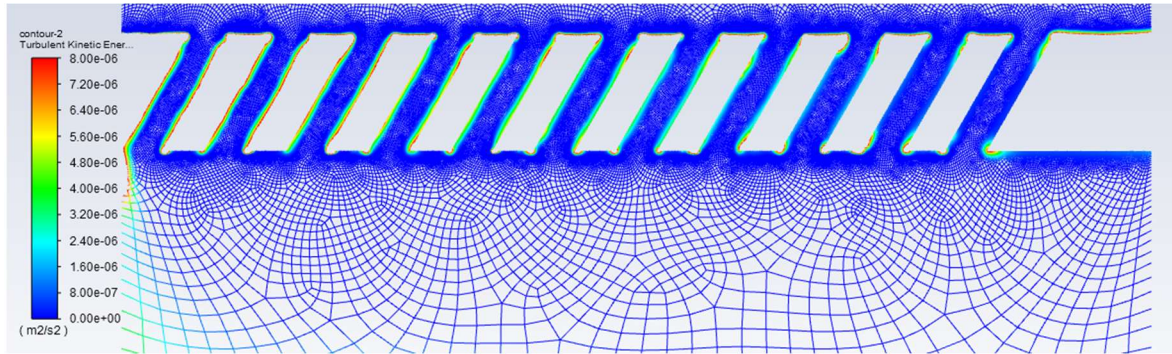
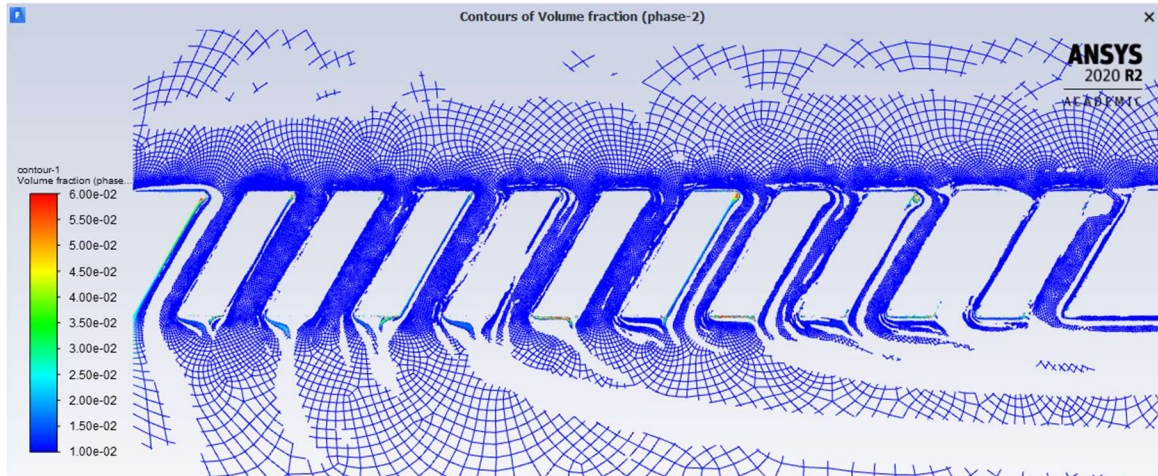
A.22. Right-Oriented 45° Angle with O₂ Phase Particle Tracks by Diameter

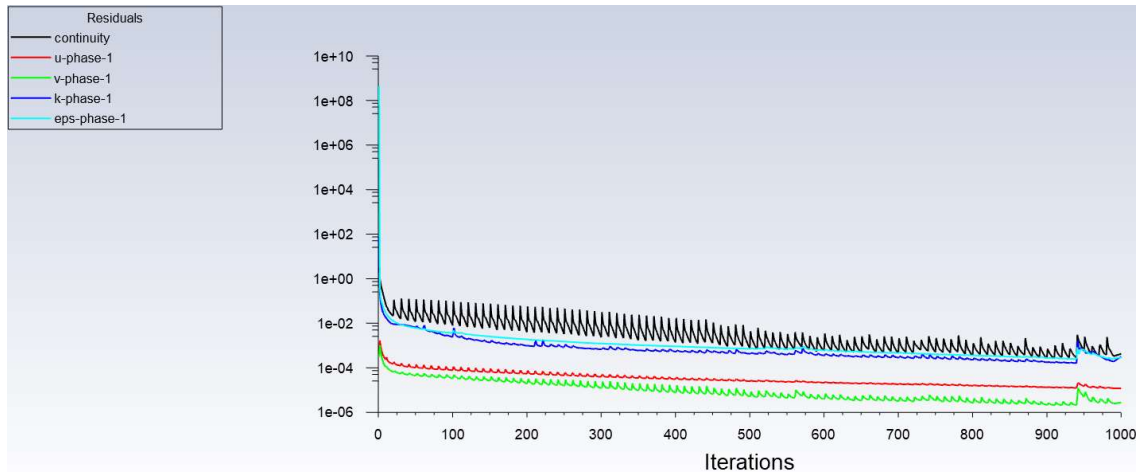
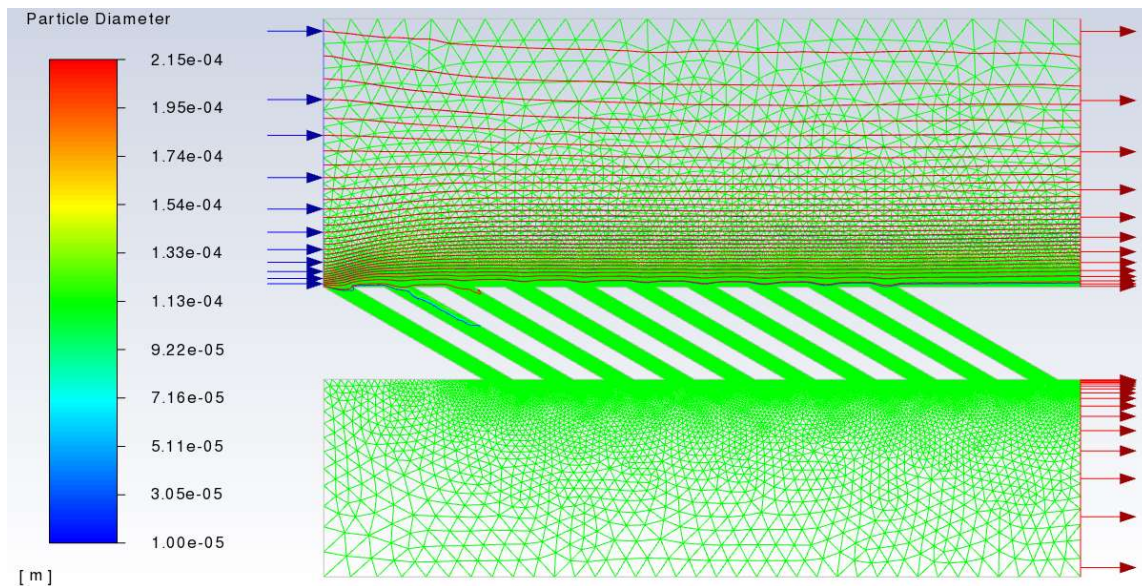


A.23. Right-Oriented 45° Angle with O₂ Phase Particle Tracks by Residence TimeA.24. Right-Oriented 45° Angle with O₂ Phase Turbulent Kinetic Energy (Phase 1)

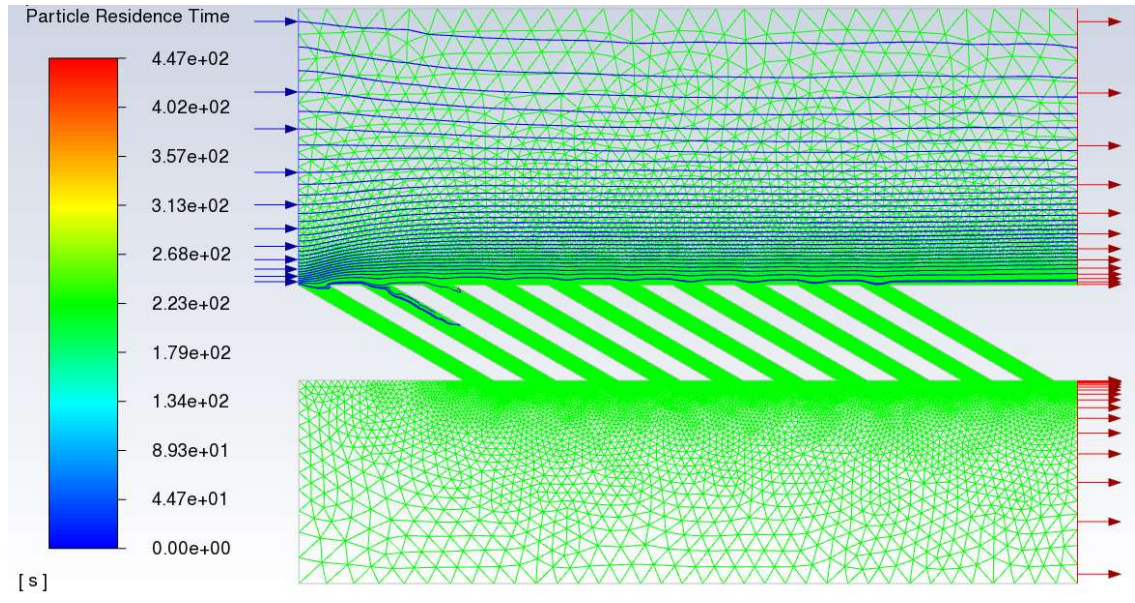
A.25. Right-Oriented 45° Angle with O₂ Phase Volume Fraction (Phase 2)A.26. Right-Oriented 60° Angle with O₂ Phase Residuals

A.27. Right-Oriented 60° Angle with O_2 Phase Particle Tracks by DiameterA.28. Right-Oriented 60° Angle with O_2 Phase Particle Tracks by Residence Time

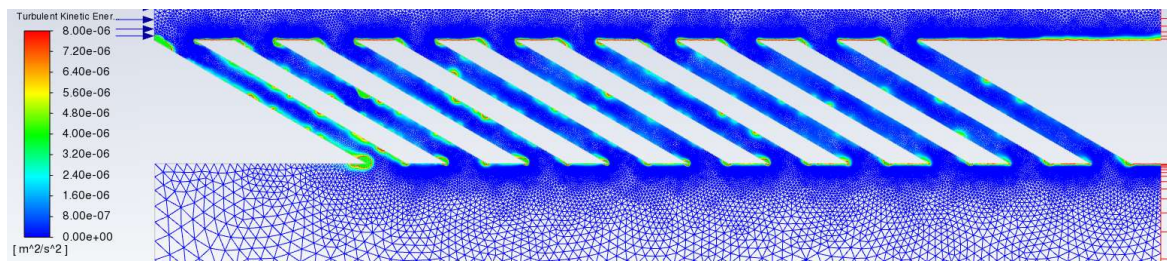
A.29. Right-Oriented 60° Angle with O₂ Phase Turbulent Kinetic Energy (Phase 1)A.30. Right-Oriented 60° Angle with O₂ Phase Volume Fraction (Phase 2)

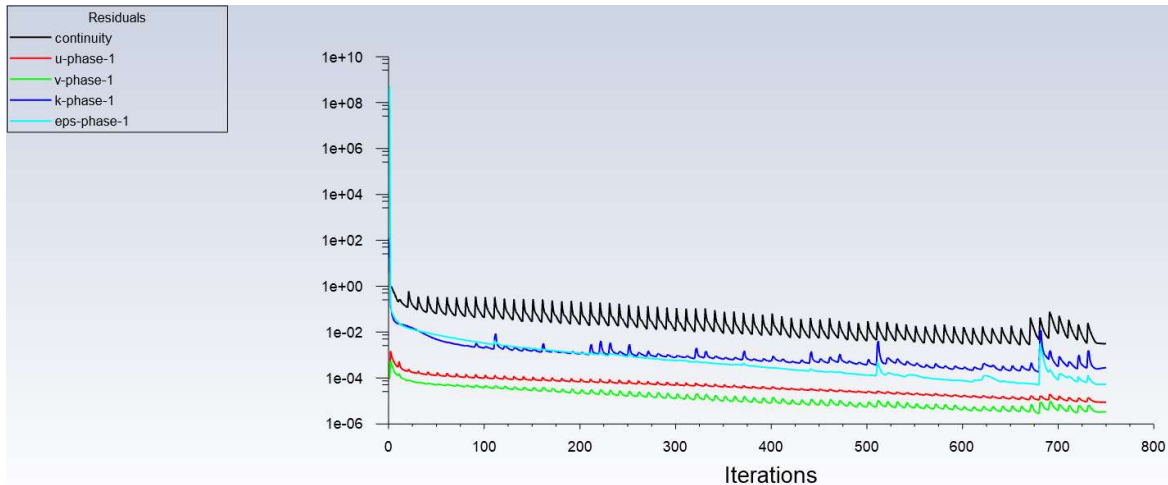
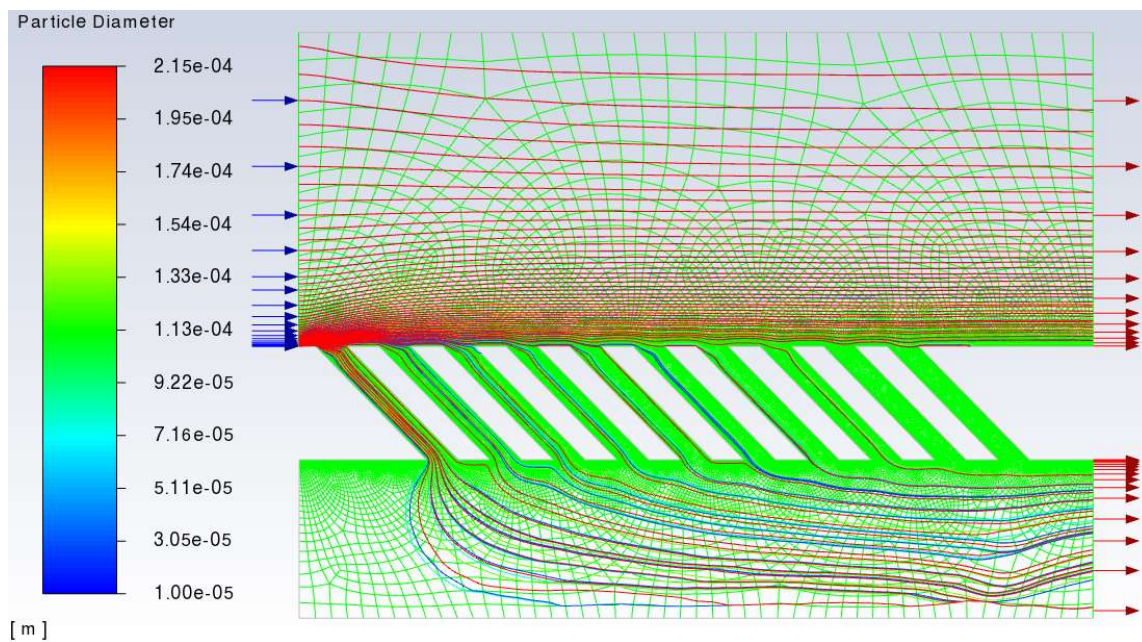
A.31. Left-Oriented 30° Angle without O₂ Phase ResidualsA.32. Left-Oriented 30° Angle without O₂ Phase Particle Tracks by Diameter

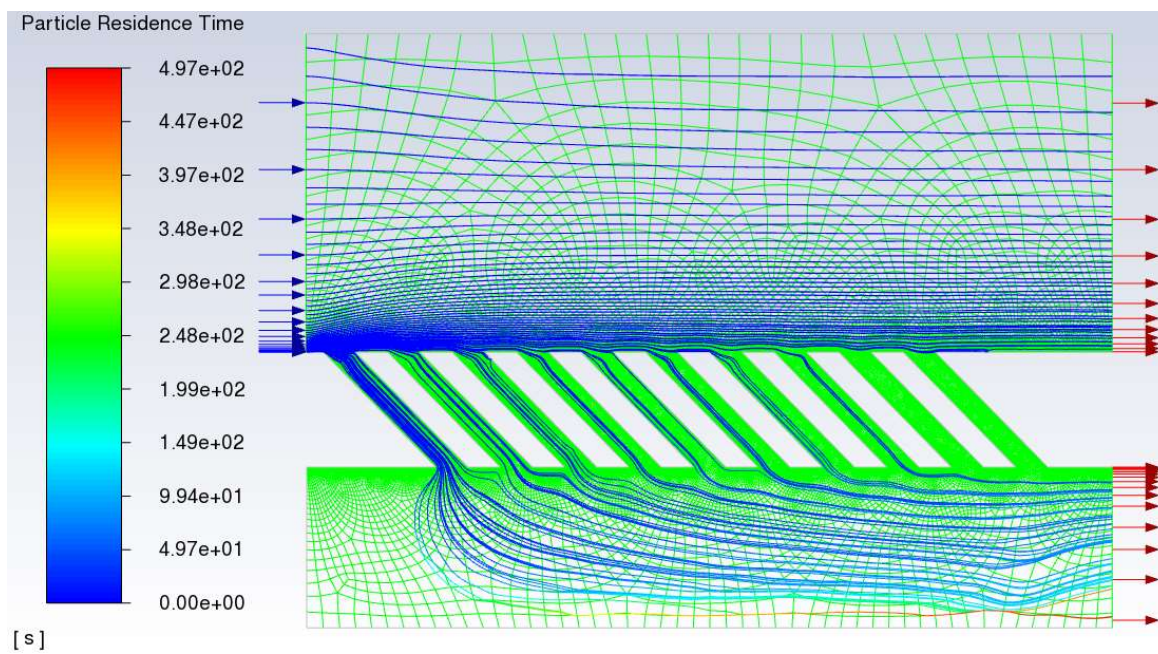
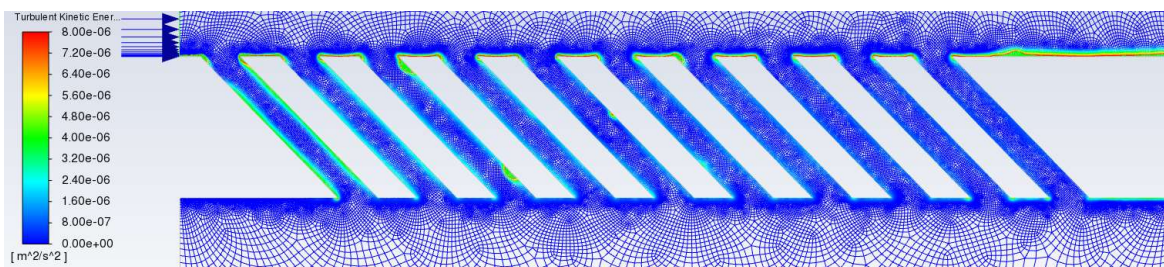
A.33. Left-Oriented 30° Angle without O₂ Phase Particle Tracks by Residence Time



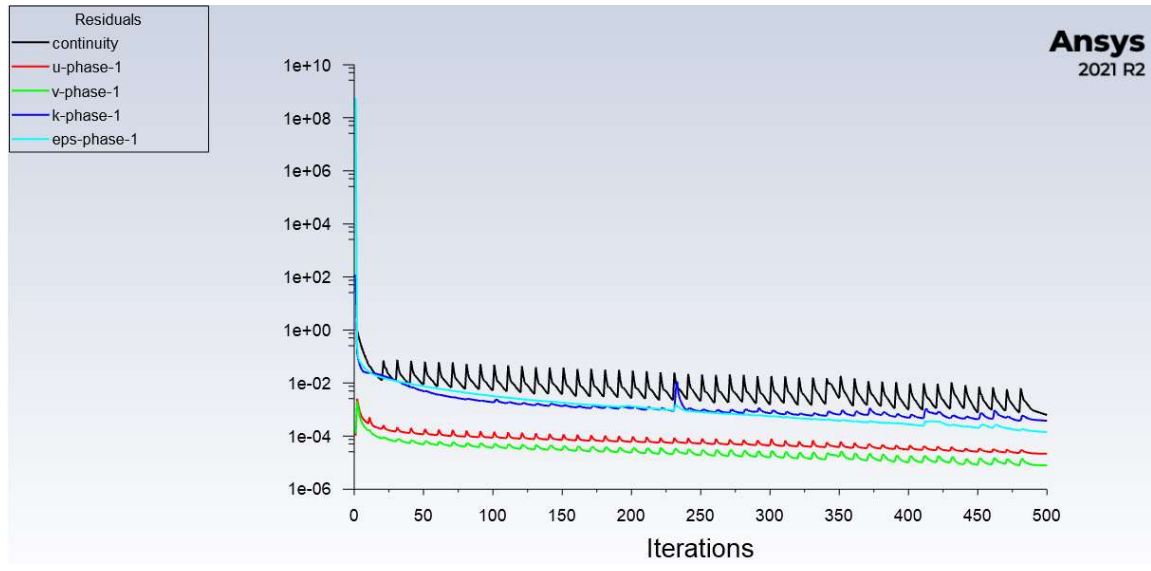
A.34. Left-Oriented 30° Angle without O₂ Phase Turbulent Kinetic Energy (Phase 1)



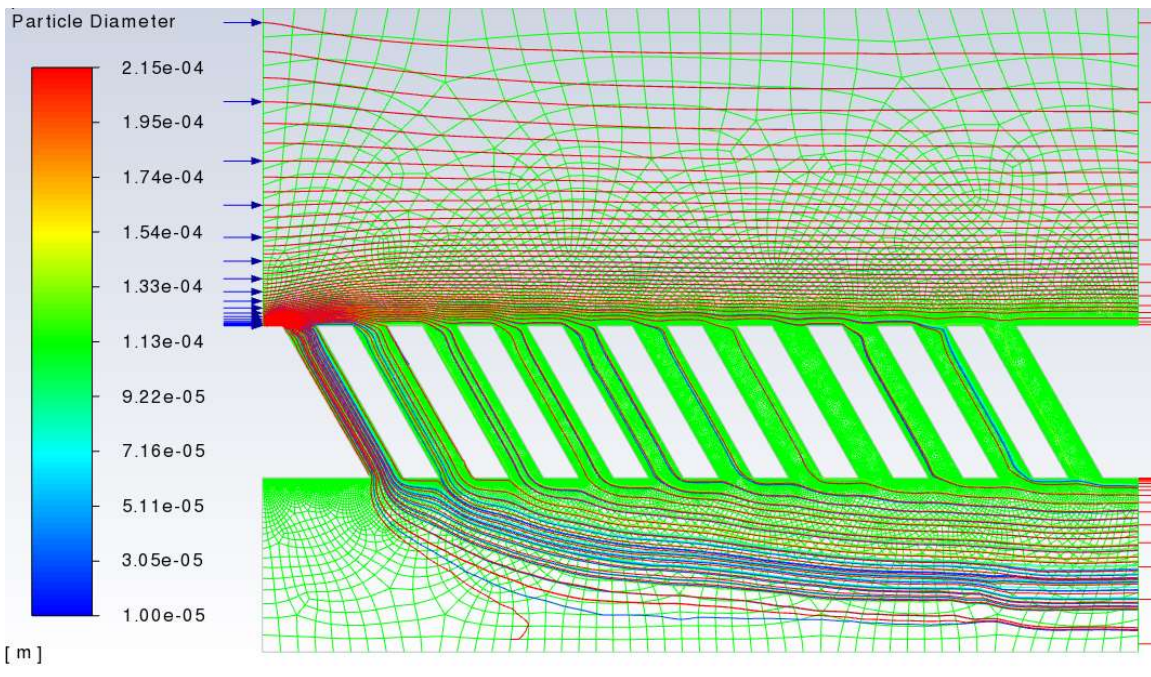
A.35. Left-Oriented 45° Angle without O₂ Phase ResidualsA.36. Left-Oriented 45° Angle without O₂ Phase Particle Tracks by Diameter

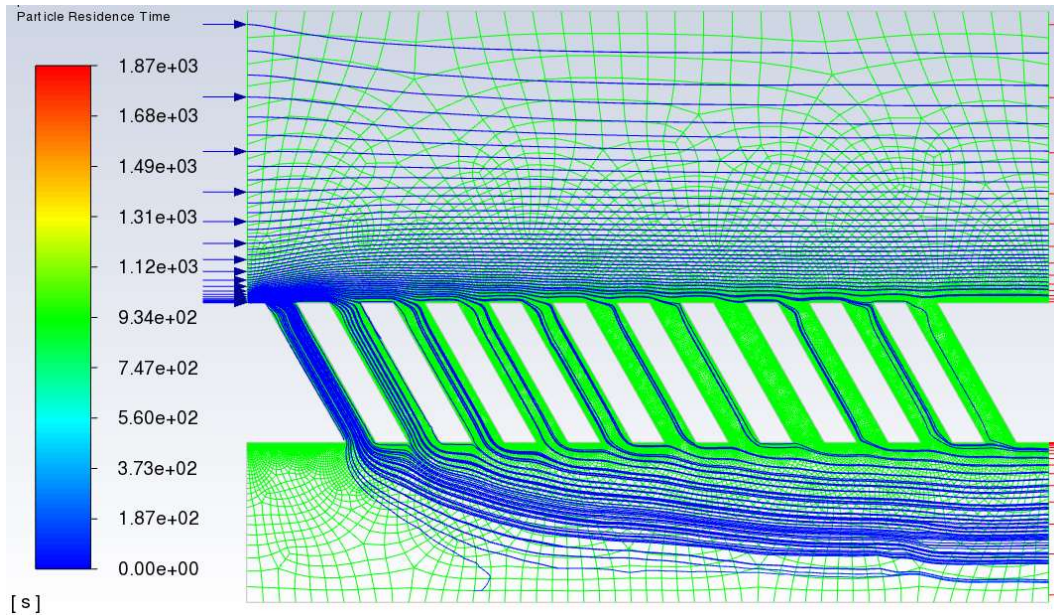
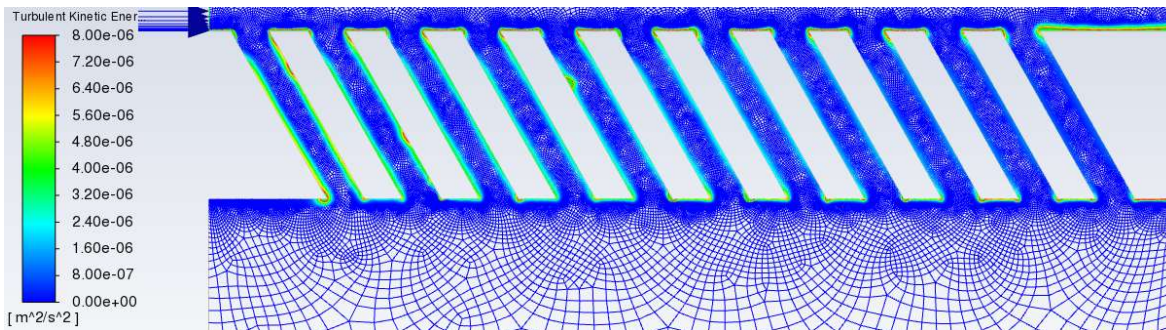
A.37. Left-Oriented 45° Angle without O₂ Phase Particle Tracks by Residence TimeA.38. Left-Oriented 45° Angle without O₂ Phase Turbulent Kinetic Energy (Phase 1)

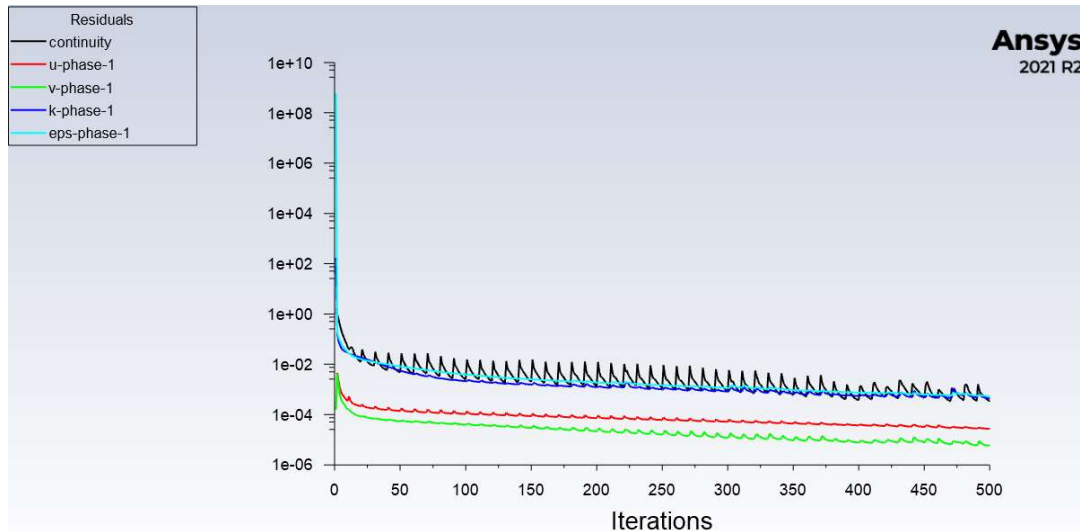
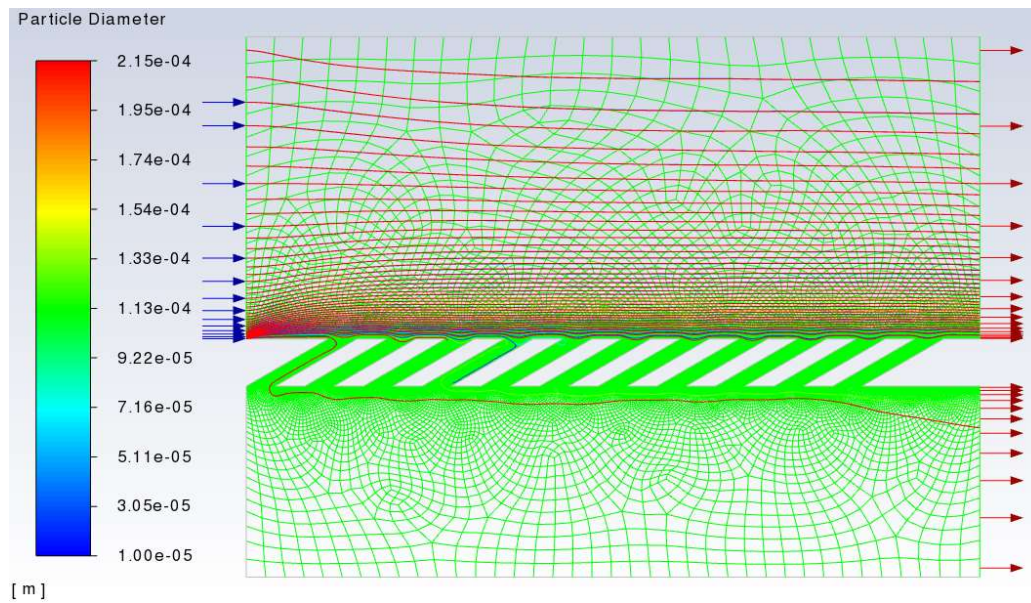
A.39. Left-Oriented 60° Angle without O₂ Phase Residuals

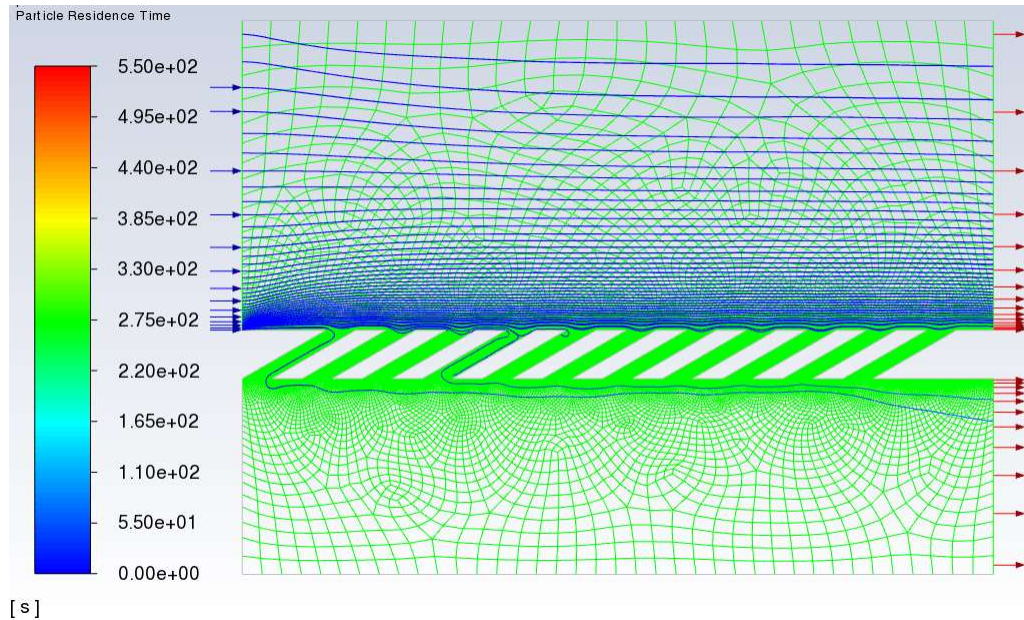
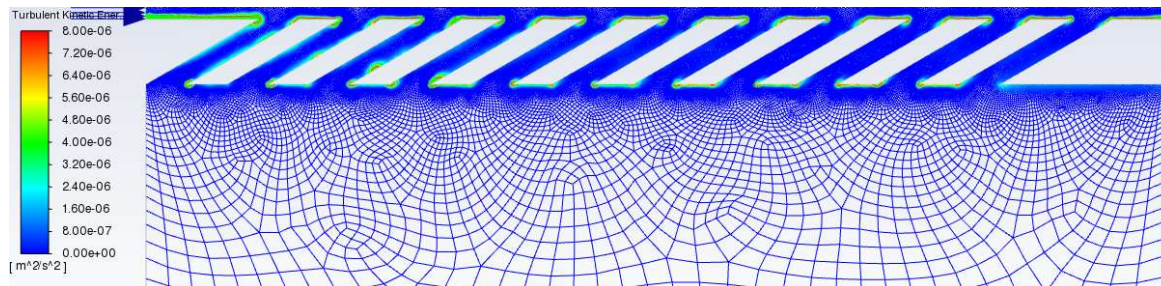


A.40. Left-Oriented 60° Angle without O₂ Phase Particle Tracks by Diameter

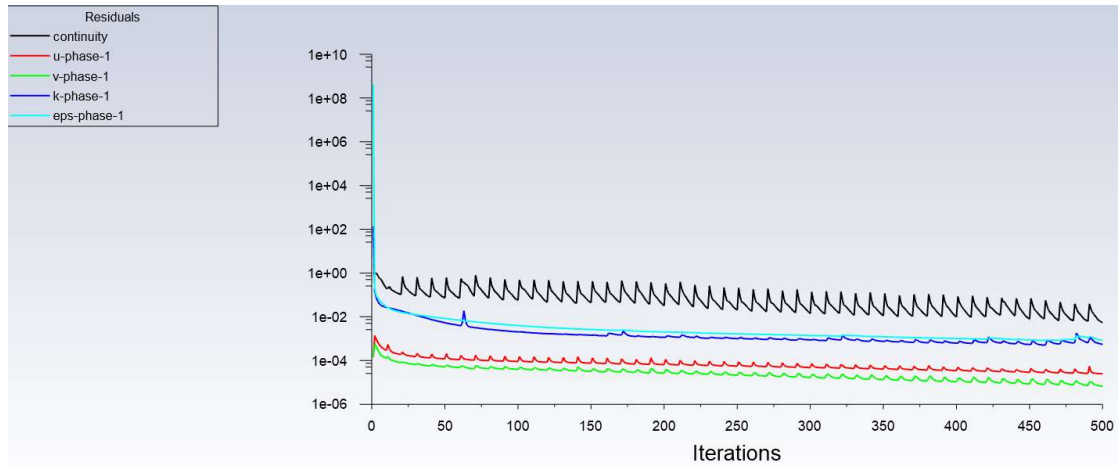


A.41. Left-Oriented 60° Angle without O₂ Phase Particle Tracks by Residence TimeA.42. Left-Oriented 60° Angle without O₂ Phase Turbulent Kinetic Energy (Phase 1)

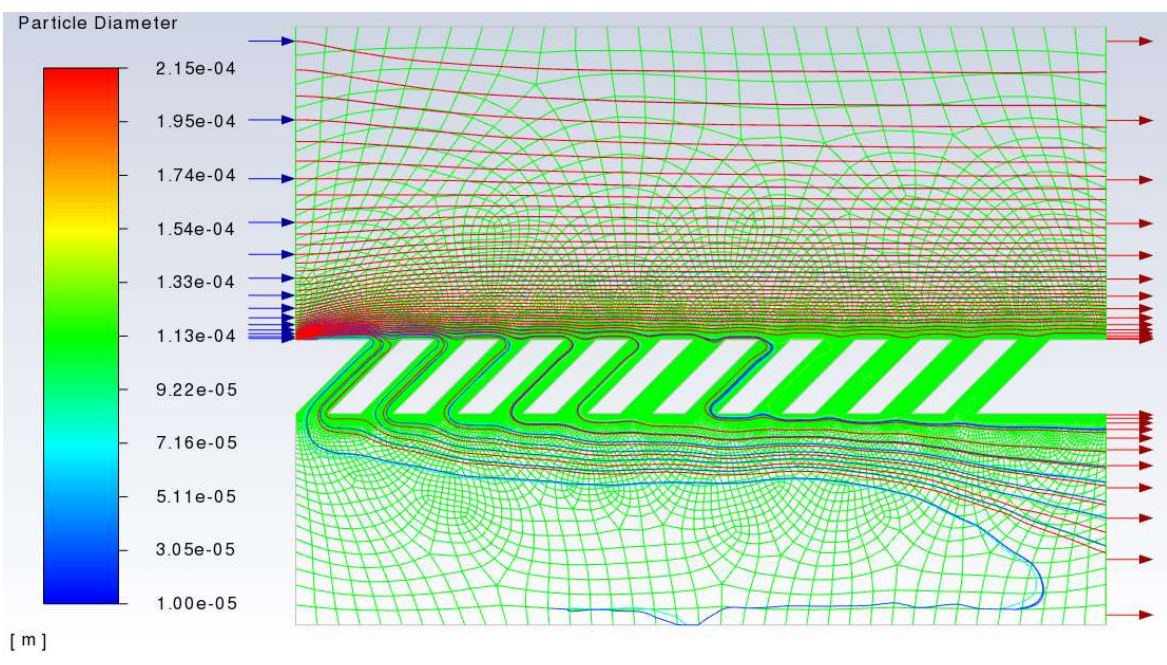
A.43. Right-Oriented 30° Angle without O₂ Phase ResidualsA.44. Right-Oriented 30° Angle without O₂ Phase Particle Tracks by Diameter

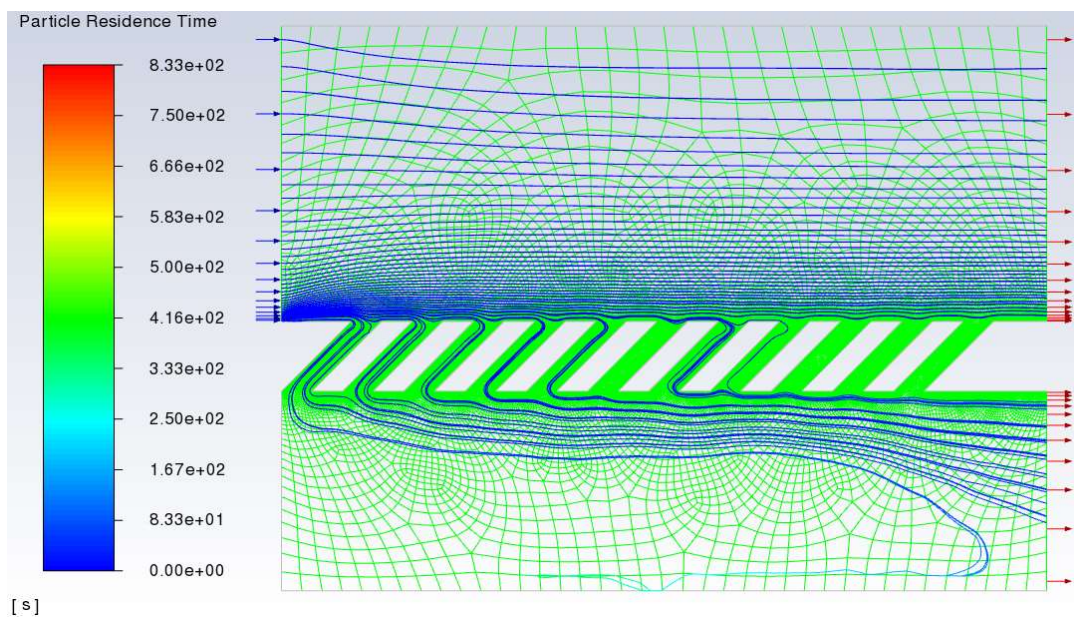
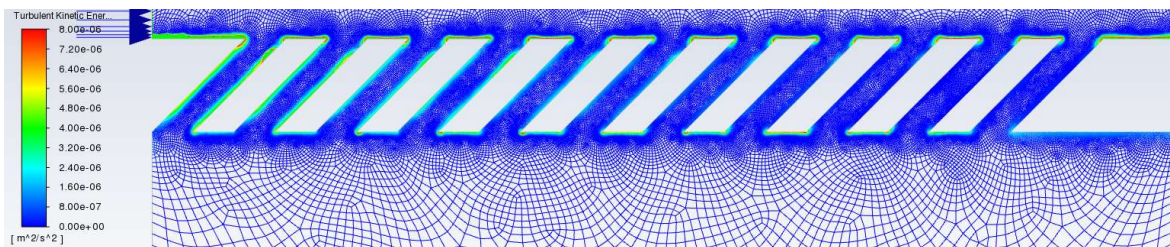
A.45. Right-Oriented 30° Angle without O₂ Phase Particle Tracks by Residence TimeA.46. Right-Oriented 30° Angle without O₂ Phase Turbulent Kinetic Energy (Phase 1)

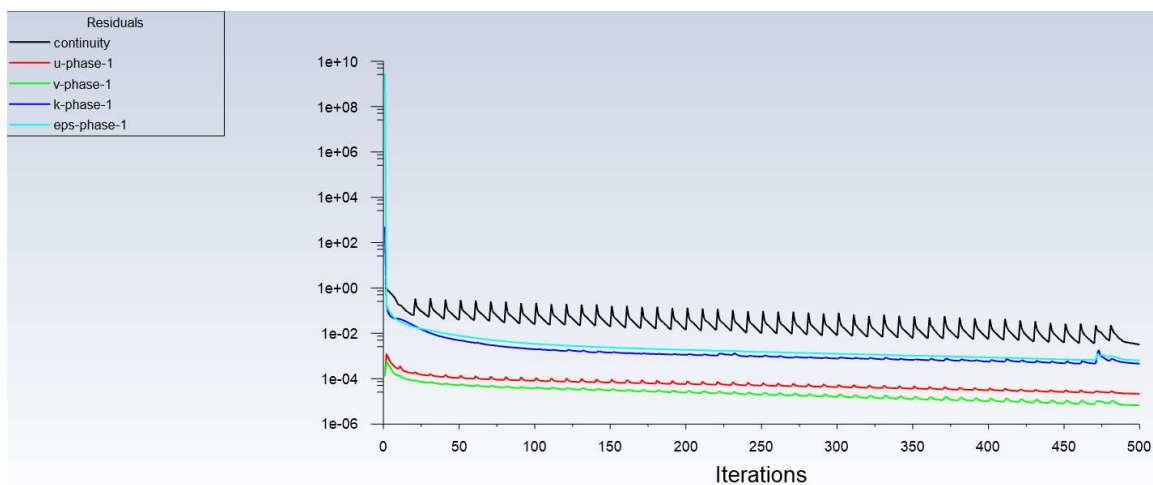
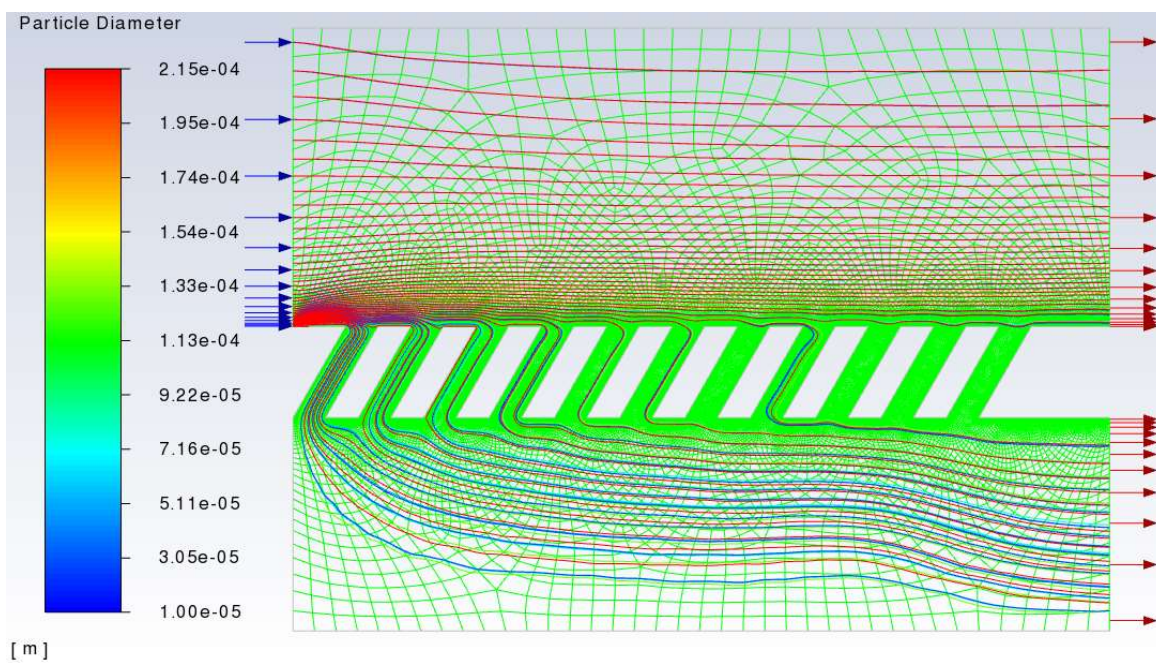
A.47. Right-Oriented 45° Angle without O₂ Phase Residuals

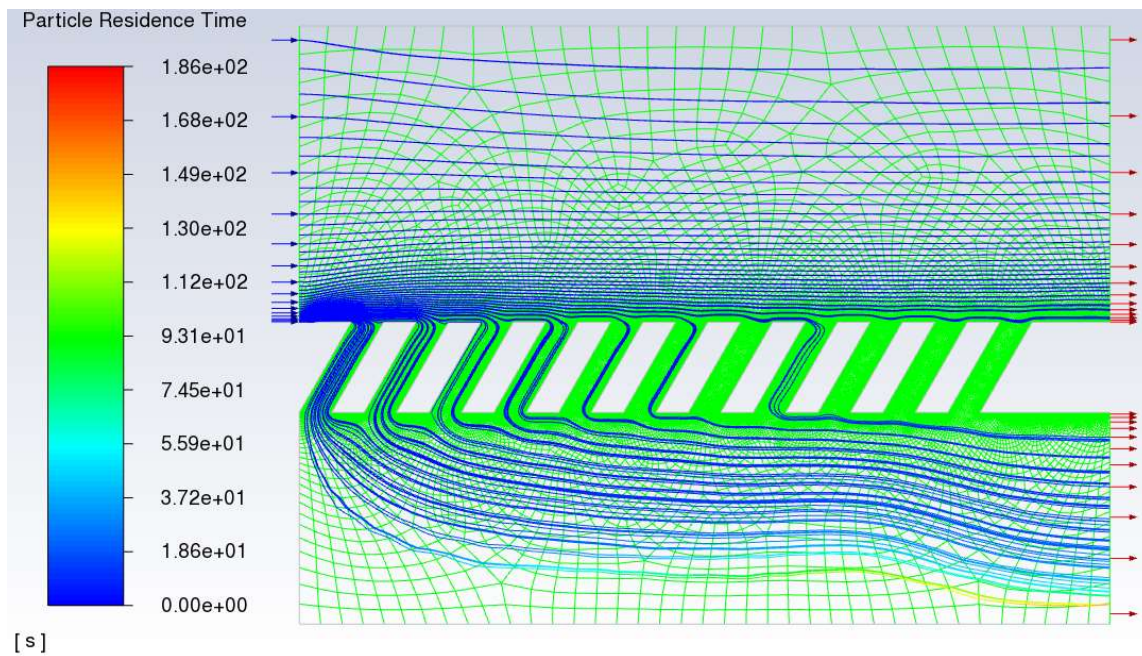
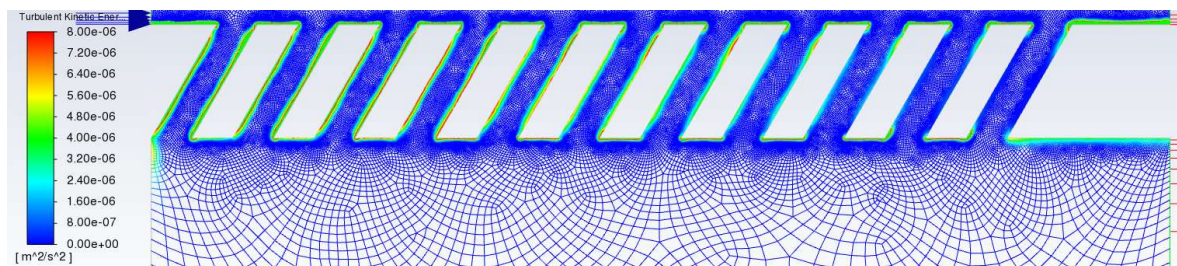


A.48. Right-Oriented 45° Angle without O₂ Phase Particle Tracks by Diameter

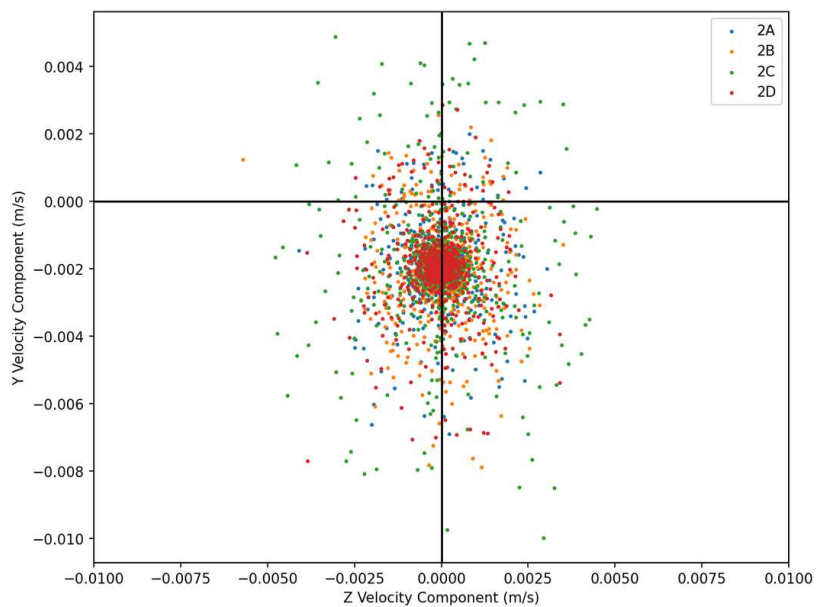


A.49. Right-Oriented 45° Angle without O₂ Phase Particle Tracks by Residence TimeA.50. Right-Oriented 45° Angle without O₂ Phase Turbulent Kinetic Energy (Phase 1)

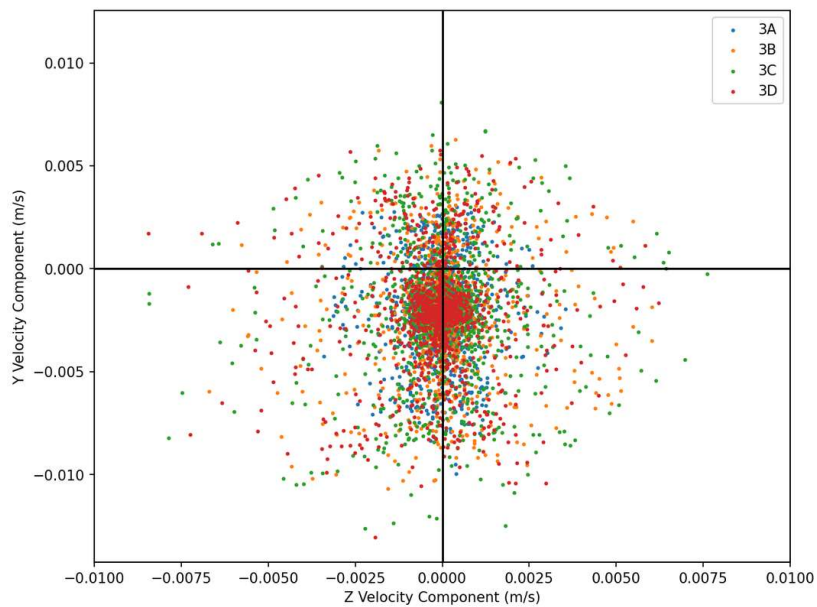
A.51. Right-Oriented 60° Angle without O_2 Phase ResidualsA.52. Right-Oriented 60° Angle without O_2 Phase Particle Tracks by Diameter

A.53. Right-Oriented 60° Angle without O₂ Phase Particle Tracks by Residence TimeA.54. Right-Oriented 60° Angle without O₂ Phase Turbulent Kinetic Energy (Phase 1)

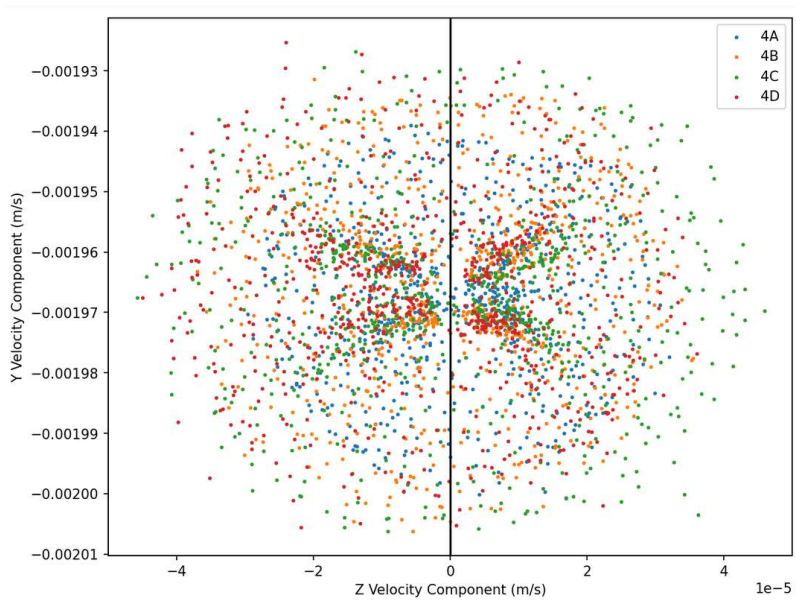
A.55. Particle YZ-Velocity Plot for Distribution 2



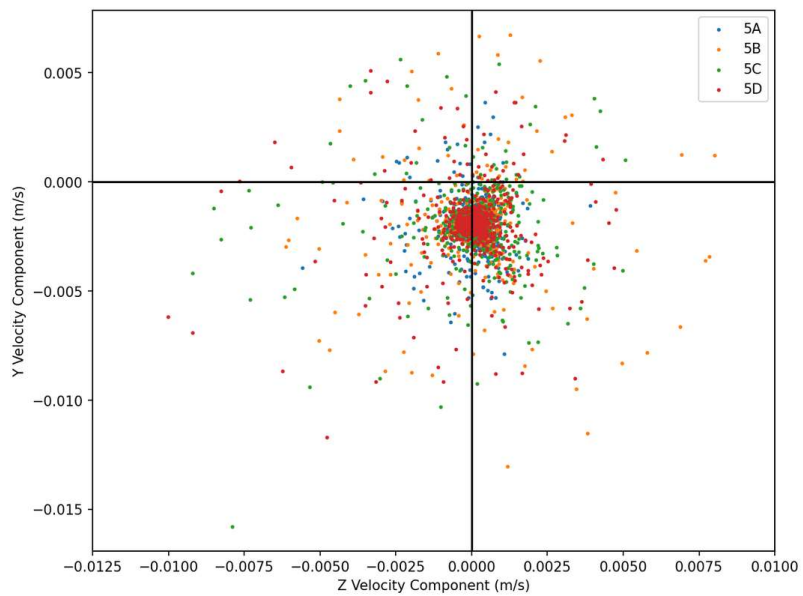
A.56. Particle YZ-Velocity Plot for Distribution 3



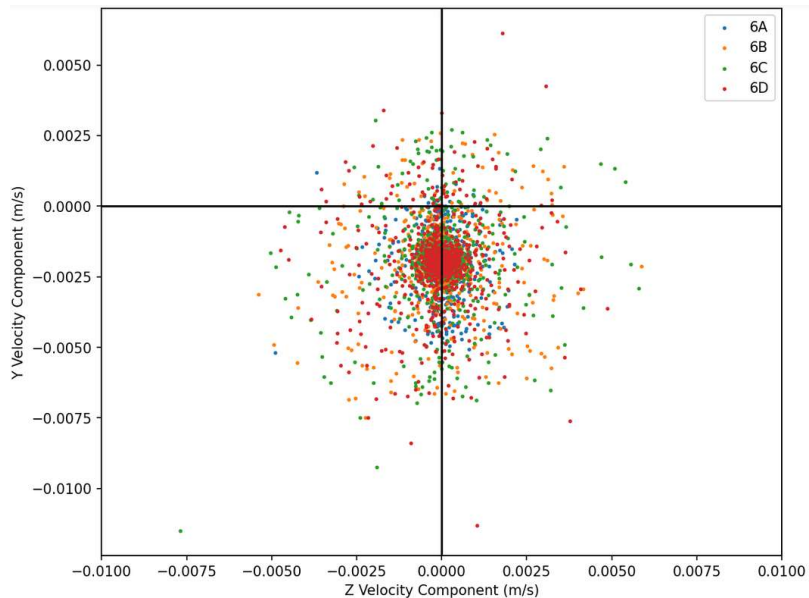
A.57. Particle YZ-Velocity Plot for Distribution 4



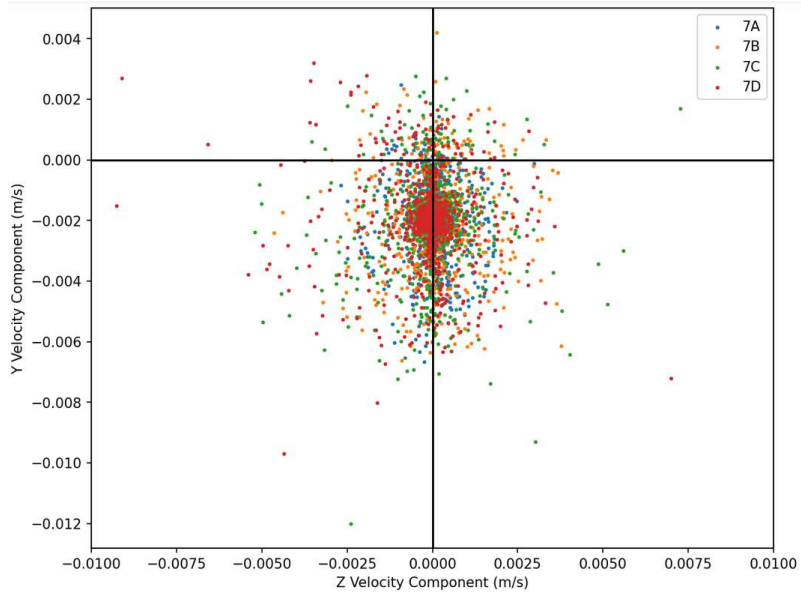
A.58. Particle YZ-Velocity Plot for Distribution 5



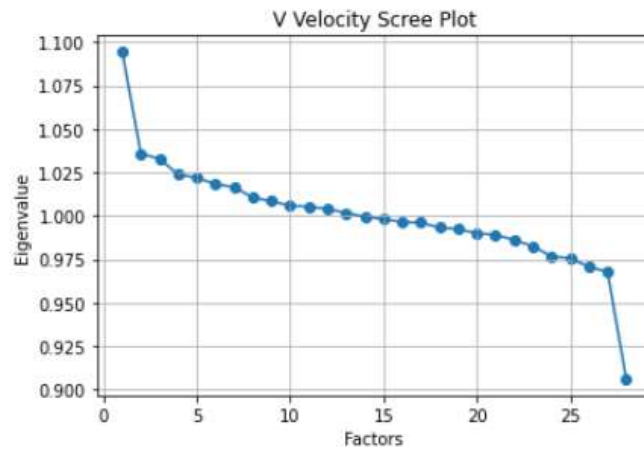
A.59. Particle YZ-Velocity Plot for Distribution 6



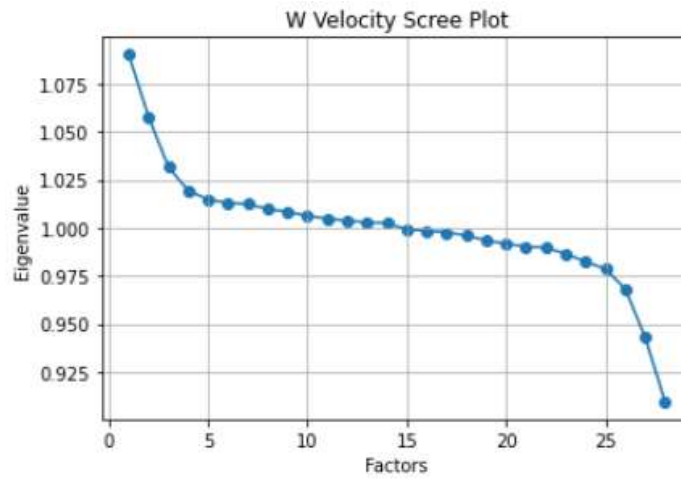
A.60. Particle YZ-Velocity Plot for Distribution 7



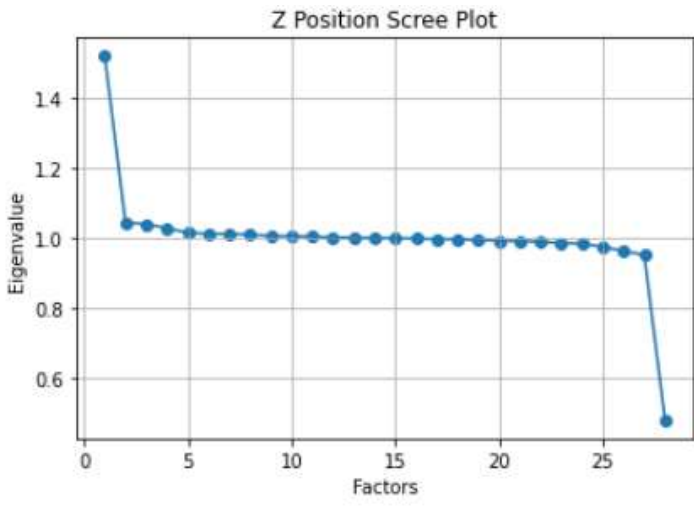
A.61. Scree Plot for V (y-axis) Velocity



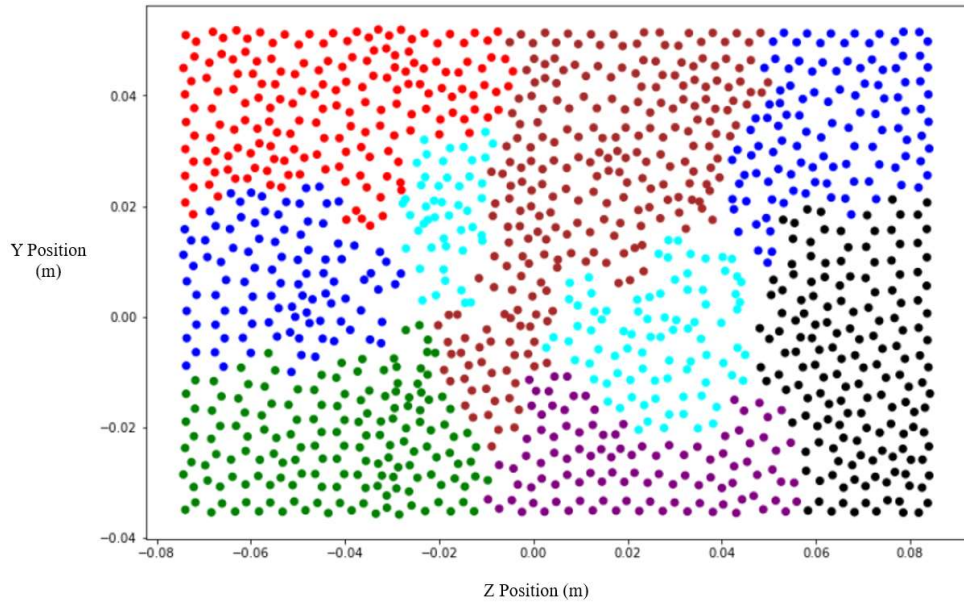
A.62. Scree Plot for W (z-axis) Velocity



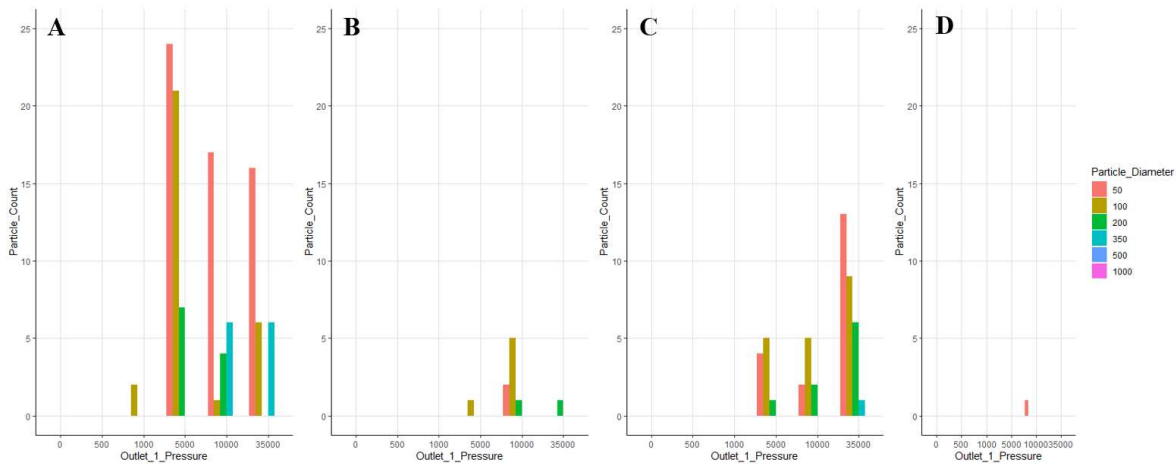
A.63. Scree Plot for z-axis Position



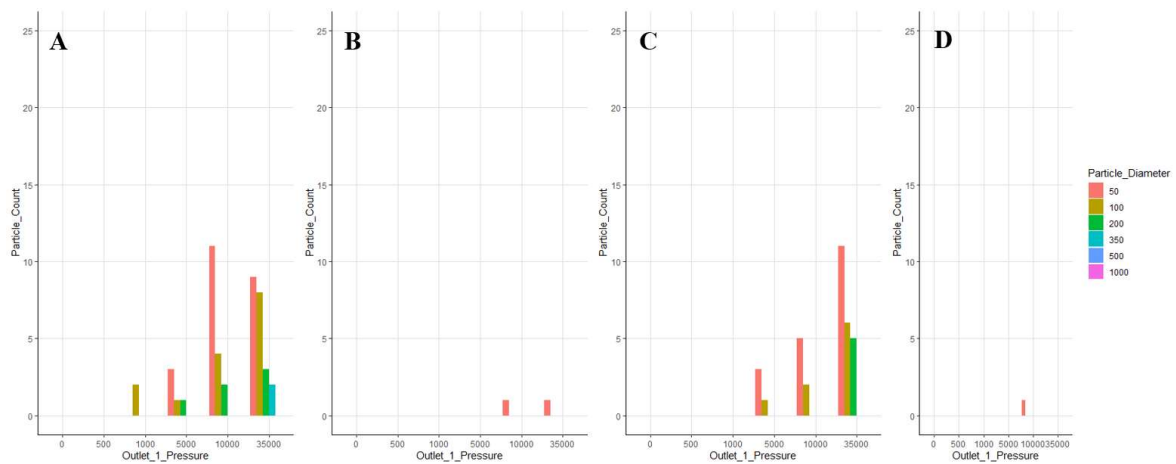
A.64. Hierarchical agglomerative clustering of particle position for 7 clusters.



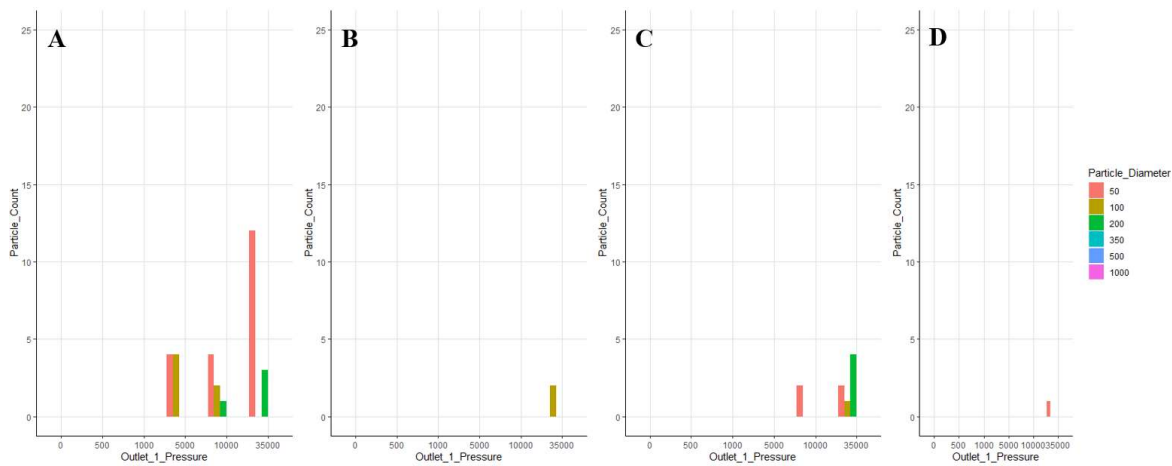
A.65. Particle Counts vs Outlet Pressure with inlet velocity of 0.2 m/s for (A) Conv_1_90, (B) Conv_0.5_90, (C) Flat_1_90, and (D) Conv_1_40.



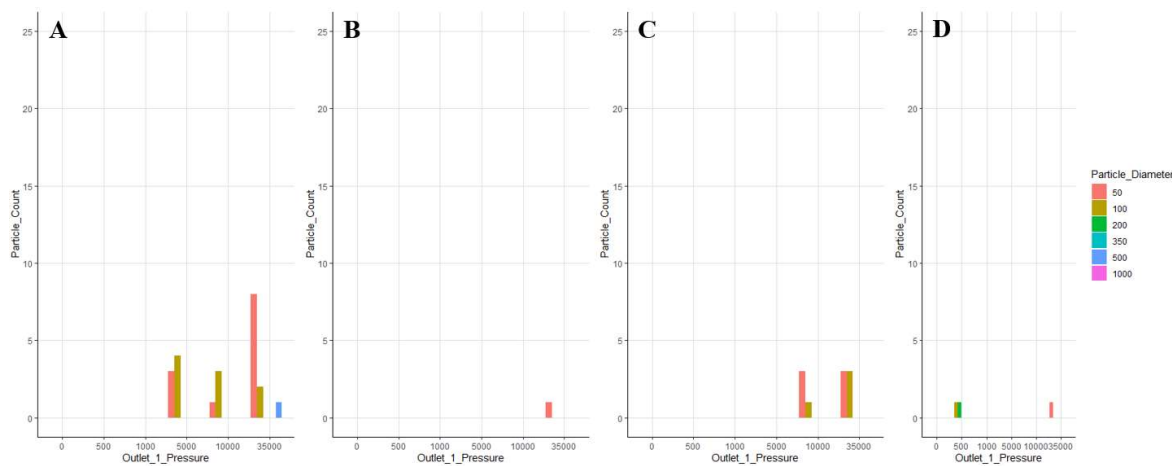
A.66. Particle Counts vs Outlet Pressure with inlet velocity of 0.24 m/s for (A) Conv_1_90, (B) Conv_0.5_90, (C) Flat_1_90, and (D) Conv_1_40.



A.67. Particle Counts vs Outlet Pressure with inlet velocity of 0.32 m/s for (A) Conv_1_90, (B) Conv_0.5_90, (C) Flat_1_90, and (D) Conv_1_40.



A.68. Particle Counts vs Outlet Pressure with inlet velocity of 0.36 m/s for (A) Conv_1_90, (B) Conv_0.5_90, (C) Flat_1_90, and (D) Conv_1_40.



A.69. Particle Counts vs Outlet Pressure with inlet velocity of 0.4 m/s for (A) Conv_1_90, (B) Conv_0.5_90, (C) Flat_1_90, and (D) Conv_1_40.

